A NOVEL APPROACH TO DIAMONDLIKE CARBON BASED MID-INFRARED ATTENUATED TOTAL REFLECTANCE SPECTROELECTROCHEMISTRY

A Thesis
Presented to
The Academic Faculty

by

Nicola Menegazzo

In Partial Fulfillment
of the Requirements for the Degree
Doctor of Philosophy in Chemistry

Georgia Institute of Technology
May 2007

A NOVEL APPROACH TO DIAMONDLIKE CARBON BASED MID-INFRARED ATTENUATED TOTAL REFLECTANCE SPECTROELECTROCHEMISTRY

Approved by:

Dr. Boris Mizaikoff, Advisor
School of Chemistry and Biochemistry
Georgia Institute of Technology

Dr. Jiři Janata
School of Chemistry and Biochemistry
Georgia Institute of Technology

Dr. Lawrence Bottomley
School of Chemistry and Biochemistry
Georgia Institute of Technology

Dr. William Hunt
School of Electrical and Computer Engineering
Georgia Institute of Technology

Dr. Miroslawa Josowicz
School of Chemistry and Biochemistry
Georgia Institute of Technology

Date Approved: November 6, 2006

Compton: "The Italian navigator has landed in the New World."

Conant: "How were the natives?"

Compton: "Very friendly."

From Arthur Compton's announcement to James Conant (chairman of the National Defense Research Committee) that Enrico Fermi had successfully achieved a self-sustained nuclear chain reaction on December 2nd, 1942.

ACKNOWLEDGEMENTS

Several people have been involved in the development of this work. I ask for the forgiveness of those individuals whose names are not mentioned here, as there would be too many for all to be included in the space allotted.

I would like to thank Dr. Boris Mizaikoff and Dr. Christine Kranz for giving me the opportunity of working with them over the span of my graduate studies. Together, they provided a highly creative environment allowing nearly unrestricted exploration of countless topics, interests and ideas. I'm equally indebted to both past and present members of the Applied Sensors Laboratory for sharing their knowledge in the lab, and companionship outside.

Dr. Jiři Janata, Dr. Miroslawa Josowicz, Dr. Lawrence Bottomley and Dr. William Hunt are gratefully acknowledged for serving as committee members and for scientific discussions undertaken on numerous occasions.

In addition, I would like to thank the Thin Film Technology group at the Laser Center Leoben headed by Dr. Wolfgang Waldhauser, as well as Dr. Roger J. Narayan and Dr. Chunming Jin at the University of North Carolina (Chapel Hill) for collaborating in the DLC portion of this work. Financial support from the ExxonMobil Research and Engineering Company in Annandale (NJ) is also acknowledged.

Finally, all of this would not have been possible without the unconditional support I received from my family throughout all my studies. Thank you!

TABLE OF CONTENTS

LIST OF TABLES

LIST OF FIGURES

LIST OF ABBREVIATIONS

2-VP	2-vinylpyridine
4-VP	4-vinylpyridine
a-C	Amorphous carbon
a-C:H	Hydrogenated amorphous carbon
AFM	Atomic force microscopy
AgQRE	Silver quasi reference electrode
ATR	Attenuated total reflectance
BDD	Boron doped diamond
CV	Cyclic voltammetry
CVD	Chemical vapor deposition
DC	Direct current
DLC	Diamondlike carbon
EELS	Electron energy loss spectroscopy
EMIRS	Electrochemically modulated infrared spectroscopy
FT	Fourier transform
FWHM	Full width at half maximum
IR	Infrared
KRS-5	Thallium bromoiodide
LEED	Low energy electron diffraction
MCT	Mercury-cadmium-telluride
NDD	Nitrogen doped diamond

NEXAFS	Near-edge X-ray absorption fine structure
NHE	Normal hydrogen electrode
NMR	Nuclear magnetic resonance
PANI	Polyaniline
PECVD	Plasma enhanced chemical vapor deposition
PLD	Pulsed laser deposition
PM-IRRAS	Polarization modulation infrared reflection-absorption spectroscopy
PtQRE	Platinum quasi reference electrode
RBS	Rutherford backscattering spectroscopy
RF	Radio frequency
SCE	Saturated calomel electrode
SECM	Scanning electrochemical microscopy
SEM	Scanning electron microscopy
SERS	Surface enhanced Raman spectroscopy
SHE	Standard hydrogen electrode
SIMS	Secondary ion mass spectrometry
SNIFTIRS	Substractively normalized interfacial Fourier transform infrared spectroscopy
STEM	Scanning transmission electron microscopy
Ta-C	Tetrahedral amorphous carbon
Ta-C:H	Tetrahedral hydrogenated amorphous carbon
TEM	Transmission electron microscopy
TIR	Total internal reflection
UME	Ultramicroelectrode

UV	Ultraviolet
Vis	Visible
XAS	X-ray absorption spectroscopy
XPS	X-ray photoelectron spectroscopy
ZnS	Zinc sulfide
ZnSe	Zinc selenide

SUMMARY

Structural changes of an electroactive species during an electrochemical reaction cannot be determined from the electroanalytical technique alone. By incorporating orthogonal spectroscopic techniques with electrochemistry, additional detailed information about the analyte structure, composition of the double layer and influence of electric fields on the analyte can be obtained during electrochemically responsive processes. Several spectroscopic methodologies have been specifically tailored for this purpose including electronic, ionic and vibrational spectroscopies. Mid-infrared ATR spectroscopy is especially interesting as it provides direct access to in-situ information about adsorbates at the electrode surface.

Mid-IR (2 – 20 μm) spectroelectrochemistry has been demonstrated for external reflection, transmission and internal reflection configurations. The work described in this thesis focuses on internal reflection spectroelectrochemistry since mass transport limitations, present in external reflection and transmission spectroelectrochemistry, are circumvented. Current limitations of appropriate electrode materials for the internal reflection configuration have hindered widespread adoption of this particular configuration. Therefore, a primary focus of this thesis is the development and coupling of electrically conducting DLC thin films with mid-IR transparent multi-reflection waveguides for attenuated total reflectance (ATR) spectroelectrochemistry.

Deposition processes of conducting diamondlike carbon (DLC) thin films were developed utilizing pulsed laser deposition systems in collaboration with Joanneum Research (Leoben, Austria) and at the University of North Carolina (Chapel Hill). Two

approaches aimed at improving the electrical conductivity of DLC were investigated: (1) doping with nitrogen and (2) incorporation of noble metal nanoclusters into the DLC matrix.

A detailed study on the composition of nitrogen-doped DLC layers showed that the fraction of sp^2-hybridized carbon is responsible for the observed electrochemical activity. Optical transparency in the mid-infrared regime was confirmed by transmission-absorption measurements after deposition of thin (~ 40 nm) DLC layers on zinc selenide (ZnSe) multi-reflection ATR waveguides. Additionally, the first application of conducting DLC films with mid-IR spectroelectrochemistry was demonstrated via the electropolymerization of polyaniline onto DLC-coated ATR elements.

Metal-DLC nanocomposite layers were extensively characterized with several analytical techniques in order to obtain detailed compositional information. The inclusion of metal nanoclusters substantially improves the electrical conductivity of the DLC layers, as demonstrated by the electrochemical activity measured. Lastly, sufficient mid-IR transmissivity was demonstrated from metal-DLC coated germanium waveguides to enable spectroelectrochemical application.

In addition, the electropolymerization of poly(4-vinylpyridine) in acetonitrile was pursued as a means for producing highly cross-linked ion exchange membranes for spectroelectrochemical sensing applications. The composition of the pre-polymerization mixture and deposition conditions were tailored to obtain uniformly coated electrodes. Thus, a suitable semipermeable membrane restricting the diffusion of cations to the electrode is obtained by performing the electropolymerization as established herein. By employing the described electropolymerization procedure at DLC-coated waveguides,

spectroelectrochemical sensing strategies can now feasibly be extended into the mid-IR regime.

1 INTRODUCTION

Thesis objective: The aim of this thesis was the development of electrically conducting diamondlike carbon (DLC) layers transparent in the mid-infrared spectral range, for simultaneous electrochemical and multi-reflection infrared attenuated total reflectance spectroscopic analysis. In addition, the mechanisms of establishing an ion-exchange membrane via electropolymerization of 4-vinylpyridine serving as an enrichment coating for spectroelectrochemical sensing applications have been studied at molecular level detail.

Original contributions of this thesis:

- In-situ monitoring of mid-IR spectral changes during electropolymerization processes via DLC-coated multi-reflection IR-ATR waveguides.(Chapter 3).
- Development and characterization of electrically conducting DLC layers (Chapters 3 and 4).
- Determination and characterization of poly(4-vinylpyridine) electropolymerization conditions in acetonitrile (Chapter 5).

This thesis is organized as follows:

Chapter 2 of this thesis provides the background and theory on infrared spectroscopic transduction principles, along with a discussion of the physical and electronic properties

of DLC. Furthermore, an introduction to the electrochemical techniques utilized for the characterization of conducting DLC is provided, along with the fundamental concepts of electropolymerized ion-exchange polymers.

Chapter 3 focuses on the physical and electrochemical characterization of nitrogen-doped DLC. The first experimental demonstration of spectroelectrochemistry with doped-DLC coated multi-reflection ATR waveguides is presented.

Chapter 4 presents an alternative concept to the studies in Chapter 3 discussing the physical, electrochemical, and spectroscopic properties of metal-DLC nanocomposite materials.

Chapter 5 provides a detailed analysis on the pre-polymerization conditions required for the electropolymerization of poly(4-vinylpyridine) as an ion-exchange membrane in acetonitrile.

Chapter 6 summarizes the obtained results and provides an outlook for continuation of this work.

1.1 Spectroelectrochemistry

The combination electrochemistry to orthogonal analytical techniques has pursued by electrochemists in an effort to acquire detailed information about electrochemical events occurring at the electrode surface (e.g. structure of the double layer, or of an adsorbate),

as well as information about products resulting from an electrochemical process. Several ex-situ techniques, such as X-ray photoelectron spectroscopy (XPS)[1] and secondary ion mass spectrometry (SIMS)[2] have been extensively applied to the analysis of electrode surfaces post-electrochemical reaction. However, these techniques require removal of the electrode from the electrolyte prior to spectroscopic analysis, which affects the arrangement of the electrode for continuation of electrochemical studies, and/or result in contamination of the surface upon exposure to the atmosphere.[3]

In contrast, in-situ techniques enable simultaneous monitoring of electrode surfaces as the electrochemical reaction proceeds, minimizing the potential to disturb the surface. Optical spectroelectrochemistry and nuclear magnetic resonance (NMR)[4] belong to this class of techniques, among others. Early reports on optical spectroelectrochemistry involved tin(IV) oxide coated glass slides transparent in the ultraviolet-visible (UV-Vis) range arranged perpendicularly to the incident light beam.[5] As a proof-of-concept, the authors utilized this configuration to spectroscopically monitor the oxidation of o-tolidine over time by properly selecting a wavelength where only the product was expected to absorb the incident radiation.

Shortly thereafter the authors extended their work by implementing the total internal reflectance (TIR) configuration, whereby the light beam is guided internally through the glass slide and spectroscopic sensing is perform via the evanescent field (See *Section 2.1.1*).[6] In contrast to conventional transmission measurements, where the bulk sample volume is analyzed and an average spectroscopic signature is obtained, the TIR approach offers the possibility of directly probing electrochemical events occurring at the electrode surface.

Continuing work utilizing the TIR configuration demonstrated the applicability of spectroelectrochemical platforms to sensing environments through the incorporation of solvent-casted ion-exchange coatings covering the OTE.[7-9] The addition of a functionalized partitioning layer (i.e. an ion-exchange polymer) prevents the interaction of potential interferants (e.g. cations in the case of an anion-exchange polymer) with the transduction mechanisms, facilitating measurements in complex matrices. In addition, compounds capable of diffusing through the polymer are enriched resulting in increased sensitivities. Hence, the realized sensing scheme is typically described as displaying three layers of selectivity as a means of accurately detecting the analyte of interest: (1) presence of absorption features corresponding to the analyte monitored, (2) electrochemical oxidation/reduction of the analyte at the applied potential, and (3) partitioning through the ion-exchange polymer. However, degradation of the polymer layer is a limitation of the sensors' temporal stability (~ 1 hr for a poly(dimethyldiallylammonium chloride)-SiO_2 layer).[8] Subsequent efforts utilizing highly cross-linked polymers, typically obtained by either introducing a cross-linking agent[7] or by electropolymerization,[10] lengthened the stability of the sensing platform to approx. 30 days.

However, absorption spectra obtained via UV-Vis spectroscopy are typically composed of broad features which render unambiguous identification of the electrochemical products difficult. In contrast, in the mid-IR range (2 – 20 μm) fundamental vibrational and rotational transitions of specific bonds are excited, yielding detailed absorption features corresponding to the structure of compound. Hence, extending

spectroelectrochemical sensing to the mid-IR range would provide a means to directly determine structural changes induced by the electrochemical reaction.

Metal films and grids, as well as electrically conducting IR-transparent materials have been utilized as OTEs for mid-IR spectroelectrochemistry with limited success (See *Section 2.1.2*). Poor transmissivity/conductivity or (electro)chemical lability of the OTE resulted in the limited adoption of this technique. Recently, electrically conducting polycrystalline diamond films have been introduced as alternative OTEs.[11, 12] Artificially grown boron doped diamond (BDD) displays several electrochemically advantageous properties,[13, 14] and in combination with optical transparency, present an extremely attractive approach to spectroelectrochemical analysis.

However, heavily doped BDD (> 0.1 % B) displays limited transmissivity in the mid-IR range, which has prevented its the widespread adoption as an OTE in that region.[11, 14] Further complications arise from the conditions required for chemical vapor deposition (CVD) of BDD, where substrate temperatures of up to 800 °C are utilized. In turn, this precludes deposition of BDD on common mid-IR transparent substrates such as zinc selenide (ZnSe), germanium and thallium bromoiodide (KRS-5) due to melting, cracking, and loss of optical transparency. Finally, considerable thermal expansion mismatch between BDD and most substrate materials generally leads to delamination.[15-20]

In order to circumvent these issues, Martin et al.[12] utilized thin BDD films (4 – 6 μm) deposited onto 50 μm thick silicon wafers pressed onto a single-reflection ZnSe internal reflection element. However, several limitations arise from their approach including significant reflection losses occurring at each optical interface, as well as reduced sensitivity due to the use of single-reflection ATR elements. Although auspicious results

were reported, Martin's contribution also illustrates some of the technical difficulties associated with using BDD for mid-IR spectroelectrochemistry.

Historically, contributions involving mid-IR spectroelectrochemistry have focused on the external reflection and transmission configurations to study adsorption processes at electrode surfaces and formation of electrolysis product, respectively. Hence, background information and relevant scientific achievements obtained with each technique will be discussed below.

The work presented in this thesis focuses on the development of a multi-reflection attenuated total reflectance (ATR) spectroelectrochemical platforms through the development and implementation of novel mid-IR transparent electrodes, which may subsequently be coupled to an ion-exchange membrane.

In both transmission and external reflection spectroelectrochemistry, the electrolyte layer must be kept at a minimum in order to avoid complete attenuation of the incident beam. With ATR, the analytical volume probed is determined by the penetration depth (d_p) of the evanescent field, which extends from the surface of the waveguide into the surrounding media. Provided that the electrolyte layer is greater than the d_p (i.e. > 2 μm, see *Table 2.1*), the total thickness will not influence the spectroscopic signal as contributions from absorbing species above the d_p are negligible (a detailed description of the theory and background of mid-IR-ATR spectroelectrochemistry will be presented in *Chapter 2*). The implication that molecular transport is not limited in the ATR configuration, enables the dynamic monitoring of electroactive species for sensing applications.

1.1.1 External reflection spectroelectrochemistry

In general, an external reflection configuration requires focusing of p-polarized IR radiation through an IR transparent window and a thin (≤ 50 μm) electrolyte layer. After the IR beam is subject to specular reflection at a solid metal electrode, it is coupled out through the electrolyte layer and the IR transparent window, and finally focused onto an IR-detection device.

A detailed description of the three most common spectroelectrochemical techniques devised for external reflection spectroscopy will be provided below. Significant scientific contributions obtained with each technique will also be discussed.

1.1.1.1 Electrochemically modulated infrared reflection spectroscopy (EMIRS)

Initial experiments involving potential modulation in an external reflection configuration were reported by Bewick et al.[21, 22] In general, an EMIRS experiment involves modulation of the potential applied at an electrode between a "base" potential (E_1), and a "step" potential (E_2) at a predetermined frequency (approx. 10 Hz[22, 23]). The infrared signal is attenuated in accordance to concentration changes due to the formation (or consumption) of the analyte with the applied potential. A phase-sensitive detector (i.e. a lock-in amplifier) is used to retrieve the analytical signal. The IR component displaying the same modulation as the applied potential square wave is detected and amplified. EMIRS was originally developed for dispersive IR spectrometers; therefore, spectra are obtained by incrementally changing the wavelength of the incident beam at each potential modulation. The demodulated infrared signal is plotted as the change in reflectivity between the two potentials ($\Delta R = R(E_2) - R(E_1)$) normalized by the reflectivity measured at the base potential, i.e. $\Delta R/R$, versus wavenumber ($\tilde{\nu}$).

With EMIRS, Bewick et al. reported large reflectivity changes at platinum electrodes immersed in 1 M H_2SO_4 upon potential modulation. The increased reflectivity was attributed to adsorption of hydrogen on the electrode at 0.5 V (vs. NHE).[22] Additional work using organic solvents demonstrated a potential dependency in the reversible adsorption of indole at platinum electrodes.[23]

Additional electrode adsorption studies were performed by Beden et al.[24] Their work provided insight on the poisoning of platinum surfaces during electrochemical oxidation of methanol. The authors claimed that, upon application of the square waveform (E_1 = 0.05V and E_2 = 0.95 V vs. NHE), changes in differential reflectivity demonstrated the adsorption of carbon monoxide onto the electrode.

Despite continuing work by Bewick et al.[25] and Kunimatsu et al.[26], EMIRS was not extensively developed due to the widespread adoption of Fourier transform (FT) IR spectrometers.

1.1.1.2 Subtractively normalized interfacial Fourier transform infrared spectroscopy (SNIFTIRS)

The incorporation of Fourier transformation and the Michelson interferometer into modern IR spectrometers, provided several breakthroughs for optical spectroscopy, including higher optical throughput and diminished sampling times due to the multiplex advantage. Concomitantly, spectroelectrochemical techniques employing FT-IR spectrometers were developed.[27]

As with EMIRS, in SNIFTIRS the electrode potential is repeatedly switched between E_1 and E_2. At each potential, several spectra are collected and averaged yielding improved signal-to-noise ratios. This process is repeated several times in order to minimize

contributions to the IR spectra from mechanical and electronic drift in the instrument. Small acquisition times also decreases the possibility of product accumulation within the thin electrolyte layer, which results in decreased reflectivity.[3]

The optical information is also plotted as the normalized reflectivity change obtained via the single beam spectra at the two applied potentials, similar to EMIRS.

The SNIFTIRS approach was initially used by Pons and co-workers[28] to study the structure of the double layer at platinum electrodes in acetonitrile containing 0.1 M tetrabutylammonium fluoroborate. The authors correlated the observed reflectivity changes at cathodic potentials (up to +2.5 V vs. Ag/Ag^{+}) to the adsorption of acetonitrile to the electrode surface. Additional work by the same authors was later extended to study the electrochemical generation of radical species.[29]

Recently, SNIFTIRS has been applied to the investigation of the self-assembly of 2-mercaptobenzimidazole on gold surfaces. Aside from duration of exposure and concentration of the thiol, it has been shown via difference reflectance spectra that the applied potential also influences the orientation of the monolayer.[30]

A notable development of SNIFTIRS is the incorporation of step-scan FT-IR. In contrast to conventional rapid-scan FT-IR, in step-scan mode spectra are collected by increasing the optical path in the interferometer block in discrete increments. A full mid-IR spectrum can be collected in ~ 1 μs (depending upon the increment "spacing") compared to a ~ 100 ms for conventional rapid-scan FT-IR. Hence, this technique permits the investigation of fast electrochemical processes.[31, 32]

1.1.1.3 Polarization modulation infrared reflection absorption spectroscopy (PM-IRRAS)

Conversely to the potential modulation techniques previously described, PM-IRRAS relies upon modulation of the IR beam between s- and p-polarization. PM-IRRAS relies upon the difference in the interaction of s- and p-polarized light with substances adsorbed at the electrode. At the reflection point, the incident and reflected light beams combine to form a standing wave. The electric field resulting from s-polarized light displays nearly zero intensity at the electrode surface (with a maximum intensity at approx. one wavelength from the surface). In contrast, the electric field originating from p-polarized light has nearly equal intensity up to one wavelength from the surface.[3] The intensity of the standing wave increases with the angle of incidence reaching a maximum at grazing angles.[33] Therefore, p-polarized light will be absorbed by molecules adsorbed at the electrode, whereas s-polarized will not. Furthermore, dipole moments oriented parallel to the electrode surface are not excited. Hence, surface selection rules provide additional information about the orientation of the adsorbate.[34]

In contrast to the previously discussed techniques, PM-IRRAS spectra can be acquired at a single electrode potential and are presented as $(I_p - I_s) / (I_p + I_s)$ versus $\tilde{\nu}$. However, in order to exclude contributions from the bulk solvent, the ratio of the spectra at two distinct potentials is required.[35] Conventional IR absorption spectra of adsorbate material are obtained with this technique in contrast to the "difference" spectra obtained via EMIRS and SNIFTIRS. Therefore, complete structural information about the adsorbed molecule can be retrieved.

PM-IRRAS was initially employed to investigate the adsorption of carbon monoxide onto platinum electrodes by Russel et al.[36] Their results corroborated original EMIRS findings

by Beden et al.[24] indicating that platinum surfaces are poisoned by carbon monoxide during the electrochemical oxidation of methanol.

In addition to electrode adsorption studies, the PM-IRRAS technique has been extended to investigations of structural changes, including desorption, of self-assembled monolayer with respect to the applied potential.[37, 38]

1.1.2 Transmission spectroelectrochemistry

Due to the simplicity of the setup, the transmission configuration was investigated early in the development of spectroelectrochemical techniques. In principle, a sufficiently transparent electrode is pressed between two IR transparent windows and is filled with an electrolyte solution. Similar to the external reflection configuration, a thin electrolyte layer (≤ 50 μm) must be employed to prevent total attenuation of the incident beam. Gold metal grids are typically used as working electrodes.[6, 39]

The infrared beam in the transmission configuration probes the entire analytical volume of the electrochemical cell, therefore, this technique is restricted to monitoring the formation of products by electrolysis.[34, 40]

Initial reports on this technique involved monitoring changes in the IR transmission spectra during the electrochemical reduction of ninhydrin in acetonitrile.[41] The authors reported on the rise of several spectroscopic features confirming the presence of reduction products.

Recently, this technique was applied to the analysis of Li^+ batteries. The diffusion process of lithium from $LiFePO_4$ (the cathode material) was monitored by following the absorption bands corresponding to the phosphate group during discharging of the battery.[42]

Since the analytical information obtained via the transmission configuration is not restricted to surface events, additional development has not been pursued to the same extend as other mid-IR spectroelectrochemical configurations.

1.2 References

1. Ilangovan, G.; Pillai, K. C., *Electrochemical and XPS Characterization of Glassy Carbon Electrode Surface Effects on the Preparation of a Monomeric Molybdate(VI)-Modified Electrode*, Langmuir, **13 (3)**, 566-575, (1997).

2. Valov, I.; Korte, C.; De Souza, R. A.; Martin, M.; Janek, J., *Electrochemical Incorporation of Nitrogen into a Zirconia Solid Electrolyte*, Electrochem. Solid-State Lett., **9 (5)**, F23-F26, (2006).

3. Bard, A. J.; Editor, *Electroanalytical Chemistry*. 1986; Vol. 14, p 459.

4. Babu, P. K.; Oldfield, E.; Wieckowski, A., *NMR and voltammetric study of dynamics at electrochemical interfaces*, Abstracts of Papers, 224th ACS National Meeting, Boston, MA, United States, August 18-22, 2002, COLL-309, (2002).

5. Kuwana, T.; Darlington, R. K.; Leedy, D. W., *Electrochemical studies using conducting glass indicator electrodes*, Anal. Chem., **36 (10)**, 2023-2025, (1964).

6. Hansen, W. N.; Osteryoung, R. A.; Kuwana, T., *Internal reflection spectroscopic observation of electrode-solution interface*, J. Am. Chem. Soc., **88 (5)**, 1062-1063, (1966).

7. Conklin, S. D.; Heineman, W. R.; Seliskar, C. J., *Spectroelectrochemical sensing based on multimode selectivity simultaneously achievable in a single device. 18. Preparation and characterization of cross-linked quaternized poly(4-vinylpyridinium) films*, Electroanalysis, **17 (15-16)**, 1433-1440, (2005).

8. Stegemiller Michael, L.; Heineman William, R.; Seliskar Carl, J.; Ridgway Thomas, H.; Bryan Samuel, A.; Hubler, T.; Sell Richard, L., *Spectroelectrochemical sensing based on multimode selectivity simultaneously achievable in a single device. 11. Design and evaluation of a small portable sensor for the determination of ferrocyanide in Hanford waste samples*, Environmental science & technology, **37 (1)**, 123-130, (2003).

9. Heineman, W. R.; Seliskar, C. J.; Richardson, J. N., *Spectroelectrochemical sensing based on multimode selectivity simultaneously achievable in a single device: An overview*, Aust. J. Chem., **56 (2-3)**, 93-102, (2003).

10. Teng, F. S.; Mahalingam, R.; Subramanian, R. V.; Raff, R. A. V., *Polymer film coatings on metal electrodes through electroinitiated polymerization and their evaluation*, J. Electrochem. Soc., **124 (7)**, 995-1006, (1977).

11. Zak, J. K.; Butler, J. E.; Swain, G. M., *Diamond Optically Transparent Electrodes: Demonstration of Concept with Ferri/Ferrocyanide and Methyl Viologen*, Anal. Chem., **73 (5)**, 908-914, (2001).

12. Martin, H. B.; Morrison, P. W., Jr., *Application of a diamond thin film as a transparent electrode for in situ infrared spectroelectrochemistry*, Electrochem. Solid-State Lett., **4 (4)**, E17-E20, (2001).

13. Witek, M.; Wang, J.; Stotter, J.; Hupert, M.; Haymond, S.; Sonthalia, P.; Swain, G. M.; Zak, J. K.; Chen, Q.; Gruen, D. M.; Butler, J. E.; Kobashi, K.; Tachibana, T., *Summary of recent progress with diamond electrodes in electroanalysis, spectroelectrochemistry and electrocatalysis*, J. Wide Bandgap Mater., **8 (3-4)**, 171-188, (2002).

14. Swain, G. M., *Electrically Conducting Diamond Thin Films: Advanced Electrode Materials for Electrochemical Technologies*. Marcel Dekker, Inc.: New York, 2004; Vol. 22, p 181-277.

15. Michler, J.; Mermoux, M.; von Kaenel, Y.; Haouni, A.; Lucazeau, G.; Blank, E., *Residual stress in diamond films: origins and modelling*, Thin Solid Films, **357 (2)**, 189-201, (1999).

16. Diniz, A. V.; Ferreira, N. G.; Corat, E. J.; Trava-Airoldi, V. J., *Boron doped diamond thin films on large area Ti6Al4V substrates for electrochemical application*, Materials Research (Sao Carlos, Brazil), **6 (1)**, 57-61, (2003).

17. Peng, X. L.; Tsui, Y. C.; Clyne, T. W., *Stiffness, residual stresses and interfacial fracture energy of diamond films on titanium*, Diamond Relat. Mater., **6 (11)**, 1612-1621, (1997).

18. Chalker, P. R.; Jones, A. M.; Johnston, C.; Buckley-Golder, I. M., *Evaluation of internal stresses present in chemical vapor deposition diamond films*, Surf. Coat. Technol., **47 (1-3)**, 365-374, (1991).

19. Guo, H.; Alam, M., *Strain in CVD diamond films: effects of deposition variables*, Thin Solid Films, **212 (1-2)**, 173-179, (1992).

20. Schwarzbach, D.; Haubner, R.; Lux, B., *Internal stresses in CVD diamond layers*, Diamond Relat. Mater., **3 (4-6)**, 757-764, (1994).

21. Bewick, A.; Kunimatsu, K.; Pons, B. S.; Russell, J. W., *Electrochemically modulated infrared spectroscopy (EMIRS). Experimental details*, J. Electroanal. Chem. Interfac., **160 (1-2)**, 47-61, (1984).

22. Bewick, A.; Kunimatsu, K., *Infrared spectroscopy of the electrode-electrolyte interphase*, Surf. Sci., **101 (1-3)**, 131-138, (1980).

23. Bewick, A.; Kunimatsu, K.; Pons, B. S., *Infrared spectroscopy of the electrode-electrolyte interphase*, Electrochim. Acta, **25 (4)**, 465-468, (1980).

24. Beden, B.; Lamy, C.; Bewick, A.; Kunimatsu, K., *Electrosorption of methanol on a platinum electrode. IR spectroscopic evidence for adsorbed carbonyl species*, J. Electroanal. Chem. Interfac., **121**, 343-347, (1981).

25. Bewick, A.; Russell, J. W., *Structural investigation by infra-red spectroscopy of adsorbed hydrogen on platinum*, J. Electroanal. Chem. Interfac., **132**, 329-344, (1982).

26. Kunimatsu, K., *The infrared spectrum of linearly adsorbed carbon monoxide species produced by chemisorption of methanol on a smooth platinum electrode at high anodic potentials*, J. Electroanal. Chem. Interfac., **145 (1)**, 219-224, (1983).

27. Korzeniewski, C.; Pons, S., *In situ infrared spectroelectrochemistry*, Journal of Vacuum Science & Technology, B: Microelectronics and Nanometer Structures, **3 (5)**, 1421-1424, (1985).

28. Davidson, T.; Pons, B. S.; Bewick, A.; Schmidt, P. P., *Vibrational spectroscopy of the electrode/electrolyte interface. Use of Fourier transform infrared spectroscopy*, J. Electroanal. Chem. Interfac., **125 (1)**, 237-241, (1981).

29. Pons, S., *The use of Fourier transform infrared spectroscopy for in situ recording of species in the electrode-electrolyte solution interphase*, J. Electroanal. Chem. Interfac., **150 (1-2)**, 495-504, (1983).

30. Doneux, T.; Buess-Herman, C.; Hosseini, M. G.; Nichols, R. J.; Lipkowski, J., *Adsorption of 2-mercaptobenzimidazole on a Au(111) electrode*, Electrochim. Acta, **50 (21)**, 4275-4282, (2005).

31. Pharr, C. M.; Griffiths, P. R., *Step-scan FT-IR spectroelectrochemical analysis of surface and solution species in the ferricyanide/ferrocyanide redox couple*, Anal. Chem., **69 (22)**, 4665-4672, (1997).

32. Zhou, Z.-Y.; Sun, S.-G., *In situ step-scan time-resolved microscope FTIR spectroscopy applied in irreversible electrochemical reactions*, Electrochim. Acta, **50 (25-26)**, 5163-5171, (2005).

33. Greenler, R. G., *Reflection method for obtaining the infrared spectrum of a thin layer on a metal surface*, J. Chem. Phys., **50 (5)**, 1963-1968, (1969).

34. Christensen, P. A.; Hamnett, A., *In-situ infrared studies of the electrode-electrolyte interface*, Compr. Chem. Kinet., **29**, 1-77, (1989).

35. Korzeniewski, C., *Infrared spectroscopy in electrochemistry: new methods and connections to UhV surface science*, Crit. Rev. Anal. Chem., **27 (2)**, 81-102, (1997).

36. Russell, J. W.; Overend, J.; Scanlon, K.; Severson, M.; Bewick, A., *Infrared spectrum of carbon monoxide on a platinum electrode in acidic solution*, J. Phys. Chem., **86 (16)**, 3066-3068, (1982).

37. Zawisza, I.; Lipkowski, J., *Layer by Layer Characterization of 1-Octadecanol Films on a Au(111) Electrode Surface. "In Situ" Polarization Modulation Infrared Reflection Absorption Spectroscopy and Electrochemical Studies*, Langmuir, **20 (11)**, 4579-4589, (2004).

38. Ye, S.; Yashiro, A.; Sato, Y.; Uosaki, K., *Electrochemical in situ FT-IRRAS studies of a self-assembled monolayer of 2-(11-mercaptoundecyl)hydroquinone*, J. Chem. Soc., Faraday Trans., **92 (20)**, 3813-3821, (1996).

39. Atwood, C. G.; Geiger, W. E., *Investigations of Time-Dependent Delocalization and the Correlation of Carbonyl IR Shifts with DE1/2 Values for Hydrocarbon-Linked Class II and Class III Mixed-Valent Complexes*, J. Am. Chem. Soc., **122 (23)**, 5477-5485, (2000).

40. Christensen, P. A., *In situ infrared spectroelectrochemistry*, Encyclopedia of Electrochemistry, **3**, 530-571, (2003).

41. Heineman, W. R.; Burnett, J. N.; Murray, R. W., *Optically transparent thin-layer electrodes: ninhydrin reduction in an infrared transparent cell*, Anal. Chem., **40 (13)**, 1974-1978, (1968).

42. Burba, C. M.; Frech, R., *In situ transmission FTIR spectroelectrochemistry: A new technique for studying lithium batteries*, Electrochim. Acta, **52 (3)**, 780-785, (2006).

2 BACKGROUND

This chapter introduces the background and theory of the mid-infrared spectroelectrochemical platform described in this thesis. Furthermore, the principles of attenuated total reflectance spectroscopy including limitations of current working electrodes for multi-reflection mid-IR ATR spectroelectrochemistry are discussed. Diamondlike carbon (DLC) is presented as a novel alternative, and details on its composition and the electronic properties are discussed. An introduction to the electrochemical techniques used for the investigation of DLC electrodes is provided. Finally, studies on the electropolymerization process of redox polymers and their application to mid-IR spectroelectrochemistry are presented.

2.1 Attenuated total reflectance spectroscopy

2.1.1 Principles of ATR

In total internal reflectance (TIR), radiation is propagated through an optically dense waveguide (n_1) surrounded by an optically rarer medium (n_2; with $n_1 > n_2$).[1] Radiation propagating towards the interface between the waveguide and the surrounding medium at incident angles greater than the critical angle (θ_c) will be totally internally reflected. The critical angle can be described as a function of the refractive indices of the waveguide and the surrounding medium:

$$\theta_c = \sin^{-1} \frac{n_2}{n_1} \tag{2.1}$$

At each internal reflection a standing wave is formed, and the corresponding electrical field, commonly referred to as the *evanescent field*, extends into the surrounding medium. The intensity of the evanescent field decays exponentially with the distance from the optical interface following:

$$E(z) = E_o - \exp^{\left(\frac{-z}{d_p}\right)}, \tag{2.2}$$

where E_O is the intensity of the evanescent field at the surface of the waveguide (i.e. $z = 0$), and d_p is the penetration depth of the evanescent field, which is defined as the distance where the intensity of the evanescent field decays to a value of 1/e. The penetration depth is dependent upon the refractive indices of the waveguide and the surrounding medium, as well as the wavelength and incident angle of the propagated radiation:

$$d_p = \frac{\lambda}{2\pi\sqrt{n_1^2 \sin^2 \theta - n_2^2}} \tag{2.3}$$

The principle of TIR is graphically illustrated in *Figure 2.1*.

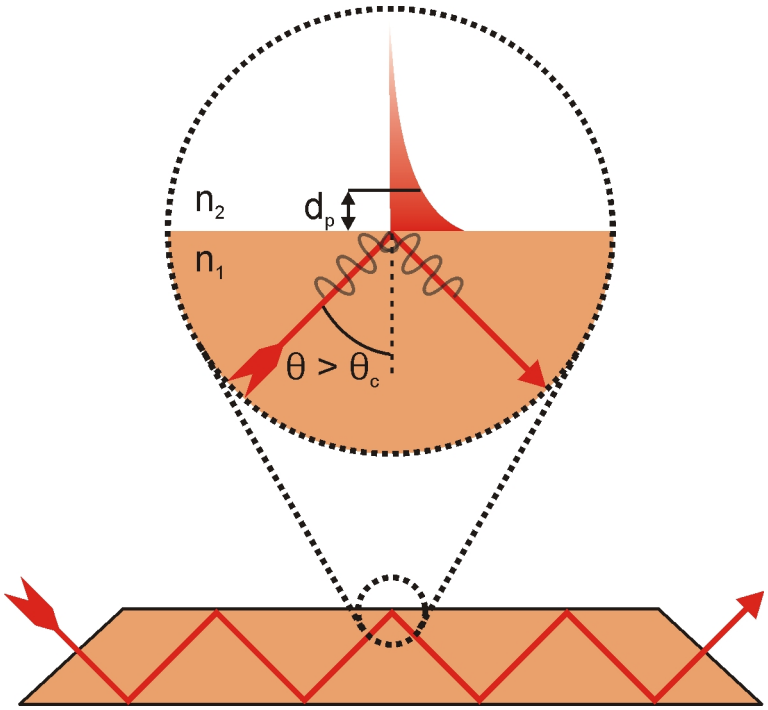

Figure 2.1: Schematic representation of the TIR principle.

The interaction of absorbing analytes in optical contact with the evanescent field results in attenuated total reflection (ATR) spectra.[2] For wavelengths corresponding to the mid-infrared region (2-20 µm) the energy transfer between the evanescent field and the absorbing analyte results in the excitation of fundamental vibrational and rotational modes of specific molecular bonds. Analysis of the absorption features consequently provides qualitative and quantitative information on the chemical functionalities of the analyte.

The analytical volume probed in IR-ATR spectroscopy is determined by the penetration depth of the evanescent field, and facilitates the analysis of samples typically unsuitable for transmission or reflection IR spectroscopy. Highly scattering samples, such as turbid solutions and powders, are routinely analyzed with IR-ATR spectroscopy.[3, 4] For

comparison, estimated penetration depths for infrared transparent materials commonly manufactured into ATR elements are summarized in *Table 2.1*.

Table 2.1: Penetration depths of common IR transparent materials in contact with water (n_2 = 1.33, θ = 45 °)

Material	Refractive index (at 5 µm)	Penetration depth (µm) 14.3 µm (700 cm^{-1})	2.5 µm (4000 cm^{-1})
Zinc sulfide	2.25	2.61	0.46
Thallium bromoiodide (KRS-5)	2.38	2.21	0.39
Zinc selenide	2.43	2.09	0.37
Silicon	3.42	1.13[a]	0.20
Germanium	4.01	0.91	0.16

[a] Although the penetration depth for silicon at 14.3 µm can be approximated, the material is optically opaque up to ~ 6.7 µm.

As the penetration depth can be described in simple mathematical terms, it has become common practice to characterize an ATR setup by the achieved penetration depth. However, d_p is only a nominal figure, and the effective spectroscopically probed volume is somewhat larger due to its exponential decay. The maximum distance from the optical interface from which analytical information on a sample can be obtained is defined as the effective sample thickness (d_e).[1] The relationship between attenuation at a single reflection point and the sample absorption properties is established via d_e:[5]

$$\ln R(\tilde{\nu}) = -\varepsilon c d_e , \tag{2.4}$$

where ε is the molar absorptivity and c is the sample concentration. For attenuation occurring at N reflection points, E*quation 2.4* becomes

$$\ln R(\tilde{v}) = -\varepsilon c d_e N \tag{2.5}$$

Equations 2.4 and *2.5* are similar to those obtained for conventional transmission absorption spectroscopy:[5]

$$\ln T = \ln \frac{I}{I_o} = -\varepsilon c d \ , \tag{2.6}$$

where T is the transmittance, I is the transmitted intensity and I_o is the incident intensity. Therefore, d_e also represents the sample thickness required to obtaining the same absorption as in a corresponding transmission measurement with a sample thickness equal to d.

2.1.2 Spectroelectrochemistry with mid-IR ATR

The simultaneous application of orthogonal transduction principles has attracted significant interest in sensor technology, since detailed information on several analytes can be acquired in one measurement step. As an example, the combination of mid-IR spectroscopy and electrochemistry enables the direct evaluation of the bonding arrangement in a molecule with respect to a changing electrochemical environment. Historically, transmission and external reflection spectroscopy have been the preferred measurement modes for IR spectroelectrochemistry, due to readily available electrode materials. In transmission mode, the electrochemical cell is placed perpendicular to the incident IR beam, whereas in external reflection mode the IR beam is reflected off of the electrode surface and subsequently guided towards the detector.[6] The requirements for the electrode materials vary for each technique. For example, in transmission mode the

electrode must provide sufficient transmissivity (*Figure 2.2(a)*), while for the external reflection mode the electrode must exhibit a mirror finish in order to minimize scattering losses (*Figure 2.2(b)*).

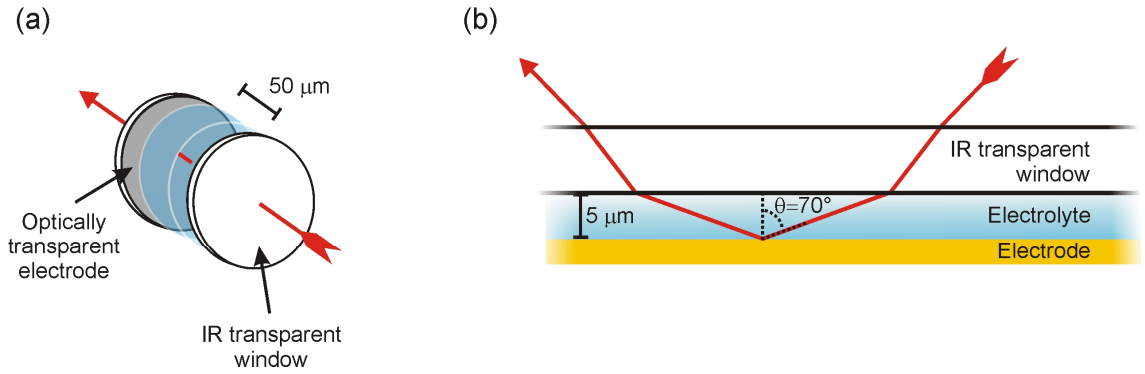

Figure 2.2: Schematic for spectroelectrochemical analysis in (a) transmission and (b) external reflection mode.

As electrochemical experiments are typically performed in aqueous solutions, thin electrolyte layers (< 50 µm) are required to avoid total absorbance of the incident radiation by the solvent. Concomitantly, thin electrolyte layers induce high solution resistance distorting the electrochemical signal.[7] Additionally, reagent depletion and product accumulation, as well as localized pH and ionic strength changes are commonly observed in these configurations.[8-10]

In ATR mode, the pathlength is determined by the penetration depth of the evanescent field. Thus, the propagation of IR radiation is not affected by the thickness of the electrolyte layer on top of the waveguide. Therefore, IR-ATR spectroelectrochemistry circumvents the limitations imposed upon the electrolyte layer by transmission and external reflection spectroscopy.

Although IR-ATR spectroelectrochemistry has been acknowledged as a viable configuration, the absence of appropriate IR-transparent electrode materials has limited the widespread adoption of this technique to date.[11, 12] Hence, the goal of this thesis was the introduction of conducting diamondlike carbon (DLC) as a novel electrode material for multi-reflection IR-ATR spectroelectrochemistry.

Single-reflection ATR configurations using metal films with thicknesses of up to 40 nm have been reported.[13-15] However, with metal films the intensity of the evanescent field rapidly attenuates within tens of nanometers (e.g. ~ 50 nm for a copper film at $\tilde{\nu} = 5$ µm[16]) due to the high absorption coefficient of free charge carriers[12], which limits their application to single-reflection configurations. Since the probed sample volume (i.e. d_e) increases with the number of internal reflections (*Equation 2.5*), improved sensitivity for analytes at low concentration levels is expected using multi-reflection ATR elements. However, for spectroelectrochemical systems the incident beam will be additionally attenuated by the metal at each reflection point. To avoid total attenuation of the incident beam, thinner metal films (≤ 10 nm) have been utilized in multi-reflection IR-ATR spectroelectrochemistry.[17-19]

Pham et al.[20] employed an iron-coated germanium waveguide to study the electropolymerization reaction of 2,6-dimethylphenol in methanol via cyclic voltammetry. In their investigations, the authors observed that methanol desorbed from the electrode at approx. +0.5 V (vs. AgQRE), corresponding to the oxidation potential of the monomer. By continuing the potential sweep to +2.5 V (vs. AgQRE), several IR absorption bands increased in intensity, corresponding to the precipitation of the polymer onto the electrode. Simultaneously, IR bands attributed to methanol decreased in

intensity, as the solvent was being displaced from the volume probed by the evanescent field, due to polymer formation.

Additional studies by the same authors[21] utilizing platinum-coated germanium waveguides were directed towards the electrochemical oxidation of methanol. The authors reported on the adsorption of carbon monoxide onto the platinum film during the electrochemical reaction. Iron-coated germanium waveguides were also employed by Neugebauer et al.[22] to investigate the oxidation of iron in 5 M KOH. The authors reported on the rise of a broad absorption band at ~ -0.8 V (vs. PtQRE) attributes to the formation of $Fe(OH)_2$ at the electrode surface.

However, transparent metal films present an additional challenge, since films with thicknesses below ~ 10 nm are usually composed of metal islands with limited electrical conductivity.[23-25] Furthermore, the stability of thin metal island films in solution is limited due to spalling.[21, 26]

Alternatively, metal grids pressed onto mid-IR ATR waveguides have been applied as working electrodes.[27, 28] For example, Zimmerann et al.[28] patterned the surface of a zinc selenide ATR waveguide with gold metal in order to obtain a grid design. This configuration enabled the study of the electropolymerization process for polyaniline during the first potential sweep cycles (0 to +1 V vs. SHE). Their observations led to the conclusion that chain propagation occurs mainly during the reverse cathodic sweep, as the IR bands increased in intensity almost exclusively during that step.

This approach yields highly conducting electrodes, however, due to incomplete coverage of the waveguide the electrochemical generation of absorbing species will be highly localized, resulting in a lower sensitivity compared to a uniformly coated waveguide.

Finally, doped germanium mid-IR waveguides serving simultaneously as working electrodes were first demonstrated by Mark et al.[29] In their work, changes in the IR-ATR spectra were observed during the reduction of 8-quinolinol to dihydro-8-quinolinol, and during the oxidation of the tetramethylbenzidine radical to tetramethylbenzidine. However, the authors commented that corrosion of the germanium electrode had occurred during the oxidation reaction. The corrosion behavior of germanium waveguides upon exposure to anodic potentials was subsequently confirmed by several other reports.[30-32]

Despite encouraging results obtained with the electrode configurations described above, mid-IR ATR spectroelectrochemistry with multi-reflection waveguides requires the development of robust, highly transparent, conducting electrode materials. Diamondlike carbon (DLC) is an IR transparent material with electrically conducting properties upon appropriate doping. The physical, electronic, and spectroscopic properties of DLC will be discussed in detail in *Section 2.2*.

2.2 Diamondlike carbon

2.2.1 Introduction

The term diamondlike carbon (DLC) was originally employed by Aisenberg and Chabot referring to thin amorphous carbon films exhibiting physical and chemical properties similar to diamond.[33] Presently, carbon films displaying high densities (~ 3.0 g/cm^3), high hardness (~ 60 GPa), IR transparency, extensive chemical inertness, and the absence of any long-range ordering are defined as "diamondlike".[34-36] Structurally, DLC is a metastable allotrope of carbon composed of a mixture of sp^3- and sp^2-hybridized carbon, which is incorporated into an amorphous matrix.[37]

Depending upon the chemical composition of DLC, two types of layers can be discriminated: hydrogenated and hydrogen-free DLC. Hydrogenated films are deposited from hydrocarbon sources, or in the presence of hydrogen gas, and can contain up to 60 % hydrogen. In contrast, hydrogen-free films are deposited using solid graphite sources either in vacuum or in the presence of noble gases. Hydrogen-free DLC typically contains < 1 % hydrogen. Hydrogenated layers generally exhibit lower hardness values, lower wear resistance, and lower thermal stability compared to hydrogen-free DLC.[38] Furthermore, each type of DLC layer can be further subdivided into two additional groups based upon the fraction of sp^3-hybridized carbon present in the film. The different compositional arrangements are graphically represented in the form of a ternary phase diagram in *Figure 2.3*.

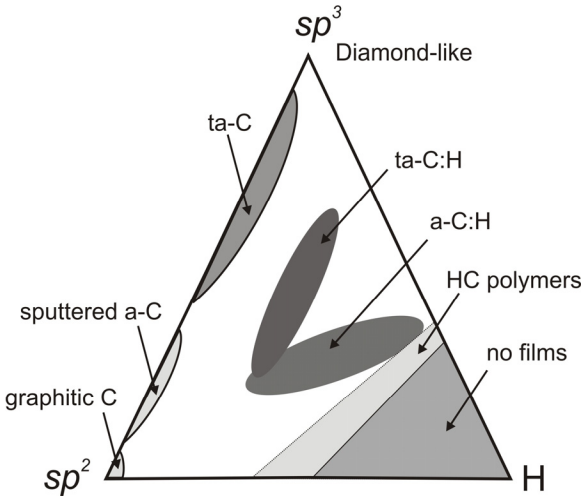

Figure 2.3: Ternary phase diagram displaying the possible compositions of diamondlike carbon layers (reproduced from Robertson[39]).

With meticulous control on the deposition parameters including substrate temperature, deposition pressure, hydrogen content, and energy of the carbon formed species, high quality DLC layers are deposited.

The mechanical properties of DLC can be directly correlated to the fraction of sp^3-hybridized carbon in the layer.[40, 41] Therefore, it is evident that for tribological applications the most desirable DLC films are characterized by a high sp^3-content, referred to as tetrahedral amorphous carbon, or ta-C. Different analytical techniques have been applied to directly quantify the sp^3-carbon content, including near-edge x-ray absorption fine structure (NEXAFS) analysis,[42] ^{13}C nuclear magnetic resonance (NMR) analysis,[43] electron energy loss spectroscopy (EELS),[44] x-ray photoelectron spectroscopy (XPS),[45] x-ray induced Auger electron spectroscopy[46] and, more recently, ultraviolet Raman spectroscopy.[47] Due to their unique physical properties, DLC films have found widespread adoption in mechanically demanding applications, such as the automotive, textile, and medical fields. A detailed listing of consumer products utilizing DLC as a protective layer has recently been published by Hauert et al.[48]

In addition to their mechanical robustness, DLC layers are also chemically inert and transparent over a wide spectral range (2 – 50 μm).[36, 49] These properties have recently been exploited in multi-reflection ATR spectroscopic studies of chemically aggressive agents (e.g. 0.5-10 % hydrogen peroxide solutions).[50, 51] Thin, optically transparent DLC protective layers deposited onto ZnSe waveguides prevented degradation of the waveguide substrate. Furthermore, recently developed conducting DLC layers generated interest for using DLC as novel carbon electrodes with electrochemical properties similar to those of boron doped diamond.[52-54]

However, despite their beneficial chemical, optical, and electrochemical properties, the analytical applications of DLC layers remains surprisingly small to date. In particular, the combination of mid-IR transparent DLC with improved electrical conductivity enables the development of superior multi-reflection spectroelectrochemical ATR platforms currently limited by the absence of sufficiently transparent electrode materials.

2.2.2 Pulsed laser deposition (PLD) of DLC

DLC deposition has been performed with several deposition techniques, including plasma enhanced chemical vapor deposition (PECVD),[55] DC[56] and RF[57] (magnetron) sputtering, cathodic arc deposition,[58] ion beam deposition,[33] and pulsed laser deposition (PLD)[59]. The properties of the resulting DLC thin film are dependent upon the deposition method due to the energy of the created carbon species (e.g. ~ 4 eV for near-IR-PLD[37] vs. ~ 140 eV for filtered cathodic arc deposition[58]) and the carbon source (e.g. gaseous hydrocarbons vs. graphite).

The PLD technique is most versatile, since DLC layers with a wide range of chemical, optical and mechanical properties can be obtained by tuning the deposition process.[37] In this technique, laser pulses (< 30 ns) ablate small sections of a carbon target in an evacuated stainless steel chamber ($< 8 \times 10^{-6}$ Torr). The resulting plume is composed of carbon ions, atoms, and clusters, which are accelerated towards the substrate and condense as thin film at the substrate surface (*Figure 2.4(a)*). Hydrogenated layers are deposited from hydrocarbon sources[60] (e.g. polycarbonate), whereas hydrogen-free layers are obtained by ablation of high purity graphite targets at inert atmospheres.[59] Layers with a high fraction of sp^3-hybridized carbon (i.e. ta-C) are deposited by performing the ablation process with UV lasers (e.g. excimer lasers).[37, 61, 62]

Furthermore, this technique enables straightforward incorporation of additional elements into the carbon matrix resulting in doped DLC layers with specifically tailored properties, such as improved hardness[35], or electrical conductivity[63]. Modifiers can be included via the ablation of the carbon source in the presence of a reactive gas,[64] by sequentially focusing the laser beam onto different targets (e.g. *Figure 2.4(b)*)[65], or by intimately mixing the carbon source with the desired modifier.[66]

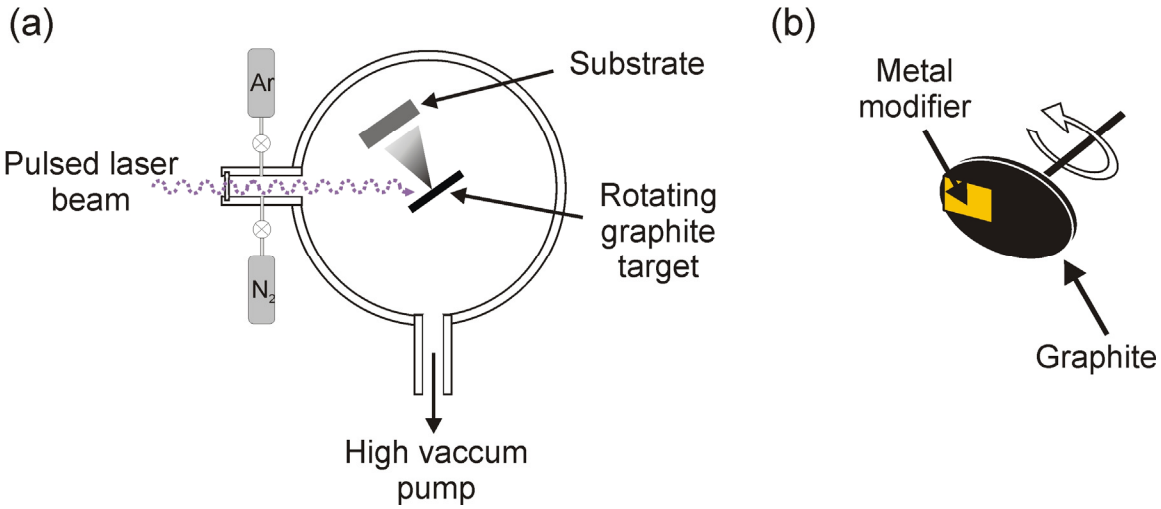

Figure 2.4: Schematic representation of (a) pulsed laser deposition chamber, and (b) metal-graphite hybrid target used for the deposition of nanocomposite materials (Chapter 4).

2.2.3 Electronic properties

Unlike amorphous silicon, DLC contains a significant fraction of sp^2-hybridized carbon atoms clustered into six-membered rings.[67] The presence of π electron density introduces tail bands at the edges of the σ (and σ*) bands, thereby decreasing the band gap in DLC.[68] Initial approaches towards modeling the band gap resulted in the following mathematical representation:

$$E_g = \frac{2\gamma}{M^{1/2}}, \qquad (2.7)$$

where γ is the nearest-neighbor π interaction and M is the number of six-membered rings in a cluster.[69] However, *Equation 2.7* does not account for ring distortion and lower-order carbon rings (e.g. cyclopropene and cyclobutene) prevalent in ta-C layers. Hence, this description is limited to approximating band gap values in layers with a high fraction of sp^2-hybridized carbon (> 90 %).[69]

In the absence of a simple equation relating the band gap to the sp^2-content for layers with higher sp^3-hybridized carbon content, an empirically derived correlation between the sp^2-carbon content and the optical (Tauc) gap has been proposed for determining the band gap energy:[67, 68]

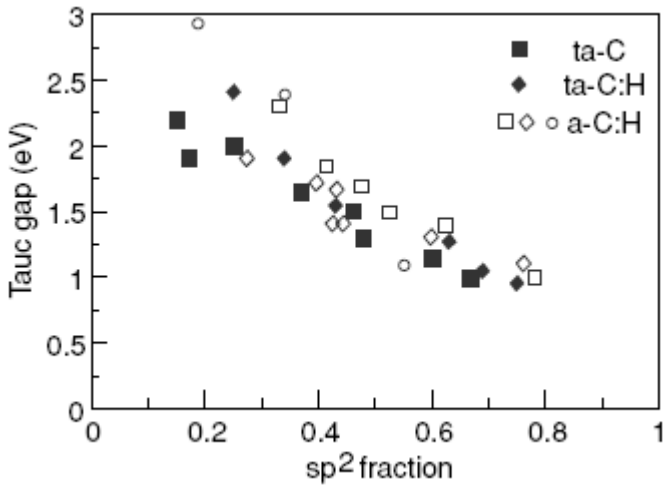

Figure 2.5: Correlation between the sp^2-hybridized carbon content and the optical gap displayed by different DLC layers (reproduced from Robertson[67]).

In addition to the π and π^* tail bands, electronic states are also introduced into the band gap by defects present in the carbon matrix. Similar to amorphous silicon, electronic defects in DLC result from trivalent sp^3-hybridized carbons (i.e. "dangling bonds") (*Figure 2.6(a)*). Additionally, since DLC also contains π electron densities, sp^2-carbon

clusters with an odd number of π electron orbitals contribute to the present defects (*Figure 2.6(b)*).

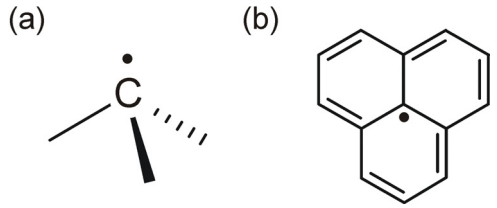

Figure 2.6: Graphic representation of electronic defects commonly encountered in DLC layers due to (a) "dangling bonds", and (b) odd π electron orbitals.

Dangling bonds in amorphous silicon are passivated by the introduction of hydrogen. Through the incorporation of small amounts of hydrogen, the band edges of DLC are sharpened and electronic states are scavenged from the band gap demonstrating a behavior similar to amorphous silicon.[70, 71] Consequently, the removal of electronic states from the band gap results in higher electrical resistivities.[72]

Doping has been proposed as a strategy for improving the electronic properties of DLC. However, a consensus regarding efficiency of the doping material, minimum concentrations required, and side-effects on the carbon network (e.g. promotion of clustering of sp^2-carbon) due to the presence of an additional element has not yet been achieved in literature.[63, 66, 73-77]

Generally, introducing low levels (~ 1 %) of nitrogen into a ta-C matrix results in a decrease in conductivity, followed by an increase at higher amounts (> 2 %). Non-doped ta-C is a slight p-type semiconductor, and the initial incorporation of nitrogen causes the Fermi level to shift towards mid-gap, thereby decreasing the conductivity. With increased nitrogen incorporation, the Fermi level continuously shifts towards the conduction band

resulting in slightly increased conductivity.[67] In addition, at high nitrogen content sp^2-hybridized carbon clustering increases, also contributing to the electrical conductivity observed.[74, 78]

2.2.4 Electrochemical characterization of conducting DLC

Cyclic voltammetry (CV) is one of the most used electroanalytical techniques for the investigation of electrochemical reactions, including monitoring of reaction pathways in organic chemistry,[79] characterization of catalysts[80], and determination of charge transfer rates at different electrode materials.[81-83] Typically, a CV experiment is performed by linearly varying the potential applied at the "working electrode" from an initial potential (E_i) to a second potential, called the switching potential (E_λ), and back to E_i. The scan rate (ν), determines the time scale of the experiment[84], and the current response is plotted against the applied potential. The potential waveform, along with the simulated CV obtained for a one-electron transfer reaction with a "fast" electron transfer kinetics are presented graphically in *Figure 2.7*:

$$O + e^- \underset{k_b}{\overset{k_f}{\rightleftharpoons}} R, \tag{2.8}$$

where *O* is the oxidized and *R* is the reduced form of the analyte, and k_f and k_b are the forward and backward rate constants, respectively.

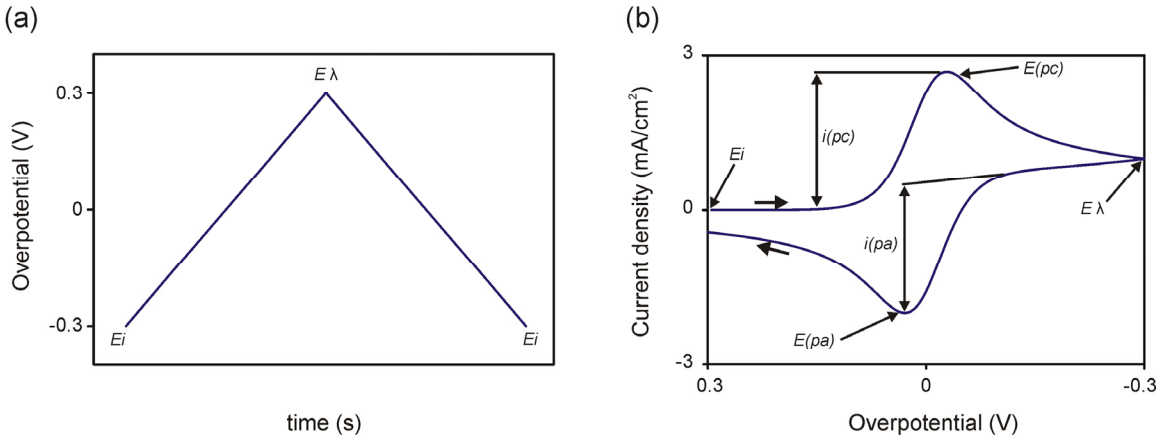

Figure 2.7: (a) Triangular waveform applied during cyclic voltammetry, and (b) cyclic voltammogram obtained from a fast one-electron transfer reaction.

The current measured with respect to the applied potential (*Figure 2.7(b)*) is based on the heterogeneous electron transfer, and the mass transport determined by diffusion processes.[85] The heterogeneous electron transfer is a function of the net reaction rate (v_{net}), and the concentration of each species at the electrode | electrolyte interface at a time t:

$$v_{net} = \left[k_f C_O(0,t) - k_b C_R(0,t)\right] nFA = i \tag{2.9}$$

Under the condition that C_O and C_R at the surface of the electrode are equal to the bulk concentrations, C_O^* and C_R^*, k_f and k_b can be expressed in terms of the standard heterogeneous rate constant, k_s:

$$k_f = k_s \exp\left(\frac{-\alpha nF}{RT}\right)\left(E - E^o\right), \tag{2.10}$$

and

$$k_b = k_s \exp\left(\frac{(1-\alpha)nF}{RT}\right)\left(E - E^o\right), \tag{2.11}$$

where α is the charge transfer coefficient, T is the Kelvin temperature, n is the number of electrons transferred in the electrode reaction, E is the applied potential and E^o is the standard potential.

By substituting k_f and k_b into *Equation 2.9*, the general equation describing the heterogeneous electron transfer is obtained:[84]

$$i = nFA\left(C_O(0,t)k_s \exp\left[\frac{-\alpha nF\left(E - E^o\right)}{RT}\right] - C_R(0,t)k_s \exp\left[\frac{(1-\alpha)nF\left(E - E^o\right)}{RT}\right]\right). \tag{2.12}$$

Equation 2.12 is valid in the presence of convection (i.e. in a stirred solution), or at low currents where the electrode surface concentrations of O and R are nearly identical to the bulk concentration (i.e. $C_O = C_O^*$ and $C_R = C_R^*$). In the absence of convection and electrostatic migration (through the addition of large amounts of supporting electrolyte), the influence of mass transport by diffusion must be taken into account. If only the reduction process in *Equation 2.8* is considered, an expanding depletion layer is formed at the electrode surface as the electrochemical reaction proceeds. The current becomes proportional to the concentration profile:

$$i = nFAD_O\left(\frac{\partial C_O(x,t)}{\partial x}\right)_{x=0} \tag{2.13}$$

The sharp rise in current shown in *Figure 2.7(b)* is related to the exponential dependence of k_f with the applied potential. However, as the reaction proceeds the concentration of O near the electrode surface decreases. Since diffusion is the only mode of mass transport, the depletion layer increases with the applied potential, and consequently, the rate of

mass transport decreases. A peak current (i_{pc} and i_{pa} in *Figure 2.7(b)*) is obtained when the rate of mass transport becomes the limiting step. The current subsequently decays due to the continuously increasing depletion layer.[85]

The k_s value can be used as a classification parameter of the electrochemical reaction. At systems with fast electron transfer rates ($k_s > 0.1$ cm/s) the measured currents depend solely on mass transport (i.e. diffusion) of the analyte to the electrode. *Equation 2.12* breaks down to the Nernst equation, as the concentrations of *O* and *R* depend only on the applied potential. Fast electrochemical reactions are termed "reversible" electrochemical reactions. Conversely, at very slow electron transfer rates ($k_s < 10^{-5}$ cm/s) the limiting step is the heterogeneous charge transfer, and these electrochemical reactions are defined as "irreversible" electrochemical reactions. Between the two extremes, "quasi-reversible" electrochemical reactions ($0.1 > k_s > 10^{-5}$) are dependent on both mass transport and the electrode kinetics.[86]

A direct measure of the reversibility is the difference between the anodic and cathodic peak potentials (ΔE_p). For a fast charge transfer (i.e. a reversible reaction), a ΔE_p of 59.1 mV/n is expected, and deviations from this value indicate a finite heterogeneous charge transfer. The peak potential separation is directly related to k_s via the kinetic parameter ψ as follows:[87]

$$\Delta E_p = f(\psi), \tag{2.14}$$

and

$$\psi = \frac{\left(\frac{D_o}{D_R}\right)^{\alpha/2} k_s}{\left(D_O \pi \frac{nF}{RT} \upsilon\right)^{1/2}} \tag{2.15}$$

Equation 2.15 can be simplified by excluding contributions from α when $D_o = D_R$. Computed values of ψ for different ΔE_ps have been tabulated by Nicholson et al.[87]

Additionally, several approaches have been developed for the determination of both k_s and α. The linear portions of Tafel plots (η vs. log | i |) have a slope equal to:

$$\frac{(1-\alpha)F}{2.303RT} \tag{2.16}$$

for the anodic branch, and

$$\frac{-\alpha F}{2.303RT} \tag{2.17}$$

for the cathodic branch.[84] However, derivation of the kinetic parameters by the Tafel method is only valid if current contributions from the reverse reaction are negligible (< 1 %), which is given when the difference between E and E^o is greater than 118 mV (i.e. irreversible reactions). If this condition is not met, mass transfer effects will influence the linear portion of the Tafel plot. Extrapolation of the linear segment yields the exchange current (i_o), which is used to determine the heterogeneous rate constant.

For quasi-reversible reactions, the current measured is related to both the forward and reverse reactions, hence both must be considered as described by Allen and Hickling:[88]

$$i = i_o \exp\left(\frac{\alpha n F \eta}{RT}\right)\left(1 - \exp\left(\frac{-nF\eta}{RT}\right)\right) \qquad (2.18)$$

By rearrangement of *Equation 2.18*, a linear plot of the overpotential (η) versus $\log\left(\frac{i}{1-\exp\left(-nF\eta/RT\right)}\right)$ is obtained, with a slope equal to $\frac{2.303RT}{\alpha nF}$.

Additionally, kinetic information can be extracted via mathematical fitting of the experimental data.[89, 90, 91]

For the determination of kinetic parameters using cyclic voltammetry, certain experimental parameters must be taken into consideration. The presence of uncompensated solution resistance can lead to erroneous results, as its effects resemble those of an electrochemical system with finite heterogeneous electron transfer kinetics (e.g. shifts in peak potentials, lower peak currents and increased peak width).[92] In order to minimize the influence on the voltammograms recorded within the experimental work of this thesis, automatic compensation via a positive feedback mechanism[93] was utilized, in addition to an optimized electrochemical cell set-up, which locates the reference electrode in close proximity (approx. 1 mm) to the working electrode.

Also, the type of potentiostat (digital or analog) affects the determined k_s and α values. Digital potentiostats perform cyclic voltammograms by changing the potential in discrete steps. Parameters like the step height (ΔE_{step}), step width (τ), and the time interval for current sampling (α') will influence the shape of a cyclic staircase voltammogram, and correspondingly, the measured kinetic parameters.[94] Osteryoung and co-workers[95]

showed that voltammograms recorded at digital and analog potentiostats are nearly identical (regardless of α'), if the following condition is fulfilled:

$$\frac{nF\Delta E_{step}}{RT} \leq 0.01 \tag{2.19}$$

The digital potentiostats used to generate the CVs in this thesis have a step height of 0.1 mV, fulfilling the requirement listed above.

2.2.5 Imaging with scanning electrochemical microscopy

For a disk-shaped microelectrode, the steady-state diffusion controlled Faradaic current measured in bulk is described by:

$$i_{T,\infty} = 4nFaC_o D\,, \tag{2.20}$$

where n is the number of electrons transferred in the reaction at the tip, F is the Faraday constant, D is the diffusion coefficient of the redox mediator, C_o is the concentration of the redox mediator in the bulk, and a is the radius of an ultramicroelectrode (UME).

Positioning of an UME near a substrate is achieved via current-distance curves ("approach curves"). When the UME is placed in close proximity of an insulator, the tip current decreases ($i_T < i_{T,\infty}$) due to the hindered hemispherical diffusion of the redox mediator ("negative feedback", *Figure 2.8(a)*). If the substrate is conducting, the mediator is regenerated at the substrate surface ($i_T > i_{T,\infty}$) resulting in an increased flux towards the tip and a concomitant increased tip current ("positive feedback", *Figure 2.8(b)*). Approach curves are usually plotted with dimensionless x- and y-values by normalizing i_T with the current measured in bulk solution ($i_{T,\infty}$), and normalizing the distance traveled (d) with the radius of the UME (a).

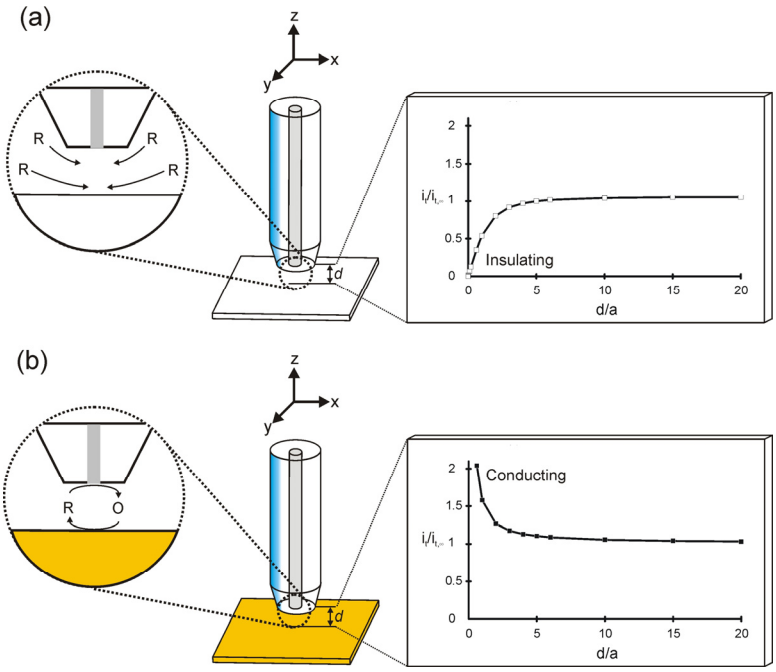

Figure 2.8: Current response measured at the ultramicroelectrode for (a) negative, and (b) positive feedback mode.

Images corresponding to the local electrochemical activity can be obtained with scanning electrochemical microscopy (SECM) by rastering the UME at constant height or constant distance across the sample surface. In principle, the measurement is based on the disturbed hemispherical diffusion of a redox species towards the UME. The presence of an electroactive site leads to increases in the Faradaic current measured at the UME due to the regeneration of the redox mediator (i.e. positive feedback). In contrast, insulating areas lead to negative feedback.

2.3 Redox polymer membranes

2.3.1 Introduction

Electroactive polymers can be classified according to the prevalent conduction mechanism. In conjugated polymers, like polyaniline and polypyrrole, electronic

conduction occurs upon rearrangement of the bond structure within the polymer backbone.[96] Conversely, in redox polymers, conduction originates from an "electron hopping" mechanism occurring between adjacent redox sites that are linked to the backbone.[97, 98] The redox sites are covalently bound to the backbone, and therefore spatially fixed (*Figure 2.9(a)*).[99-101] Ion-exchange polymers are a subgroup of redox polymers where redox sites are bound to the polymer backbone by electrostatic interactions, thereby enabling limited diffusion of the redox species through the polymer (*Figure 2.9(b)*).[102-104]

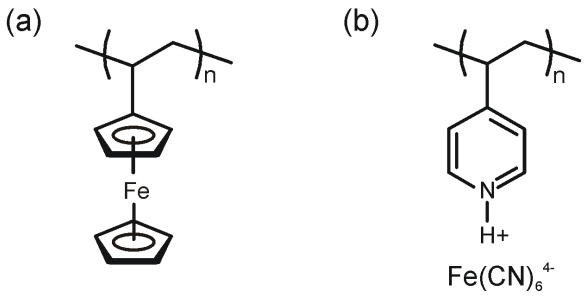

Figure 2.9: Examples of redox polymers with (a) covalently, and (b) electrostatically bonded redox sites.

The introduction of chemically modified electrodes using redox polymer coatings was initiated by their application in electrocatalysis,[101, 105] for corrosion protection[106], and for bioelectrochemistry.[107] Several procedures have been developed for the deposition of polymer coatings onto electrodes, including solvent-casting[108], electropolymerization[109], and plasma deposition.[110] Electropolymerization offers the advantage that highly cross-linked polymers with a homogeneous thickness can be deposited onto substrates with complex geometries.[111, 112]

In general, the electropolymerization process is initiated by the electrochemical generation of radical species, either by oxidation or reduction of the monomer. Subsequently, the radical monomer reacts with another radical, or with the original monomer, thereby yielding a dimer. Recombination of two radical species results in chain termination and requires re-initiation by another electronic transfer at the electrode, or by reacting with another radical species continuing propagation of the polymer chain. The exact mechanism, however, is dependent upon several parameters including the nature of the monomer, the pH, and the applied potential. The mechanism for 2-vinylpyridine (2-VP) depicted in *Figure 2.10* illustrates the initial stages of the electropolymerization process.[113] In *Chapter 5*, several spectroscopic studies were developed in order to investigate if 4-vinylpyridine (4-VP) undergoes a similar electropolymerization mechanism.

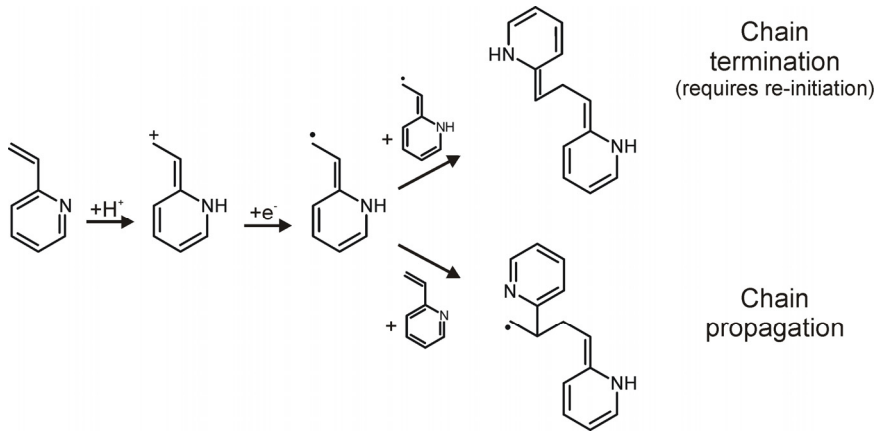

Figure 2.10: Mechanism for the electropolymerization of 2-vinylpyridine.[113]

Examples of electropolymerizable ion-exchange redox polymers include 2- VP[114], 4-VP[115], and N,N-dimethylaniline.[116]

2.3.2 Redox polymers in mid-IR spectroelectrochemistry

To date, mid-IR spectroelectrochemistry has been applied to the study of the growth mechanism and doping processes of conducting polymers (e.g. polyaniline) in both external reflectance[117-119], and ATR mode.[120-122] However, spectroscopic studies of the electropolymerization process of redox polymers, including ion incorporation (and ejection) have not yet been reported.

Furthermore, the combination of ion-exchange polymer membranes with spectroelectrochemical sensing platforms provides an additional strategy for improved selectivity, as well as increased sensitivity via enrichment of the analyte into the membrane. This concept has been successfully demonstrated using solvent-casted polymer-coated UV-Vis ATR spectroelectrochemical platforms, as introduced by Heineman and co-workers.[123-125]

Consequently, utilizing an IR-ATR element coated with an optically transparent electrode, such as conductive DLC, permits the acquisition of spectroscopic information on the electropolymerization process, in addition to monitoring the enrichment of electroactive species into the ion-exchange membrane. Hence, a main goal of this thesis was extending spectroelectrochemical sensing strategies to the mid-infrared spectral regime for the first time.

2.4 References

1. Harrick, N. J., *Internal Reflection Spectroscopy*. 1967; p 327 pp.

2. Fahrenfort, J., *Attenuated total reflection. A new principle for the production of useful infrared reflection spectra of organic compounds*, Spectrochimica Acta, **17**, 698-709, (1961).

3. Kraft, M.; Mizaikoff, B., *A mid-infrared sensor for monitoring of chlorinated hydrocarbons in the marine environment*, Int. J. Environ. Anal. Chem., **78 (3-4)**, 367-383, (2000).

4. Planinsek, O.; Planinsek, D.; Zega, A.; Breznik, M.; Srcic, S., *Surface analysis of powder binary mixtures with ATR FTIR spectroscopy*, Int. J. Pharm., **319 (1-2)**, 13-19, (2006).

5. Huber-Waelchli, P.; Guenthard, H. H., *ATR technique for ir matrix spectroscopy*, Journal of Physics E: Scientific Instruments, **9 (5)**, 409-411, (1976).

6. Ashley, K., *Solution infrared spectroelectrochemistry: a review*, Talanta, **38 (11)**, 1209-1218, (1991).

7. Flowers, P. A.; Callender, S.-A., *Variable Path Length Transmittance Cell for Ultraviolet, Visible, and Infrared Spectroscopy and Spectroelectrochemistry*, Anal. Chem., **68 (1)**, 199-202, (1996).

8. Roth, J. D.; Weaver, M. J., *Potential-difference surface infrared spectroscopy under forced hydrodynamic flow conditions: control and elimination of adsorbate solution-phase interferences*, Anal. Chem., **63 (15)**, 1603-1606, (1991).

9. Corrigan, D. S.; Weaver, M. J., *The interpretation of solution electrolyte vibrational bands in potential-difference infrared spectroscopy*, J. Electroanal. Chem. Interfac., **239 (1-2)**, 55-66, (1988).

10. Bae, I. T.; Scherson, D. A.; Yeager, E. B., *Infrared spectroscopic determination of pH changes in diffusionally decoupled thin-layer electrochemical cells*, Anal. Chem., **62 (1)**, 45-49, (1990).

11. Korzeniewski, C., *Infrared spectroscopy in electrochemistry: new methods and connections to UhV surface science*, Crit. Rev. Anal. Chem., **27 (2)**, 81-102, (1997).

12. Strojek, J. W.; Mielczarski, J.; Nowak, P., *Spectroscopic investigations of the solid-liquid interface by the ATR technique*, Adv. Colloid Interface Sci., **19 (4)**, 309-327, (1983).

13. Nakao, Y.; Yamada, H., *Enhanced infrared ATR spectra of surface layers using metal films*, J. Electron Spectrosc. Relat. Phenom., **45**, 189-196, (1987).

14. Hatta, A.; Suzuki, Y.; Wadayama, T.; Suetaka, W., *Kretschmann ATR-IR spectroscopy of investigating metal/liquid(or solid) interfaces*, Appl. Surf. Sci., **48-49**, 222-226, (1991).

15. Wadayama, T.; Momota, Y.; Hatta, A.; Suetaka, W., *Polarization modulation IR spectroscopic study of electrochemically generated species from TCNE at a gold electrode in the Kretschmann ATR geometry*, J. Electroanal. Chem. Interfac., **289 (1-2)**, 29-36, (1990).

16. Christensen, P. A.; Hamnett, A., *In-situ infrared studies of the electrode-electrolyte interface*, Compr. Chem. Kinet., **29**, 1-77, (1989).

17. Neugebauer, H.; Moser, A.; Strecha, P.; Neckel, A., *In situ FTIR spectroscopy of iron electrodes in alkaline solutions. I. Internal reflection spectroscopy*, J. Electrochem. Soc., **137 (5)**, 1472-1475, (1990).

18. Zippel, E.; Kellner, R.; Krebs, M.; Breiter, M. W., *ATR-IR studies of carbon monoxide adsorption from solutions*, J. Electroanal. Chem., **330 (1-2)**, 521-527, (1992).

19. Johnson, B. W.; Bauhofer, J.; Doblhofer, K.; Pettinger, B., *Practical considerations of the IR attenuated-total-reflection (IR-ATR) technique for electrochemical investigations*, Electrochim. Acta, **37 (12)**, 2321-2329, (1992).

20. Pham, M. C.; Adami, F.; Dubois, J. E., *An in situ multiple internal reflection Fourier transform infrared spectroscopy investigation of the electropolymerization mechanism of substituted phenols on iron electrodes*, J. Electrochem. Soc., **134 (9)**, 2166-2169, (1987).

21. Pham Minh, C.; Moslih, J.; Simon, M.; Lacaze, P. C., *In-situ IR study by MIRFTIRS of adsorption and oxidation of methanol on sputtered platinum electrodes in sulfuric acid solution*, J. Electroanal. Chem. Interfac., **282 (1-2)**, 287-294, (1990).

22. Neugebauer, H.; Nauer, G.; Brinda-Konopik, N.; Gidaly, G., *The in situ determination of oxidation products on iron electrodes in alkaline electrolytes using multiple internal reflection Fourier transform infrared spectroscopy*, J. Electroanal. Chem. Interfac., **122**, 381-385, (1981).

23. Buskuehl, M.; Korte, E.-H., *Infrared-optical properties of vapor-deposited metal films*, Anal. Bioanal. Chem., **374 (4)**, 672-675, (2002).

24. Kamata, T.; Kato, A.; Umemura, J.; Takenaka, T., *Intensity enhancement of infrared attenuated total reflection spectra of stearic acid Langmuir-Blodgett monolayers with evaporated silver island films*, Langmuir, **3 (6)**, 1150-1154, (1987).

25. Maaroof, A. I.; Evans, B. L., *Onset of electrical conduction in Pt and Ni films*, J. Appl. Phys., **76 (2)**, 1047-1054, (1994).

26. Zippel, E.; Kellner, R.; Breiter, M. W., *Instability of sputtered platinum films on germanium reflection elements in aqueous solutions*, J. Electroanal. Chem. Interfac., **289 (1-2)**, 297-298, (1990).

27. Ping, Z.; Nauer, G. E., *In situ FTIR-ATR spectroscopic investigations on the redox behavior of poly(thienylpyrrole) thin film electrodes in non-aqueous solutions*, Synth. Met., **84 (1-3)**, 843-844, (1997).

28. Zimmermann, A.; Dunsch, L., *Investigation of the electropolymerization of aniline by the in situ techniques of attenuated total reflection (ATR) and external reflection (IRRAS)*, J. Mol. Struct., **410-411**, 165-171, (1997).

29. Mark, H. B., Jr.; Pons, B. S., *In situ spectrophotometric method for observing the infrared spectra of species at the electrode surface during electrolysis*, Anal. Chem., **38 (1)**, 119-121, (1966).

30. Reed, A. H.; Yeager, E., *Infrared internal reflection studies of the germanium/electrolyte interface*, Electrochim. Acta, **15 (8)**, 1345-1354, (1970).

31. Tallant, D. R.; Evans, D. H., *Application of infrared internal reflection spectrometry to studies of the electrochemical reduction of carbonyl compounds*, Anal. Chem., **41 (6)**, 835-838, (1969).

32. Higashiyama, T.; Takenaka, T., *Infrared attenuated total reflection spectra of adsorbed layers at the interface between a germanium electrode and an aqueous solution of sodium laurate*, J. Phys. Chem., **78 (9)**, 941-947, (1974).

33. Aisenberg, S.; Chabot, R., *Ion-beam deposition of thin films of diamondlike carbon*, J. Appl. Phys., **42 (7)**, 2953-2958, (1971).

34. Robertson, J., *Properties of diamond-like carbon*, Surf. Coat. Technol., **50 (3)**, 185-203, (1992).

35. Voevodin, A. A.; Zabinski, J. S., *Superhard, functionally gradient, nanolayered and nanocomposite diamond-like carbon coatings for wear protection*, Diamond Relat. Mater., **7 (2-5)**, 463-467, (1998).

36. Wei, Q.; Narayan, J., *Superhard diamondlike carbon: preparation, theory, and properties*, Int. Mater. Rev., **45 (4)**, 133-164, (2000).

37. Voevodin, A. A.; Donley, M. S., *Preparation of amorphous diamond-like carbon by pulsed laser deposition: a critical review*, Surf. Coat. Technol., **82 (3)**, 199-213, (1996).

38. Narayan, R. J., *Laser processing of diamondlike carbon thin films for medical prostheses*, Int. Mater. Rev., **51 (2)**, 127-143, (2006).

39. Robertson, J., *Defects in diamond-like carbon*, Phys. Status Solidi A, **186 (2)**, 177-185, (2001).

40. Ronkainen, H.; Varjus, S.; Koskinen, J.; Holmberg, K., *Differentiating the tribological performance of hydrogenated and hydrogen-free DLC coatings*, Wear, **249 (3-4)**, 260-266, (2001).

41. Pharr, G. M.; Callahan, D. L.; McAdams, S. D.; Tsui, T. Y.; Anders, S.; Anders, A.; Ager, J. W., III; Brown, I. G.; Bhatia, C. S.; et al., *Hardness, elastic modulus, and structure of very hard carbon films produced by cathodic-arc deposition with substrate pulse biasing*, Appl. Phys. Lett., **68 (6)**, 779-781, (1996).

42. Lenardi, C.; Piseri, P.; Briois, V.; Bottani, C. E.; Li Bassi, A.; Milani, P., *Near-edge x-ray absorption fine structure and Raman characterization of amorphous and nanostructured carbon films*, J. Appl. Phys., **85 (10)**, 7159-7167, (1999).

43. Alam, T. M.; Friedmann, T. A.; Schultz, P. A.; Sebastiani, D., *Low temperature annealing in tetrahedral amorphous carbon thin films observed by 13C NMR spectroscopy*, Phys. Rev. B: Condens. Matter Mater. Phys., **67 (24)**, 245309/245301-245309/245311, (2003).

44. Samano, E. C.; Soto, G.; Olivas, A.; Cota, L., *DLC thin films characterized by AES, XPS and EELS*, Appl. Surf. Sci., **202 (1-2)**, 1-7, (2002).

45. Haerle, R.; Riedo, E.; Pasquarello, A.; Baldereschi, A., *sp2/sp3 Hybridization ratio in amorphous carbon from C 1s core-level shifts: X-ray photoelectron spectroscopy and first-principles calculation*, Phys. Rev. B: Condens. Matter Mater. Phys., **65 (4)**, 045101/045101-045101/045109, (2002).

46. Scaglione, S.; Giorgi, R.; Lascovich, J. C.; Ottaviani, G., *Study of the sp2-to-sp3 ratio of dual-ion-beam sputtered hydrogenated amorphous carbon films*, Surf. Coat. Technol., **47 (1-3)**, 287-291, (1991).

47. Gilkes, K. W. R.; Sands, H. S.; Batchelder, D. N.; Robertson, J.; Milne, W. I., *Direct observation of sp3 bonding in tetrahedral amorphous carbon using ultraviolet Raman spectroscopy*, Appl. Phys. Lett., **70 (15)**, 1980-1982, (1997).

48. Hauert, R., *An overview on the tribological behavior of diamond-like carbon in technical and medical applications*, Tribology International, **37 (11-12)**, 991-1003, (2004).

49. Wei, Q.; Sharma, A. K.; Narayan, R. J.; Ravindra, N. M.; Oktyabrsky, S.; Sankar, J.; Muth, J. F.; Kolbas, R. M.; Narayan, J. In *Microstructure and IR range optical properties of pure DLC and DLC containing dopants prepared by pulsed laser deposition*, Materials Research Society Symposium Proceedings, 1998; pp 331-336.

50. Janotta, M.; Rudolph, D.; Kueng, A.; Kranz, C.; Voraberger, H.-S.; Waldhauser, W.; Mizaikoff, B., *Analysis of Corrosion Processes at the Surface of Diamond-Like Carbon Protected Zinc Selenide Waveguides*, Langmuir, **20 (20)**, 8634-8640, (2004).

51. Janotta, M.; Vogt, F.; Voraberger, H.-S.; Waldhauser, W.; Lackner Jurgen, M.; Stotter, C.; Beutl, M.; Mizaikoff, B., *Direct analysis of oxidizing agents in aqueous solution with attenuated total reflectance mid-infrared spectroscopy and diamond-like carbon protected waveguides*, Anal. Chem., **76 (2)**, 384-391, (2004).

52. Yoo, K.; Miller, B.; Kalish, R.; Shi, X., *Electrodes of nitrogen-incorporated tetrahedral amorphous carbon. A novel thin-film electrocatalytic material with diamond-like stability*, Electrochem. Solid-State Lett., **2 (5)**, 233-235, (1999).

53. Krotova, M. D.; Evstefeeva, Y. U. E.; Pleskov, Y. U. V.; Elkin, V. V.; Baranov, A. M., *Diamond-like carbon electrodes: the impedance spectroscopy and kinetics of redox reactions*, Russ. J. Electrochem., **34 (9)**, 934-939, (1998).

54. Lagrini, A.; Deslouis, C.; Cachet, H.; Benlahsen, M.; Charvet, S., *Elaboration and electrochemical characterization of nitrogenated amorphous carbon films*, Electrochem. Commun., **6 (3)**, 245-248, (2004).

55. Kumar, S.; Sarangi, D.; Dixit, P. N.; Panwar, O. S.; Bhattacharyya, R., *Diamond-like carbon films with extremely low stress*, Thin Solid Films, **346 (1,2)**, 130-137, (1999).

56. Onoprienko, A. A.; Artamonov, V. V.; Yanchuk, I. B., *Effect of magnetron discharge power on the resistivity and microstructure of carbon films*, Surf. Coat. Technol., **200 (14-15)**, 4174-4178, (2006).

57. Lazar, G., *Influence of the substrate-electrode applied bias voltage on the properties of sputtered a-C:H thin films*, J. Phys.: Condens. Matter, **13 (13)**, 3011-3021, (2001).

58. Fallon, P. J.; Veerasamy, V. S.; Davis, C. A.; Robertson, J.; Amaratunga, G. A. J.; Milne, W. I.; Koskinen, J., *Properties of filtered-ion-beam-deposited diamondlike carbon as a function of ion energy*, Phys. Rev. B: Condens. Matter Mater. Phys., **48 (7)**, 4777-4782, (1993).

59. Haverkamp, J.; Mayo, R. M.; Bourham, M. A.; Narayan, J.; Jin, C.; Duscher, G., *Plasma plume characteristics and properties of pulsed-laser-deposited diamond-like carbon films*, J. Appl. Phys., **93 (6)**, 3627-3634, (2003).

60. Voevodin, A. A.; Laube, S. J. P.; Walck, S. D.; Solomon, J. S.; Donley, M. S.; Zabinski, J. S., *Pulsed laser deposition of diamond-like amorphous carbon films from graphite and polycarbonate targets*, J. Appl. Phys., **78 (6)**, 4123-4130, (1995).

61. Peeler, D. T.; Murray, P. T., *Dynamics of amorphous carbon film growth by pulsed laser deposition: kinetic energy of the incident particles*, Diamond Relat. Mater., **3 (8)**, 1124-1127, (1994).

62. Germain, C.; Girault, C.; Aubreton, J.; Catherinot, A.; Bec, S.; Tonck, A., *Photoablation of a graphite target by a KrF laser beam. Realization of hard carbon thin films*, Diamond Relat. Mater., **4 (4)**, 309-313, (1995).

63. Arena, C.; Kleinsorge, B.; Robertson, J.; Milne, W. I.; Welland, M. E., *Electronic and topographic structure of ta-C, ta-C:N and ta-C:B investigated by scanning tunnelling microscopy*, Diamond Relat. Mater., **8 (2-5)**, 435-439, (1999).

64. Voevodin, A. A.; Jones, J. G.; Back, T. C.; Zabinski, J. S.; Strel'nitzki, V. E.; Aksenov, I. I., *Comparative study of wear-resistant DLC and fullerene-like CNx coatings produced by pulsed laser and filtered cathodic arc depositions*, Surf. Coat. Technol., **197 (1)**, 116-125, (2005).

65. Narayan, R. J., *Pulsed laser deposition of functionally gradient diamondlike carbon-metal nanocomposites*, Diamond Relat. Mater., **14 (8)**, 1319-1330, (2005).

66. Rusop, M.; Soga, T.; Jimbo, T.; Umeno, M.; Sharon, M., *Electronic Doping of Amorphous Carbon Thin Films*, Surf. Rev. Lett., **12 (4)**, 579-586, (2005).

67. Robertson, J., *Electronic and atomic structure of diamond-like carbon*, Semicond. Sci. Technol., **18 (3)**, S12-S19, (2003).

68. Robertson, J., *Electronic structure of diamond-like carbon*, Diamond Relat. Mater., **6 (2-4)**, 212-218, (1997).

69. Robertson, J.; O'Reilly, E. P., *Electronic and atomic structure of amorphous carbon*, Phys. Rev. B: Condens. Matter Mater. Phys., **35 (6)**, 2946-2957, (1987).

70. Bredas, J. L.; Street, G. B., *Electronic properties of amorphous carbon films*, J. Phys. C: Solid State Phys., **18 (21)**, L651-L655, (1985).

71. Kleinsorge, B.; Rodil, S. E.; Adamopoulos, G.; Robertson, J.; Grambole, D.; Fukarek, W., *Hydrogen and disorder in diamond-like carbon*, Diamond Relat. Mater., **10 (3-7)**, 965-969, (2001).

72. Veerasamy, V. S.; Amaratunga, G. A. J.; Davis, C. A.; Milne, W. I.; Hewitt, P., *Electronic density of states in highly tetrahedral amorphous carbon*, Solid-State Electron., **37 (2)**, 319-326, (1994).

73. Silva, S. R. P., *Properties of Amorphous Carbon*. INSPEC: London, 2003; Vol. 29, p 367.

74. Kleinsorge, B.; Ferrari, A. C.; Robertson, J.; Milne, W. I., *Influence of nitrogen and temperature on the deposition of tetrahedrally bonded amorphous carbon*, J. Appl. Phys., **88 (2)**, 1149-1157, (2000).

75. Davis, C. A.; McKenzie, D. R.; Yin, Y.; Kravtchinskaia, E.; Amaratunga, G. A. J.; Veerasamy, V. S., *Substitutional nitrogen doping of tetrahedral amorphous carbon*, Philosophical Magazine B: Physics of Condensed Matter: Statistical Mechanics, Electronic, Optical and Magnetic Properties, **69 (6)**, 1133-1140, (1994).

76. Chhowalla, M.; Yin, Y.; Amaratunga, G. A. J.; McKenzie, D. R.; Frauenheim, T., *Boronated tetrahedral amorphous carbon (ta-C:B)*, Diamond Relat. Mater., **6 (2-4)**, 207-211, (1997).

77. Ma, Z. Q.; Liu, B. X., *Boron-doped diamond-like amorphous carbon as photovoltaic films in solar cell*, Sol. Energy Mater. Sol. Cells, **69 (4)**, 339-344, (2001).

78. Ferrari, A. C.; Rodil, S. E.; Robertson, J., *Interpretation of infrared and Raman spectra of amorphous carbon nitrides*, Phys. Rev. B: Condens. Matter Mater. Phys., **67 (15)**, 155306/155301-155306/155320, (2003).

79. Bobbitt, J. M.; Willis, J. P., *Electrochemistry of natural products. 7. Oxidative decarboxylation of some tetrahydro-b-carbolinecarboxylic acids*, J. Org. Chem., **45 (10)**, 1978-1984, (1980).

80. Tokarev, A. V.; Kustov, L. M.; Ivaska, A.; Murzin, D. Y., *Cyclic voltammetry as a tool for characterization of supported VIII group metal catalysts*, Appl. Catal., A, **309 (1)**, 52-61, (2006).

81. Chen, P.; Fryling, M. A.; McCreery, R. L., *Electron Transfer Kinetics at Modified Carbon Electrode Surfaces: The Role of Specific Surface Sites*, Anal. Chem., **67 (18)**, 3115-3122, (1995).

82. Pillai, K. C.; Thangamuthu, R.; Ilangovan, G., *Behavior of cathodically pretreated platinum on Fe(CN)63- electroreduction in KNO3: dependence on pretreatment*, Electroanalysis, **7 (12)**, 1182-1188, (1995).

83. Granger, M. C.; Witek, M.; Xu, J.; Wang, J.; Hupert, M.; Hanks, A.; Koppang, M. D.; Butler, J. E.; Lucazeau, G.; Mermoux, M.; Strojek, J. W.; Swain, G. M., *Standard Electrochemical Behavior of High-Quality, Boron-Doped Polycrystalline Diamond Thin-Film Electrodes*, Anal. Chem., **72 (16)**, 3793-3804, (2000).

84. Bard, A. J.; Faulkner, L. R., *Electrochemical Methods: Fundamentals and Application*. 2nd ed.; John Wiley & Sons, Inc.: New York, 2001.

85. Mabbott, G. A., *An introduction to cyclic voltammetry*, J. Chem. Educ., **60 (9)**, 697-702, (1983).

86. Heinze, J., *Cyclic voltammetry - the \"spectroscopy\" of the electrochemist*, Angew. Chem., **96 (11)**, 823-840, (1984).

87. Nicholson, R. S., *Theory and application of cyclic voltammetry for measurement of electrode reaction kinetics*, Anal. Chem., **37 (11)**, 1351-1355, (1965).

88. Allen, P. L.; Hickling, A., *Electrochemistry of sulfur. I. Overpotential in the discharge of the sulfide ion*, Transactions of the Faraday Society, **53**, 1626-1635, (1957).

89. Bioanalytical Systems, I. http://www.bioanalytical.com/products/ec/digisim/ (October 15, 2006).

90. Rudolph, M. http://www.digielch.de (October 15, 2006).

91. Nervi, C. http://lem.ch.unito.it/chemistry/esp_manual.html (October 15, 2006).

92. Saveant, J. M.; Imbeaux, J. C., *Linear sweep voltammetry effect of uncompensated cell resistance and double layer charging on polarization curves*, J. Electroanal. Chem. Interfac., **28 (2)**, 327-340, (1970).

93. He, P.; Faulkner, L. R., *Intelligent, automatic compensation of solution resistance*, Anal. Chem., **58 (3)**, 517-523, (1986).

94. Seralathan, M.; Osteryoung, R. A.; Osteryoung, J. G., *General equivalence of linear scan and staircase voltammetry*, J. Electroanal. Chem. Interfac., **222 (1-2)**, 69-100, (1987).

95. Seralathan, M.; Osteryoung, R.; Osteryoung, J., *Comparison of linear sweep and staircase voltammetries using Walsh series*, J. Electroanal. Chem. Interfac., **214 (1-2)**, 141-156, (1986).

96. Scrosati, B.; Editor, *Applications of Electroactive Polymers*. 1993; p 354 pp.

97. Kaufman, F. B.; Engler, E. M., *Solid-state spectroelectrochemistry of crosslinked donor bound polymer films*, J. Am. Chem. Soc., **101 (3)**, 547-549, (1979).

98. Kaufman, F. B.; Schroeder, A. H.; Engler, E. M.; Kramer, S. R.; Chambers, J. Q., *Ion and electron transport in stable, electroactive tetrathiafulvalene polymer coated electrodes*, J. Am. Chem. Soc., **102 (2)**, 483-488, (1980).

99. Tchepournaya, I.; Vasilieva, S.; Logvinov, S.; Timonov, A.; Amadelli, R.; Bartak, D., *Electrochemical Synthesis and Characterization of Redox Polymer Nanostructures*, Langmuir, **19 (21)**, 9005-9012, (2003).

100. Pickup, P. G., *Conjugated metallopolymers. Redox polymers with interacting metal based redox sites*, J. Mater. Chem., **9 (8)**, 1641-1653, (1999).

101. Sliwa, W., *Osmium, iridium and platinum pyridine complexes*, Transition Met. Chem. (London), **20 (1)**, 1-12, (1995).

102. Oh, S. M.; Faulkner, L. R., *Electron transport dynamics in partially quaternized poly(4-vinylpyridine) thin films containing ferri/ferrocyanide*, J. Electroanal. Chem. Interfac., **269 (1)**, 77-97, (1989).

103. Geno, P. W.; Ravichandran, K.; Baldwin, R. P., *Chemically modified carbon paste electrodes. Part IV. Electrostatic binding and electrocatalysis at poly(4-vinylpyridine)-containing electrodes*, J. Electroanal. Chem. Interfac., **183 (1-2)**, 155-166, (1985).

104. Harak, D. W.; Mottola, H. A., *Electrostatically-immobilized hexacyanoferrate ions as redox mediators in biochemical sensing: controlled release and cyclic voltammetric behavior*, Biosens. Bioelectron., **6 (7)**, 589-594, (1991).

105. Kost, K. M.; Bartak, D. E.; Kazee, B.; Kuwana, T., *Electrodeposition of palladium, iridium, ruthenium, and platinum in poly(4-vinylpyridine) films for electrocatalysis*, Anal. Chem., **62 (2)**, 151-157, (1990).

106. Sekine, I.; Kohara, K.; Sugiyama, T.; Yuasa, M., *Syntheses of polymerized films on mild steels by electrooxidation and electroreduction and their corrosion resistance*, J. Electrochem. Soc., **139 (11)**, 3090-3097, (1992).

107. Ryder, K. S.; Morris, D. G.; Cooper, J. M., *Tailored Polymers To Probe the Nature of the Bioelectrochemical Interface*, Langmuir, **12 (23)**, 5681-5688, (1996).

108. Oyama, N.; Anson, F. C., *Electrostatic binding of metal complexes to electrode surfaces coated with highly charged polymeric films*, J. Electrochem. Soc., **127 (1)**, 249-250, (1980).

109. Ling, X.; Pritzker, M. D.; Burns, C. M.; Byerley, J. J., *Effects of reaction conditions on the formation of poly(2-vinylpyridine) coatings by electropolymerization*, J. Coat. Tech., **72 (908)**, 71-80, (2000).

110. Nowak, R.; Schultz, F. A.; Umana, M.; Abruna, H.; Murray, R. W., *Chemically modified electrodes. Part XIV. Attachment of reagents to oxide-free glassy carbon surfaces. Electroactive RF polymer films on carbon and platinum electrodes*, J. Electroanal. Chem. Interfac., **94 (3)**, 219-225, (1978).

111. Finklea, H. O.; Vithanage, R. S., *Non-electroactive electrode coatings formed by electrochemical polymerization*, J. Electroanal. Chem. Interfac., **161 (2)**, 283-294, (1984).

112. Teng, F. S.; Mahalingam, R.; Subramanian, R. V.; Raff, R. A. V., *Polymer film coatings on metal electrodes through electroinitiated polymerization and their evaluation*, J. Electrochem. Soc., **124 (7)**, 995-1006, (1977).

113. Ling, X.; Pritzker, M. D.; Burns, C. M.; Byerley, J. J., *A Mechanism for Electropolymerization of 2-Vinylpyridine Coatings on Metal Surfaces*, Macromolecules, **31 (26)**, 9134-9140, (1998).

114. Tantavichet, N.; Pritzker, M. D.; Burns, C. M., *Electropolymerized poly(2-vinylpyridine) coatings as ion-exchange polymer modified electrodes*, J. Appl. Electrochem., **31 (3)**, 281-291, (2001).

115. Lebrun, C.; Deniau, G.; Viel, P.; Lecayon, G., *Electrosynthesis of poly(4-vinylpyridine) films on metallic surfaces under anodic and cathodic polarizations: structure and properties of the organic coatings*, Surf. Coat. Technol., **100-101 (1-3)**, 474-479, (1998).

116. Roy, P. R.; Saha, M. S.; Okajima, T.; Ohsaka, T., *Electrocatalytic oxidation of ascorbic acid by [Fe(CN)6]3-/4- redox couple electrostatically trapped in*

cationic N,N-dimethylaniline polymer film electropolymerized on diamond electrode, Electrochim. Acta, **51 (21)**, 4447-4454, (2006).

117. Seeger, D.; Kowalchyk, W.; Korzeniewski, C., *Investigation of polymer-dopant interactions in polyaniline-modified electrodes: in situ analysis by FTIR spectroscopy*, Langmuir, **6 (10)**, 1527-1534, (1990).

118. Jones, C. L.; Higgins, S. J.; Christensen, P. A., *Some in situ reflectance Fourier transform infrared studies of electrochemically prepared polybenzo[c]thiophene and poly-5-fluorobenzo[c]thiophene films*, J. Mater. Chem., **12 (3)**, 758-764, (2002).

119. Liu, M.; Ye, M.; Yang, Q.; Zhang, Y.; Xie, Q.; Yao, S., *A new method for characterizing the growth and properties of polyaniline and poly(aniline-co-o-aminophenol) films with the combination of EQCM and in situ FTIR spectroelectrochemisty*, Electrochim. Acta, **52 (1)**, 342-352, (2006).

120. Zimmermann, A.; Kunzelmann, U.; Dunsch, L., *Initial states in the electropolymerization of aniline and p-aminodiphenylamine as studied by in situ FT-IR and UV-Vis spectroelectrochemistry*, Synth. Met., **93 (1)**, 17-25, (1998).

121. Neugebauer, H.; Kvarnstrom, C.; Cravino, A.; Yohannes, T.; Sariciftci, N. S., *Photoexcited spectroscopy and in situ electrochemical spectroscopy in conjugated polymers: a comparative study*, Synth. Met., **116 (1-3)**, 115-121, (2001).

122. Yohannes, T.; Neugebauer, H.; Farinola, G. M.; Winder, C.; Babudri, F.; Cardone, A.; Naso, F.; Sariciftci, N. S., *Vibrational spectroscopic study of a push-pull substituted fluorinated poly(p-phenylenevinylene) copolymer*, Synth. Met., **152 (1-3)**, 149-152, (2005).

123. Maghasi, A. T.; Conklin, S. D.; Shtoyko, T.; Piruska, A.; Richardson, J. N.; Seliskar, C. J.; Heineman, W. R., *Spectroelectrochemical Sensing Based on Attenuated Total Internal Reflectance Stripping Voltammetry. 2. Determination of Mercury and Lead*, Anal. Chem., **76 (5)**, 1458-1465, (2004).

124. Shi, Y.; Slaterbeck, A. F.; Seliskar, C. J.; Heineman, W. R., *Spectroelectrochemical Sensing Based on Multimode Selectivity Simultaneously Achievable in a Single Device. 1. Demonstration of Concept with Ferricyanide*, Anal. Chem., **69 (18)**, 3679-3686, (1997).

125. Stegemiller Michael, L.; Heineman William, R.; Seliskar Carl, J.; Ridgway Thomas, H.; Bryan Samuel, A.; Hubler, T.; Sell Richard, L., *Spectroelectrochemical sensing based on multimode selectivity simultaneously achievable in a single device. 11. Design and evaluation of a small portable sensor for the determination of ferrocyanide in Hanford waste samples*, Environmental science & technology, **37 (1)**, 123-130, (2003).

3 CHARACTERIZATION OF NITROGEN-DOPED DIAMONDLIKE CARBON MATERIALS

The physical, spectroscopic, and electrochemical properties of nitrogen-doped diamondlike carbon (DLC) electrodes will be discussed in this chapter. Where applicable, fundamental information on the analytical techniques used to characterize DLC layers will also be addressed. Furthermore, the influence of cathodic pretreatment in H_2SO_4 of N-DLC electrodes will be discussed. Finally, the application of these electrode materials deposited as thin films onto mid-IR waveguides for multi-reflection ATR spectroelectrochemistry will be described.

3.1 Motivation

Spectroelectrochemistry permits monitoring of changes of IR absorption features while applying a potential. To date, this type of analytical platform has largely been restricted to the ultraviolet (UV) and visible (Vis) wavelengths, due to the availability of optically transparent electrodes, such as indium-tin oxide.[1] In contrast to the UV-Vis, which is restricted to monitoring electronic transitions, the mid-IR region permits the excitation of fundamental vibrational and rotational modes associated with molecular bonds. This technique is of particular interest, as it provides information on the composition of the electrochemical double layer, on the molecular structure of species adsorbed at the electrode surface, and for monitoring molecular bonding rearrangement during application of a potential.[2, 3]

The experimental limitations of transmission[4] and external reflectance[5] IR spectroelectrochemistry discussed in *Chapters 1* and *2* of this thesis render multi-reflection ATR evanescent field spectroscopy the most suitable configuration for spectroelectrochemical analysis. However, the absence of sufficiently transparent electrodes has so far limited the more widespread adoption of the ATR configuration.[5]

The mid-IR transparency of diamondlike carbon (DLC) coatings has recently been utilized by our research group for evanescent field absorption analysis in strongly oxidizing aqueous matrices.[6, 7] Consequently, this thesis focuses on the extended applicability of this concept by the development of mid-IR transparent doped DLC layers, which are sufficiently conductive for multi-reflection spectroelectrochemical analysis.

3.1.1 Nitrogen-doped diamondlike carbon

The electrochemical properties of non-doped DLC electrodes were previously reported.[8-11] The electrical conductivity associated with non-doped layers originates from the large fraction of sp^2-hybridized carbon (> 60 %). However, highly graphitic layers are softer, less mechanically stable, and more prone to chemical degradation compared to insulating layers containing less sp^2-carbon. Introducing a dopant into the DLC matrix results in a layer with a high fraction of sp^3-hybridized carbon, which provides sufficient electrical conductivity for electrochemical applications at yet superior mechanical and chemical properties.

Several authors have described the use of doped DLC as thin film electrode materials. Initial reports by Miller and co-workers[12, 13] demonstrated that tetrahedral amorphous carbon (ta-C) layers doped with ~ 10 % nitrogen display electrochemical properties

similar to those of highly doped boron doped diamond (BDD). Zeng et al.[14, 15] and Lagrini et al.[16, 17] independently evaluated the electrochemical properties of hydrogen-free N-DLC. In their contributions, the $Fe(CN)_6^{4-/3-}$ redox couple exhibited a peak potential separation (ΔE_p) < 80 mV (ν = 0.1 V/s) for nitrogen concentrations ranging from 5 to 12 %.

Pleskov and co-workers developed nitrogen-doped hydrogenated DLC layers by adjusting the gas composition during deposition.[18, 19] In their studies, peak separations (ΔE_p) greater than 600 mV (ν = 0.05 V/s) for $Fe(CN)_6^{4-/3-}$ couple were observed, revealing a hindered heterogeneous electron transfer rate. Similar results with hydrogenated N-DLC layers were obtained by Cachet and co-workers reporting ΔE_p > 400 mV (ν = 0.05 V/s) for $Fe(CN)_6^{4-/3-}$.[20, 21]

Hydrogenated layers consistently display reduced heterogeneous electron transfer constants compared to hydrogen-free DLC, despite containing similar nitrogen concentrations. As discussed in *Section 2.2.2*, the addition of hydrogen during the deposition procedure results in the passivation of defect sites. Since defects introduce electronic states in the band gap, the removal of these states reduces the electrical conductivity, and consequently increases the peak separation (ΔE_p). Hence, the work presented in this thesis focuses on hydrogen-free doped DLC layers.

Furthermore, Janotta et al. have recently demonstrated that DLC thin films (30 – 200 nm) deposited onto ZnSe attenuated total reflectance (ATR) waveguides are transparent in the mid-infrared range (2 – 20 μm).[6, 7] These promising results obtained with DLC-coated ZnSe ATR waveguides have led to the work presented in this chapter with the goal of

combining the electrochemical and optical properties of DLC thin films for establishing an electrode material suitable for multi-reflection IR-ATR spectroelectrochemistry.

3.2 Experimental

3.2.1 Pulsed laser deposition system

The DLC layers discussed in this chapter were developed in collaboration with the Laser Center Leoben (Leoben, Austria), a division of Joanneum Research. The DLC layers were deposited in an industrial scale stainless steel chamber, provided by Joanneum Research which has been described in detail elsewhere.[22] The chamber was evacuated to a base pressure of ~ 4×10^{-5} Torr, and then brought to a working pressure of ~ 5×10^{-3} Torr for the deposition process. The composition of the processing gas (i.e. argon-to-nitrogen ratio) was varied according to the targeted nitrogen content (*Table 3.2*). The total gas flow rate was kept at 30 sccm. All substrates were cleaned by sequential sonication in acetone and ethanol. Prior to DLC deposition, the substrates were treated by in-situ argon ion etching with an Ion Tech/VEECO gun (Fort Collins, CO). DLC deposition was achieved by ablation of a high purity graphite target (99.9 %, GfE, Gesellschaft für Elektrometallurgie, Nürnberg, Germany) with a 1064 nm Nd:YAG laser from Continuum (Santa Clara, CA) operating at a repetition rate of 50 Hz with a pulse duration of 10 ns. The output of ~ 500 mJ and a spot size of ~ 0.02 cm^2 provided an energy density of ~ 25 J/cm^2. The distance from the target to the substrate was maintained at 12 cm. The DLC thin films were deposited onto n-type doped silicon substrates from Nova Electronics (Carrollton, TX, As-doped, < 0.01 Ω/cm), which were backside coated with gold. The deposition time for each DLC layer was 5 min resulting in the film thicknesses summarized in *Table 3.1*:

Table 3.1: Measured thicknesses of N-DLC layers determined by stylus profilometry.

Sample	Nitrogen gas concentration in chamber	Thickness (nm) (n = 6)
Pure DLC	0 % (pure Ar)	26 ± 8
N #1	17 %	21 ± 6
N #2	25 %	43 ± 11
N #3	33 %	41 ± 10

3.2.2 Physical characterization

The characterization of N-DLC layers was performed with several analytical techniques in an effort to correlate their physical properties to their electrochemical behavior.

Film thickness measurements were performed using a Dektak^3 ST stylus profilometer (Veeco/Sloan Technologies, Santa Barbara, CA).

X-ray photoelectron spectroscopy (XPS) data were acquired using a SSX-100 ESCA spectrometer (Surface Science Labs, Mountain View, CA) equipped with a small spot monochromatic Al Kα source (1486.6 eV). General survey spectra (0 to 1100 eV, 1 scan at 1 eV steps, 800 μm spot size, 150 eV pass energy) were recorded to verify surface constituents. High resolution spectra (10 scans at 0.1 eV steps, 400 μm spot size, 50 eV pass energy) were obtained for the carbon and nitrogen 1s peaks. Deconvolution of the carbon 1s peak was performed using the peak fitting functions of the Analysis 2000 software (Service Physics Inc., Bend, OR).

Infrared spectra were recorded in transmission mode at an Equinox 55 FT-IR spectrometer (Bruker Optics, Billerica, MA) equipped with a broadband liquid nitrogen-cooled mercury-cadmium-telluride (MCT) detector (Infrared Associates, Stuart, FL).

Spectra were recorded at 4 cm^{-1} resolution, and a total of 100 scans were averaged for each collected spectrum. N-DLC films were additionally deposited onto 5.0 cm x 2.0 cm x 2.0 mm trapezoidal attenuated total reflectance ZnSe waveguides. The coupling facets of the waveguides were masked to prevent coating. Deposition parameters for the N-DLC coating were identical to those of layer N #2 in *Table 3.2*.

Raman spectra were acquired with an ISA Jobin Yvon LabRAM (Villeneuve d'Ascq, France) spectrometer using a frequency doubled Nd:YAG laser operating at $\lambda = 532$ nm. The spot size probed was approx. 6 μm.

3.2.3 Electrochemical characterization

The electrochemical characterization of N-DLC layers was performed in a custom-made three-electrode Teflon cell (*Figure 3.1*) using a potentiostat (660A CH Instruments, Austin, TX). A 3 M KCl Ag|AgCl reference electrode (+210 mV vs. SHE) was used for the redox mediator studies, and a saturated Hg|$HgSO_4$ reference electrode (+640 mV vs. SHE) for determining the potential window of the metal-DLC electrodes. The electrochemical cell was completed with a segment of platinum foil as counter electrode, and DLC-coated silicon segments as the working electrode. DLC layers were pressed onto the bottom portion of the cell with the solution being contained by a Viton O-ring.

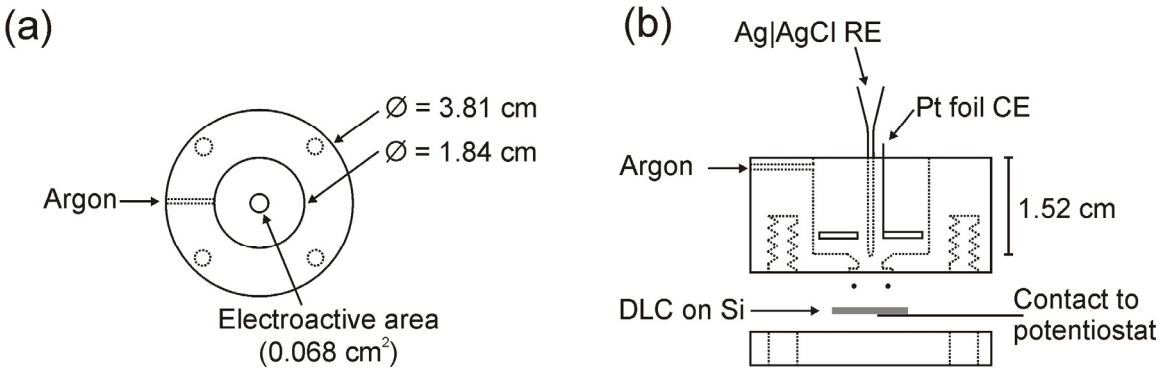

Figure 3.1: (a) Top and (b) side view of the custom-built Teflon cell utilized in the electrochemical characterization of DLC.

The geometric area exposed was 0.068 cm^2. 5 mM hexaammineruthenium(III) trichloride / hexaammineruthenium(II) dichloride ($Ru(NH_3)_6^{3+/2+}$), or 10 mM potassium hexacyanoferrate(III) / potassium hexacyanoferrate(II) trihydrate ($Fe(CN)_6^{3-/4-}$) in 0.1 M potassium chloride as supporting electrolyte (Aldrich, St. Louis, MA) were used as reversible redox mediator couples. The working potential windows were determined in a 0.5 M solution of sulfuric acid (Fisher Scientific, Fair Lawn, NJ). Since DLC is considered a semiconductor,[23] all electrochemical experiments were performed in the absence of light, thereby limiting photoconductive effects. All solutions were prepared with deionized water (Millipore Milli-Q, Billerica, MA) with a resistance of 18.2 MΩ·cm at 25 ºC, and were sparged with argon (Airgas, Marietta, GA) for at least 15 min prior to electrochemical analysis. All chemicals were used as received without further purification.

Heterogeneous electron transfer rate constants (k_s), and transfer coefficients (α) were obtained from simulations using the DigiElch software package.[24-26] Automatic iR compensation was applied to all voltammetric measurements.

The ATR spectroelectrochemical experiments were performed in the sample compartment of the infrared spectrometer equipped with a vertical ATR module (Specac, Norcross, GA). The top portion of the flow cell was custom built from polyether-ether ketone (PEEK) in order to accommodate the AgQRE reference electrode and the platinum foil counter electrode (*Figure 3.2*). The N-DLC layer was electrically contacted using four gold-coated pogo-pins (Emulation Technology, Santa Clara, CA). The cell volume was approximately 700 μL. A solution containing 0.2 M aniline with 1.0 M perchloric acid in water was filled through the PEEK spectroelectrochemical cell. The electropolymerization of aniline was performed via cyclic voltammetry sweeping from the open circuit potential (-0.05 V, vs. AgQRE) to +1.0 V (vs. AgQRE) at a scan rate of 0.005 V/s for a total of 40 cycles. Infrared spectra were acquired in-situ before the electropolymerization, and at the end of selected voltammetric cycles. No potential was applied during the spectroscopic measurement.

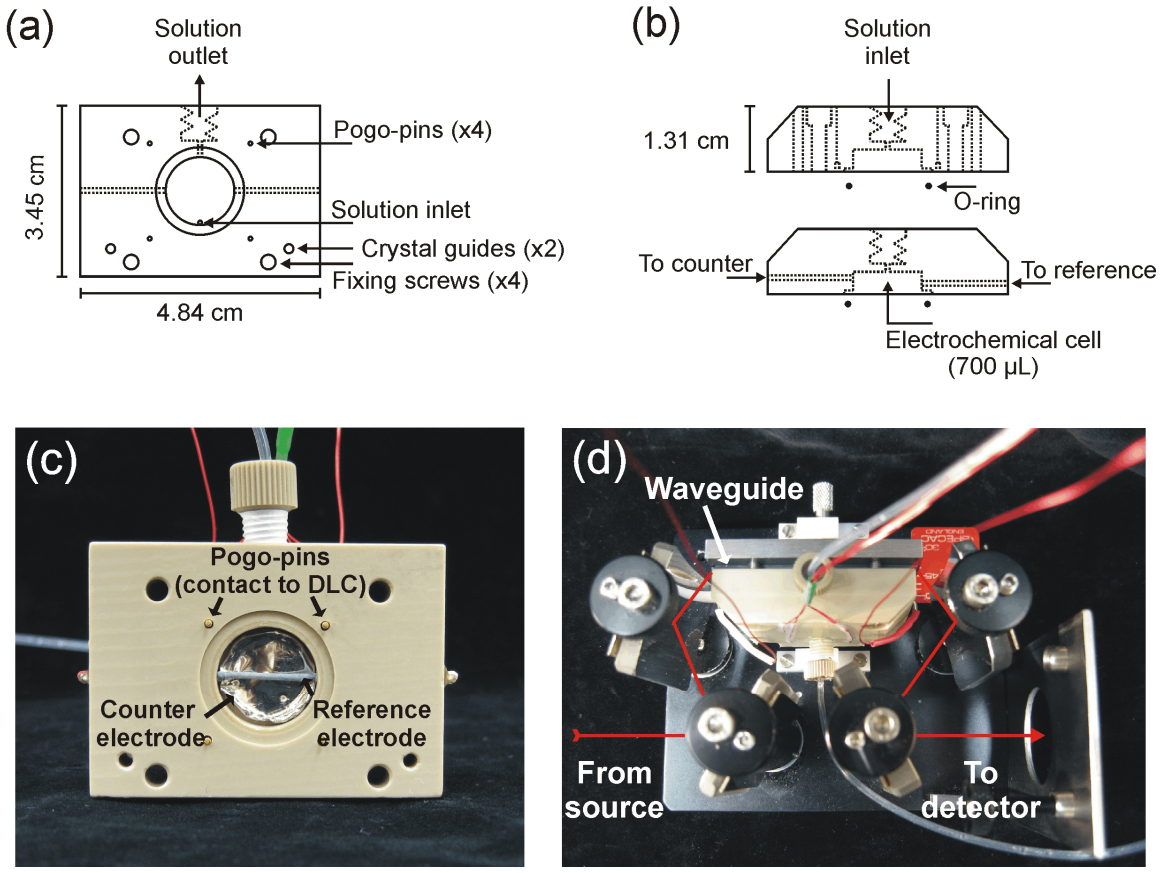

Figure 3.2: (a) Side and (b) top view schemes of the PEEK spectroelectrochemical cell. Optical micrographs of (c) the PEEK cover plate, and (d) the fully assembled spectroelectrochemical setup on the optical mirror bench.

3.3 Results

The error bars presented within this chapter reflect the variance (± 1σ) observed in a representative sample for nitrogen content.

3.3.1 X-ray photoelectron spectroscopy studies

X-ray photoelectron spectroscopy (XPS) provides information on the oxidation state of atoms in the top few layers of the sample (approx. 5 nm), as well as non-destructive compositional analysis.[27] Survey scans of the DLC surface indicates that the only elements present in measurable quantities are carbon, adventitious oxygen and nitrogen,

for N-DLC layers (*Figure 3.3(a)*). The obtained XPS data are particularly important since the electrochemical properties of carbon-based electrodes are intimately related to the fraction of sp^2-hybridized carbon atoms.[18, 28, 29] In general, the carbon 1s photoemission peaks collected for non-doped DLC layers are composed of sp^2-hybridized carbon at 284.4 ± 0.1 eV, sp^3-hybridized carbon at 285.2 ± 0.1 eV, and carbon bonded to adventitious oxygen at 286.5 eV.[30, 31] For nitrogen-doped DLC, superficial composition is derived from the ratio of the integrated peak areas adjusted with the proper sensitivity factors for each detected element.

Mathematical decomposition of the carbon 1s peak for the non-doped DLC layer reveals that approximately 30 % of the layer is sp^3-hybridized, resulting in a graphitic behavior of the layers (*Table 3.2*). The high fraction of sp^2-hybridized carbon is consistent with DLC layers deposited with lasers operating in the near-infrared range (*Section 3.2.1*).[32] The inclusion of nitrogen complicates the determination of the fraction of sp^3-hybridized carbon, as contributions from C-N bonds shift the carbon 1s photoemission peak to higher binding energies (*Figure 3.3(b)*).[33] The number of contributing constituents (i.e. C_{sp3}, C_{sp2}, C_{sp3}-N, C_{sp2}-N, and CO), leads to closely-spaced peak maxima (on average ~ 0.8 eV apart) resulting in ambiguous results. The variance in binding energies reported in the literature for each constituent reflects the fact that decomposition of C 1s peaks in N-DLC is still uncertain.[34-37]

Table 3.2: Compositional analysis of the N-DLC layers (n = 3).

Sample	Nitrogen gas concentration in chamber	Nitrogen concentration in layer	Percentage of sp^3-hybridized atoms	Oxygen/carbon ratio
Pure DLC	0 %	0 %	30 ± 7 %	0.12 ± 0.01
N #1	17 %	6.8 ± 0.8 %	--	0.11 ± 0.01
N #2	25 %	8.6 ± 0.3 %	--	0.12 ± 0.01
N #3	33 %	9.2 ± 0.9 %	--	0.11 ± 0.01

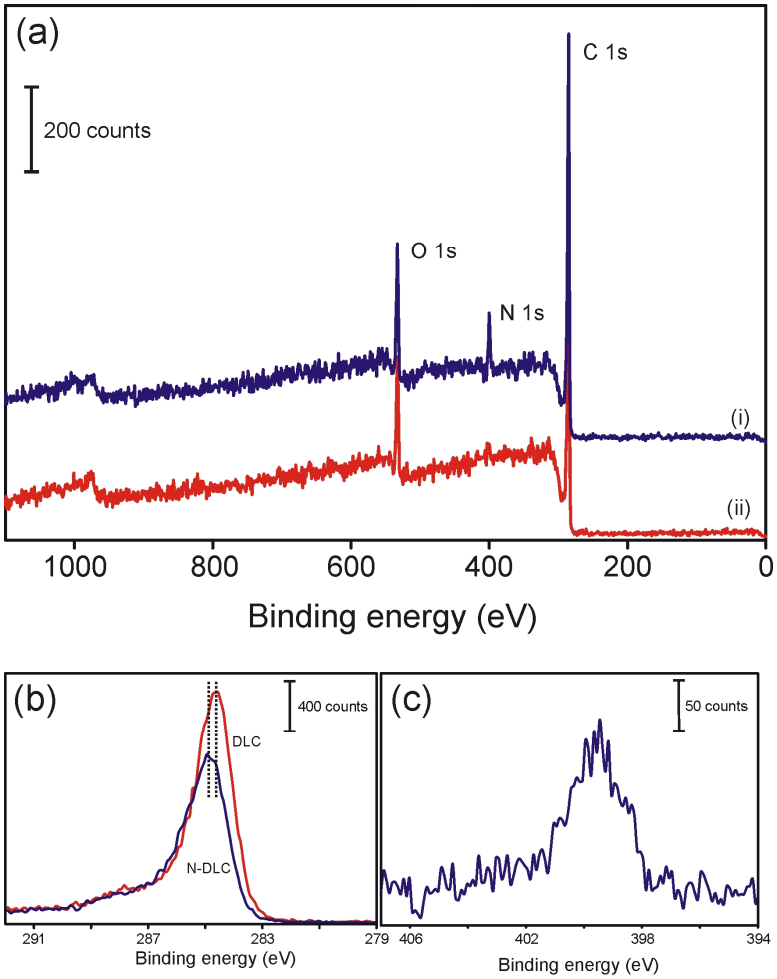

Figure 3.3: (a) X-ray photoelectron spectra of (i) N-DLC (sample N #2) and (ii) non-doped DLC. (b) High resolution C 1s photoemission peak doped and non-doped DLC, and (c) high resolution N 1s peak of N-DLC .

Alternatively, the nitrogen 1s photoemission peak can be utilized to monitor changes in carbon hybridization with nitrogen content.[35, 38-44] Three constituents are commonly described as contributing to the N 1s peak: N-C_{sp3} at approx. 398.4 eV, N-C_{sp2} at approx. 400.3 eV and NO/NN at approx. 402.5 eV. Unfortunately, quantitative information about the hybridization state of carbon in NC bonds derived from mathematical deconvolution of the N 1s peak is not possible due to the general disagreement in binding energies reported for each constituent. However, qualitatively, the N 1s photoemission peak corresponding to the N-DLC layers presented here are centered at approx. 399.6 eV, indicating that nitrogen is primarily bonded to sp^2-hybridized carbon (*Figure 3.3(c)*).

3.3.2 Raman spectroscopic studies

Raman spectroscopy of carbon layers is usually performed using a visible excitation source, typically in the green spectral region (488-532 nm).[45] The resulting Raman spectra are dominated by contributions from the sp^2-hybridized carbon atoms, due to a resonance effect of the excitation wavelength with the π states. As a result, the cross-section for sp^2-hybridized carbon atoms is up to 200 times higher than that of sp^3-hybridized carbon.[46]

The Raman spectra collected for DLC are commonly composed of a peak centered at approx. 1550 cm^{-1} (G-band) with a shoulder at approx. 1350 cm^{-1} (D-band).[47] The G-band is associated with the E_{2g} stretching mode of all sp^2-sites, regardless of their configuration (ring or olefinic chain). The D-band results from the A_{1g} breathing mode of six-membered carbon rings.[48] The combination of the band position, full width at half maximum (FWHM), and the ratio of the intensities of the two bands (I_D/I_G) provides direct information on the configuration of the sp^2- sites, and indirect information on the

sp^3-hybridized carbon content. Ferrari et al. described in detail the expected spectral changes, as the bond-angle disorder and the sp^3-carbon content increase, proposing a three stage classification based upon the carbon layer morphology (*Figure 3.4*):[46]

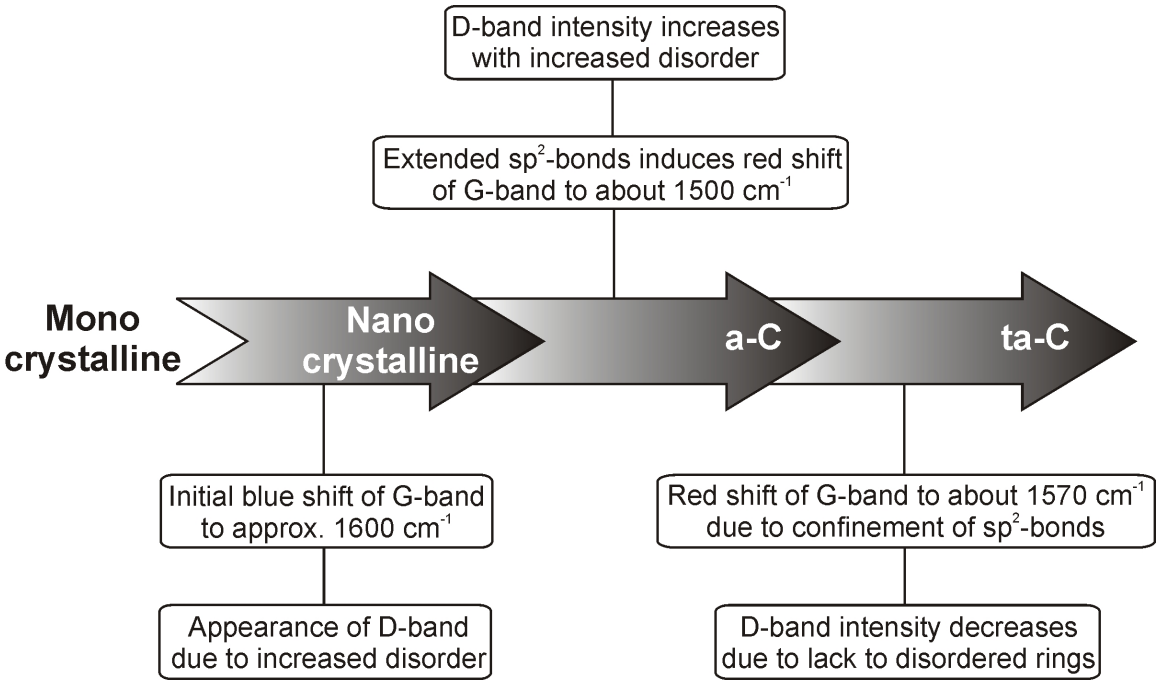

Figure 3.4: Anticipated changes in the Raman spectra of carbon films with increasing disorder and sp^3-hybridized carbon content.

Representative Raman spectra of non-doped and nitrogen-doped DLC are shown in *Figure 3.5*. In general, the vibrational frequencies of the C-N bonds cannot be separated from those of the C-C bonds, rendering the interpretation of the D- and G-bands identical to non-doped DLC.[46]

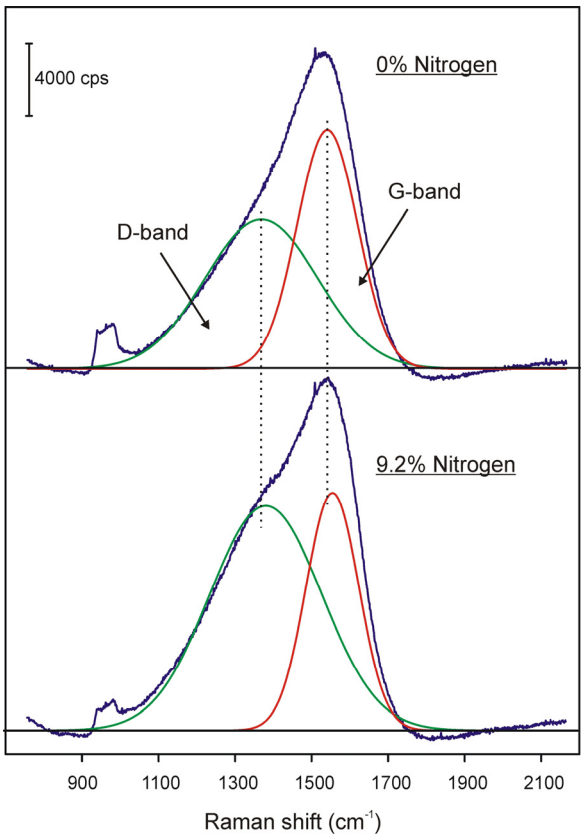

Figure 3.5: Visible Raman spectra of non-doped and nitrogen-doped DLC layers.

Upon addition of nitrogen, the most prominent changes in the Raman spectra are the I_D/I_G, which increases from ~ 0.7 to ~ 1.0 (*Figure 3.6(a)*), and the FWHM of the G-band, which decreases from ~ 185 to ~ 160 cm^{-1} (*Figure 3.6(b)*). These variations show that the addition of nitrogen causes an increase in the sp^2-hybridized carbon cluster size, as well as increased ordering of the sp^2-carbon phase.[49] The minor blue shift exhibited by the G-band further confirms the increased cluster size.[46]

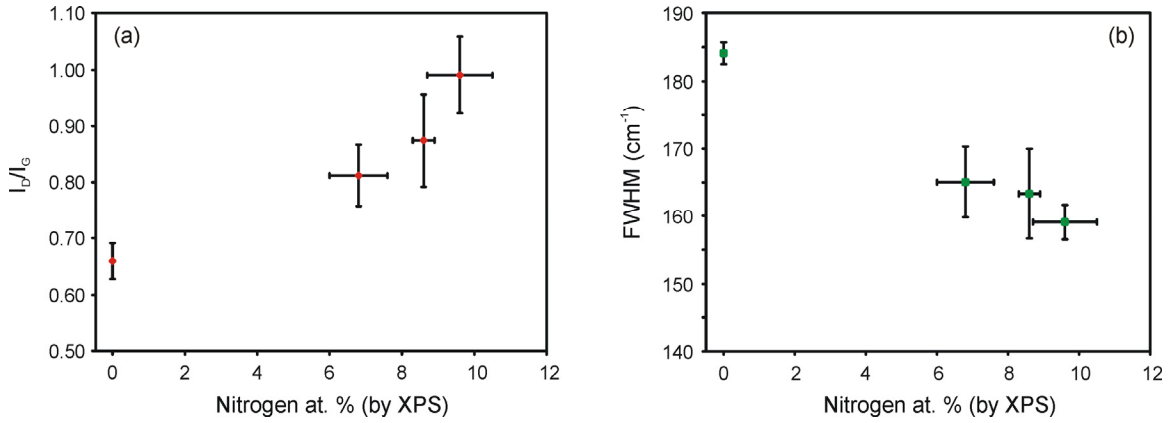

Figure 3.6: Changes in (a) I_D/I_G and (b) FWHM of the G-band with respect to the nitrogen content (n = 3).

3.3.3 Mid-infrared spectroscopic studies

For mid-IR studies, non-doped and doped DLC layers were deposited onto ZnSe ATR waveguides. The thickness of the layers was 28 ± 7 nm (n = 3) for non-doped and 43 ± 8 nm (n = 3) for nitrogen-doped DLC. Infrared transparency was maintained for both layers (*Figure 3.7(a)*). A small absorption feature at approximately 1300 cm^{-1} is observed for the non-doped DLC layer, which is related to the delocalization of π electron density of conjugated C=C bonds in layers with a high fraction of sp^2-carbon (*Figure 3.7(b)*).[49] This absorption feature is nearly absent in ta-C layers, as the π density is localized in small sp^2-carbon clusters. The incorporation of nitrogen into DLC layers increases the intensity of the absorption band, and in addition results in a broadening effect. The incorporation of nitrogen promotes sp^2-bonding and the formation of larger cluster sizes. Accordingly, an increased intensity for the broad band at 1300 cm^{-1} was observed. Broadening of the absorption band is related to the formation of C=N bonds, which display absorption features at wavelengths similar to C=C bonds.[49-51]

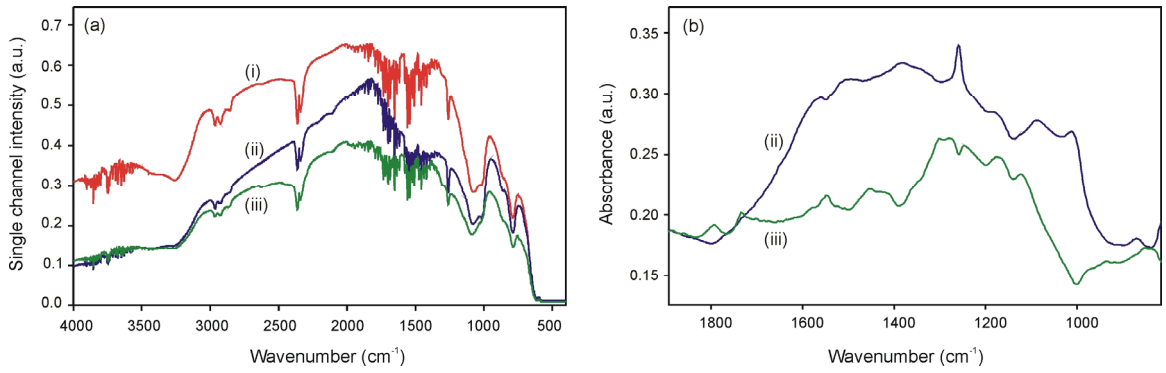

Figure 3.7: (a) Single beam spectra of (i) bare ZnSe, (ii) N-DLC coated ZnSe, and (iii) non-doped DLC coated ZnSe. The C=N and C=C absorption features in (ii) N-DLC, and (iii) non-doped DLC are shown in (b).

3.3.4 Electrochemical studies

Despite the absence of dopant, the non-doped layer exhibits sufficient conductivity to allow significant electron transfer. The observed electrochemical activity results from the high fraction of sp^2-hybridized carbon.[11] *Table 3.3* summarizes the peak separations for $Ru(NH_3)_6^{3+/2+}$ and $Fe(CN)_6^{3-/4-}$ determined by cyclic voltammetry at untreated DLC layers.

Table 3.3: Peak separation for the $Ru(NH_3)_6^{3+/2+}$ and $Fe(CN)_6^{3-/4-}$ redox couples at (N-)DLC layers at 0.1 V/s (n = 3).

Sample	Nitrogen concentration	ΔE ($Ru(NH_3)_6^{3+/2+}$) (mV)	ΔE ($Fe(CN)_6^{3-/4-}$) (mV)
Pure DLC	0 %	81 ± 19	367 ± 84
N #1	6.8 ± 0.8 %	78 ± 16	321 ± 58
N #2	8.6 ± 0.3 %	84 ± 6	364 ± 34
N #3	9.2 ± 0.9 %	72 ± 2	303 ± 80

The Raman spectra of N-DLC layers (*Section 3.3.2*) show that the incorporation of nitrogen increases the sp^2-hybridized carbon cluster size, which is in agreement with

previous reports.[49, 52-54] However, the data presented in *Table 3.3* does not show a correlation between the nitrogen (or sp^2-carbon) content and the peak separation for either mediator couple. This indicates that the increase in sp^2-carbon cluster size does not significantly affect the electrochemical properties.

Heterogeneous electron transfer rate constants (k_s) were derived from the recorded CVs, and are summarized in *Table 3.4*.

The diffusion coefficients (in 0.1 M KCl) used for the simulations were 7.6×10^{-6} cm/s^2 and 6.5×10^{-6} cm/s^2 for $Fe(CN)_6^{3-}$ and $Fe(CN)_6^{4-}$, respectively.[55] The diffusion coefficient for $Ru(NH_3)_6^{2+}$ was determined experimentally by cyclic voltammetry and calculated using the Randles-Sevčik equation[55]. The obtained value is $5.5 \pm 0.5 \times 10^{-6}$ cm/s^2. A diffusion coefficient of $9.2 \pm 0.7 \times 10^{-6}$ cm/s^2 was experimentally determined for $Ru(NH_3)_6^{3+}$, which is in agreement with values reported elsewhere.[56]

Table 3.4: Kinetic parameters for the $Ru(NH_3)_6^{3+/2+}$ and $Fe(CN)_6^{3-/4-}$ redox couples for untreated DLC layers at 0.1 V/s (n = 3).

Sample	$Ru(NH_3)_6^{3+/2+}$ k_s ($\times 10^{-2}$ cm/s)	$Fe(CN)_6^{3-/4-}$ k_s ($\times 10^{-4}$ cm/s)	$Ru(NH_3)_6^{3+/2+}$ α	$Fe(CN)_6^{3-/4-}$ $1-\alpha$
Pure DLC	1.1 ± 1.0	3.9 ± 2.5	0.59 ± 0.04	0.43 ± 0.09
N #1	2.6 ± 3.1	4.5 ± 2.0	0.56 ± 0.02	0.47 ± 0.05
N #2	1.0 ± 0.3	3.7 ± 1.4	0.59 ± 0.04	0.46 ± 0.04
N #3	2.3 ± 0.5	5.9 ± 2.7	0.46 ± 0.07	0.4 ± 0.07

The k_s values for both redox couples display a significant variance, regardless of nitrogen content. Deslouis and co-workers[57, 58] observed that areas with increased electrochemical activity were present at untreated N-DLC surfaces. The k_s values reported at different positions on the same sample varied by 2 orders of magnitude. Our findings confirm the

heterogeneity of N-DLC surfaces as demonstrated by the variance in k_s values reported in *Table 3.4*.

A comparison of the k_s values of the two mediators reveals that the electron transfer for the $Ru(NH_3)_6^{3+/2+}$ couple occurs much faster than for the $Fe(CN)_6^{3-/4-}$ couple. Although an outer-sphere mechanism is commonly attributed to both mediators, in contrast to $Ru(NH_3)_6^{3+/2+}$, the surface oxide composition of carbon electrodes complicates the electronic transfer for $Fe(CN)_6^{3-/4-}$ rendering it in fact similar to an inner-sphere mechanism.[59] A low concentration of surface oxides (< 0.15 O/C[60]) does not significantly influence the rate of electron transfer.[61] Hence, the O/C ratios obtained for the N-DLC layers (*Table 3.2*) do not significantly influence the electrochemical behavior observed for $Fe(CN)_6^{3-/4-}$. Although the electron transfer mechanism for $Fe(CN)_6^{3-/4-}$ at carbon surfaces is not fully understood,[59] McCreery and co-workers[60] demonstrated that the electron transfer rate for $Fe(CN)_6^{3-/4-}$ is reduced at a carbon surface covered by a monolayer, such as nitrophenyl. This suggests that adsorption of $Fe(CN)_6^{3-/4-}$ onto the surface is necessary for a fast electron transfer, similar to inner-sphere mechanisms.[55]

The electron transfer rate of $Fe(CN)_6^{3-/4-}$ at glassy carbon and BDD electrodes also decreases significantly upon exposure of the electrodes to atmosphere for extended periods of time.[62-65] Water contact angle measurements revealed that carbon surfaces become increasingly hydrophobic with time, due to the physisorption of hydrocarbon impurities present in the atmosphere.[62, 66] The N-DLC layers presented throughout this thesis were analyzed approx. 45 days after deposition. Therefore, N-DLC layers will contain a passivating layer similar to glassy carbon and BDD electrodes.

The surface reactivity of passivated carbon electrodes can be restored by electrochemical or physical pretreatment procedures prior to the electrochemical analysis. Electrochemical procedures discussed in the literature involve anodic[67] or cathodic[68] polarization, and potential sweeping.[69] Physical procedures rely upon renewal of the electrode surface by laser ablation,[70] heat treatment in vacuum, [64, 71] or plasma etching.[61, 62]

For N-DLC thin films, Cachet et al.[58] showed that electrochemical potential cycling between -0.25 V (vs. SHE) and -1.25 V (vs. SHE) at a scan rate of 0.05 V/s in 0.5 M H_2SO_4 for 15 cycles, yields substantially improved electron transfer rates for the $Fe(CN)_6^{3-/4-}$ couple. Since hydrogen gas evolution may lead to delamination of the DLC layer from the substrate, the procedure of Cachet et al. was modified for this study. The potential window was limited to cycling from -0.1 V to -1.1 V (vs. SHE) resulting in similar values as reported by Cachet et al.[58].

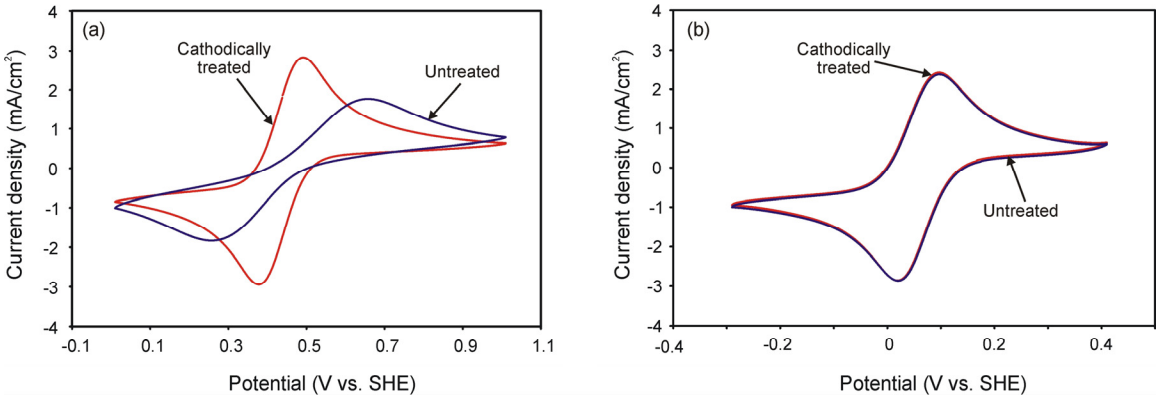

Figure 3.8: Cyclic voltammograms (v = 0.1 V/s) of (a) $Fe(CN)_6^{3-/4-}$, and (b) $Ru(NH_3)_6^{3+/2+}$ untreated and after cathodic pretreatment in 0.5 M sulfuric acid.

Figure 3.8 shows representative cyclic voltammograms of the two redox mediators at non-doped DLC layer. The cathodic pretreatment significantly alters the voltammetric

response of $Fe(CN)_6^{3-/4-}$ couple, while leaving that of $Ru(NH_3)_6^{3+/2+}$ essentially unchanged, as expected.

In contrast to anodically pretreated carbon electrodes, where increased oxygen-to-carbon ratios (O/C) are observed,[62, 69, 72, 73] cathodic pretreatments do not significantly alter the O/C values.[65, 72] A detailed mechanism for treated surfaces has not yet been established, due to the complex composition of oxidized carbon surfaces.[59] However, XPS analysis of cathodically treated surfaces have shown increased contributions from hydroxyl groups to the carbon 1s peak in exchange for carbonyls.[69, 72, 74] Faradaic currents measured at potentials corresponding to the reduction of carbonyls (e.g. quinines) to hydroxyl groups provide further evidence that the electrode surface is changed during cathodic pretreatment.[75] However, the influence of hydroxyl groups on the removal of the passivating hydrocarbon layer has not been elucidated to date.

The peak potential separation for $Ru(NH_3)_6^{3+/2+}$ and $Fe(CN)_6^{3-/4-}$, and the kinetic parameters for cathodically treated layers are provided in *Table 3.5* and *Table 3.6*, respectively. As anticipated, the k_s values for $Fe(CN)_6^{3-/4-}$ of the cathodically treated electrodes increased by one order of magnitude compared to untreated N-DLC.

Table 3.5: Peak separation of $Ru(NH_3)_6^{3+/2+}$ and $Fe(CN)_6^{3-/4-}$ redox couples for cathodically treated (N-)DLC layers at 0.1 V/s (n = 3).

Sample	Nitrogen concentration	ΔE ($Ru(NH_3)_6^{3+/2+}$) (mV)	ΔE ($Fe(CN)_6^{3-/4-}$) (mV)
Pure DLC	0 %	79 ± 4	96 ± 13
N #1	6.8 ± 0.8 %	75 ± 2	118 ± 24
N #2	8.6 ± 0.3 %	75 ± 8	110 ± 4
N #3	9.2 ± 0.9 %	68 ± 16	91 ± 12

Table 3.6: Kinetic parameters for the $Ru(NH_3)_6^{3+/2+}$ and $Fe(CN)_6^{3-/4-}$ redox couples for cathodically treated (N-)DLC layers at 0.1 V/s (n = 3).

Sample	$Ru(NH_3)_6^{3+/2+}$ k_s ($\times 10^{-2}$ cm/s)	$Fe(CN)_6^{3-/4-}$ k_s ($\times 10^{-3}$cm/s)	$Ru(NH_3)_6^{3+/2+}$ α	$Fe(CN)_6^{3-/4-}$ $1-\alpha$
Pure DLC	1.3 ± 0.7	6.6 ± 0.9	0.61 ± 0.11	0.43 ± 0.09
N #1	1.3 ± 0.1	4.7 ± 2.2	0.59 ± 0.04	0.47 ± 0.05
N #2	1.7 ± 1.0	4.6 ± 0.3	0.60 ± 0.07	0.46 ± 0.04
N #3	1.9 ± 1.8	9.7 ± 4.0	0.60 ± 0.04	0.4 ± 0.07

The k_s values obtained for the N-DLC studied herein reveal that after the cathodic treatment, the electron transfer rate of these electrodes is comparable to that of moderately doped boron-doped diamond electrodes, and to that of N-DLC layers published in literature (*Table 3.7*).

Table 3.7: Comparison of k_s values obtained with N-DLC electrodes in this study with those published for several carbon electrodes in literature.

Electrode type	$Ru(NH_3)_6^{3+/2+}$ k_s (cm/s)	$Fe(CN)_6^{3-/4-}$ k_s (cm/s)	Comment	Reference
BDD	0.1 – 0.01	0.1 – 0.01	Micro- and nanocrystalline	[76]
NDD	0.1 – 0.01	0.1 – 0.01	Nitrogen-doped microcrystalline	[77]
Glassy carbon	0.24	0.1	Freshly polished	[78]
H-glassy carbon	0.02	0.03	Hydrogen plasma treated	[63]
a-C:H:N	n/a	< 0.0001 [a]	Hydrogenated N-DLC	[18]
ta-C:N	~ 0.001[a]	n/a	"High" sp^3-content	[13]
a-C:N	n/a	~ 0.06[a]	Hydrogen-free	[15]
a-C:N	n/a	~ 0.01[a]	Hydrogen-free, after cathodic treatment	[58]
a-C:N	**~ 0.01**	**~ 0.005**	**This work, after cathodic treatment**	

[a] k_s values were not provided by the authors, instead they were approximated using the method of Nicholson and Shain[79] assuming $D_O = D_R$ and $\alpha = 0.5$.

Working potential windows of up to 3.7 V for N-DLC electrodes have been reported in the literature.[12, 15, 16] The developed (N-)DLC layers display working potential windows of approx. 2.8 V, at ± 1.0 mA/cm^2 in 0.5 M H_2SO_4 (*Figure 3.9*(a)). The formation of gaseous products, such as O_2, requires the adsorption of reactive species at the surface of the electrode.[80] The presence of a high sp^2-carbon content in (N-)DLC facilitates the adsorption of such species, resulting in a narrower potential window, similar to other sp^2-carbon electrodes. In contrast, the surface of BDD and hydrogenated DLC electrodes is C-H terminated, and are considered inert with respect to the adsorption of chemical species. Hence, the adsorption of reactive species is hindered and gas evolution is delayed.[81, 82] The observed increase in Faradaic current at potentials lower than -0.2 V (vs. SHE) are attributed to the reduction of surface quinone to phenolic chemical functionalities.[83] During the anodic portion of the scan, the carbon surface is oxidized at potentials greater than 0.9 V (vs. SHE), resulting in an increasing O/C ratios, as reported in the literature.[62, 69, 72, 73]

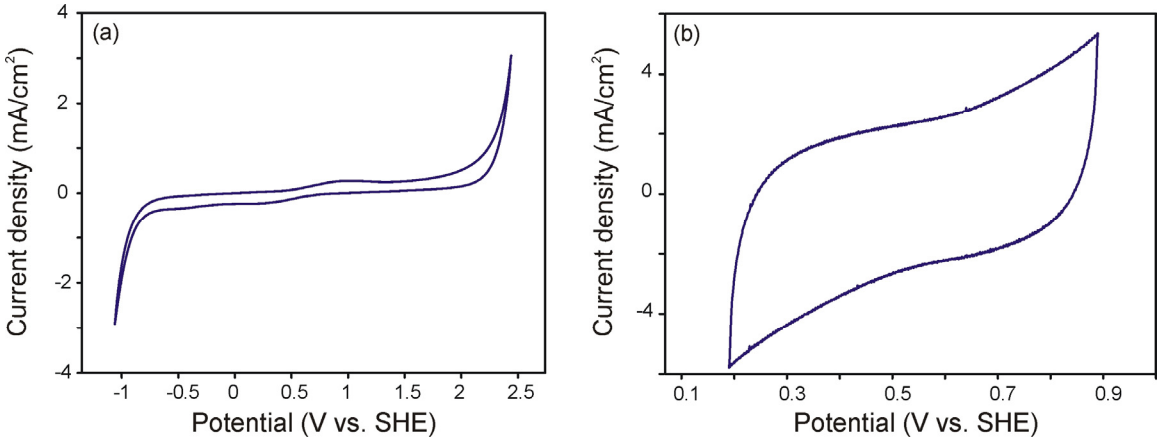

Figure 3.9: Representative cyclic voltammograms utilized in the determination of (a the) working potential window (v = 0.1 V/s) and (b) double layer capacitance (v = 100 V/s) of DLC in 0.5 M H_2SO_4.

Double layer capacitance values of approx. 25 μF/cm^2 were recorded for (N-)DLC layers in the 0.19 V to 0.89 V (vs. SHE) potential range (*Figure 3.9*(b)). Similar to glassy carbon electrodes, N-DLC exhibits surface redox-active CO moieties contributing to background currents. In contrast, high quality BDD electrode surfaces are nearly exclusively C-H terminated (i.e. redox-inactive), hence C_{dl} values below 10 μF/cm^2 are usually achievable.[84] As seen in *Figure 3.9*(a), in the potential region selected Faradaic currents resulting from oxidation and reduction of surface CO moieties are minimized, providing a more accurate measure of C_{dl}.

3.3.5 Spectroelectrochemical studies

Due to the refractive index of ZnSe (n = 2.43 at 5 μm), the penetration depth of the evanescent field for ATR ZnSe waveguides is greater than for other common ATR materials, such as germanium and silicon (*Section 2.1*). KRS-5 and zinc sulfide ATR crystals display similar optical properties to ZnSe, however these materials are toxic and provide a narrower optical window, respectively.[85]

N-DLC deposited onto ZnSe waveguides allows approx. 50 % of the incident radiation to propagate, despite a broad absorption band from 1000 to 1600 cm^{-1} (*Section 3.3.3*). XPS analysis revealed that the N-DLC coating contained 7.3 ± 0.8 % nitrogen, (n = 3) which is in close agreement to layer N #2 deposited onto silicon at the same conditions (see *Table 3.2*).

As outlined in the introductory chapter of this thesis, the motivation for this study was the development of optically transparent DLC electrodes for multi-reflection ATR spectroelectrochemical platforms. The main goal was to utilize the electrode material for electropolymerizing a partitioning membrane directly onto the waveguide substrate,

thereby enabling spectroscopic monitoring of the incorporation of electroactive species with the applied potential. Coating N-DLC layers with a membrane would provide for (1) the selective enrichment of selected analytes, and (2) rejection of potential spectroscopic interferants.

Poly(4-vinylpyridine) is an electropolymerizable anion-exchange polymer, preferentially enriching $Fe(CN)_6^{3-/4-}$ (a detailed discussion of poly(4-VP) membranes is presented in *Chapter 5*). The cathodic electropolymerization of poly(4-VP) requires potentials as high as -2.2 V (vs. SHE). Since deposited thin film electrodes are prone to increased stress and delamination from the substrate due to applied electric fields,[86] initial spectroelectrochemical studies were performed with the aniline monomer which can be electropolymerized at lower potentials (+1.0 V vs. SHE).

The infrared ATR spectrum of the solution prior to the electrochemical experiment containing the monomer and supporting electrolyte is shown in *Figure 3.10*. The water band at approximately 3300 cm^{-1} exhibits a negative absorbance (compared to the pure water background), due to the monomer and supporting electrolyte partially displacing water molecules from the volume probed by the evanescent field.

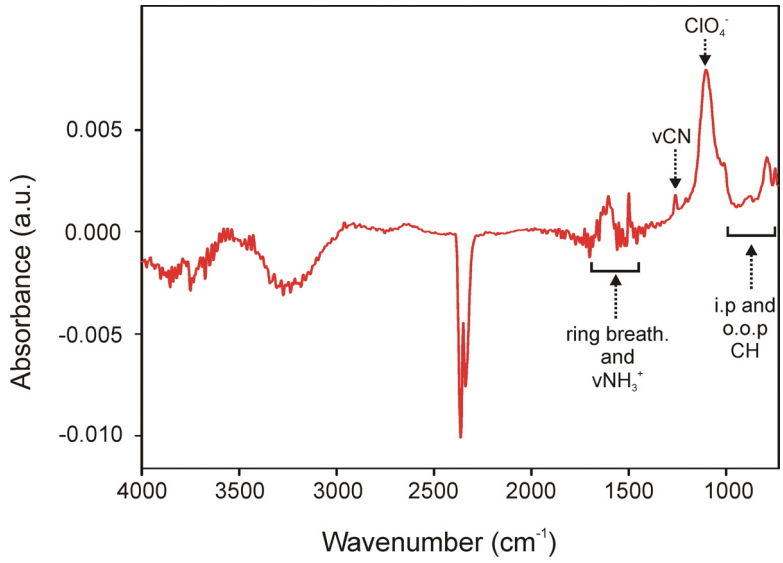

Figure 3.10: ATR infrared spectrum of 0.2 M aniline / 1 M perchloric acid in water. The background spectra were collected in deionized water.

Upon electropolymerization, several spectral features pertaining to the polymer formation increase in intensity with the corresponding voltammetric cycles (*Figure 3.11*(a)). The most prominent spectral features are summarized in *Table 3.8*. As the polymer layer grows, the segment of the evanescent field closer to the waveguide is prevented from interacting with the solution. Consequently, the water bands at approx. 3300 cm^{-1} exhibits an increasingly negative absorbance compared to the background scan performed prior to the electropolymerization (*Figure 3.11*(b)).

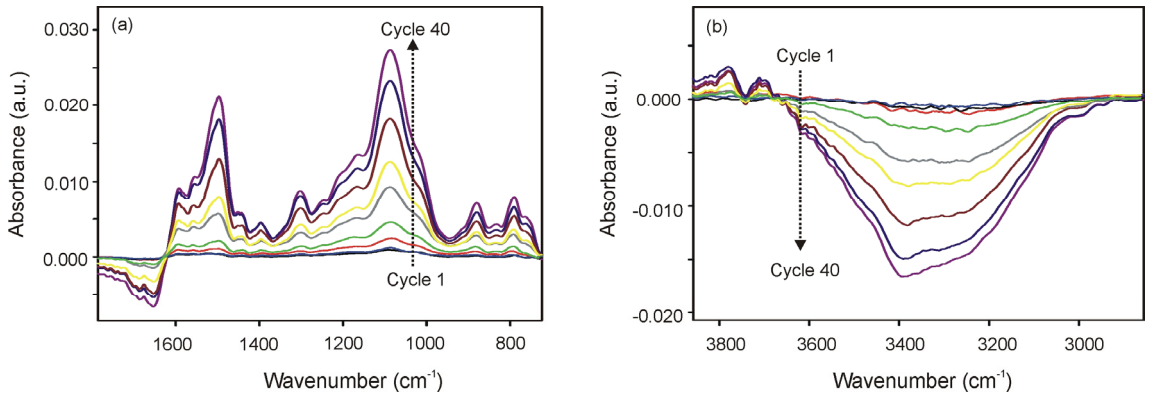

Figure 3.11: Infrared spectra of PANI growth with increasing voltammetric cycles. (a) shows the increasing absorption intensities of the polymer bands, (b) shows the decreasing water absorption.

Table 3.8: Spectral assignment of the absorption bands in *Figure 3.11*(a).

Wavenumber (cm^{-1})	Assignment
1596	ring breathing
1558	ring breathing
1498	ring breathing
1400	CN stretch
1304	CN stretch
1171	in-plane CH bending
1089	ClO_4^-
791	out-of-plane CH deformation

Integrating the areas underneath the polymer (1363 – 946 cm^{-1} in *Figure 3.11(a)*) and water absorption bands (3690 – 2924 cm^{-1} in *Figure 3.11(b)*) results in a linear relationship between the observed spectroscopic changes and the number of voltammetric cycles (*Figure 3.12(a)*). Additionally, a linear relationship is obtained by plotting the ratio of the two integrated areas, indicating that the rate with which the absorption

features change is the same (*Figure 3.12(b)*). Hence, the measured spectral changes are related to the same phenomenon, that is, growth of the PANI film.

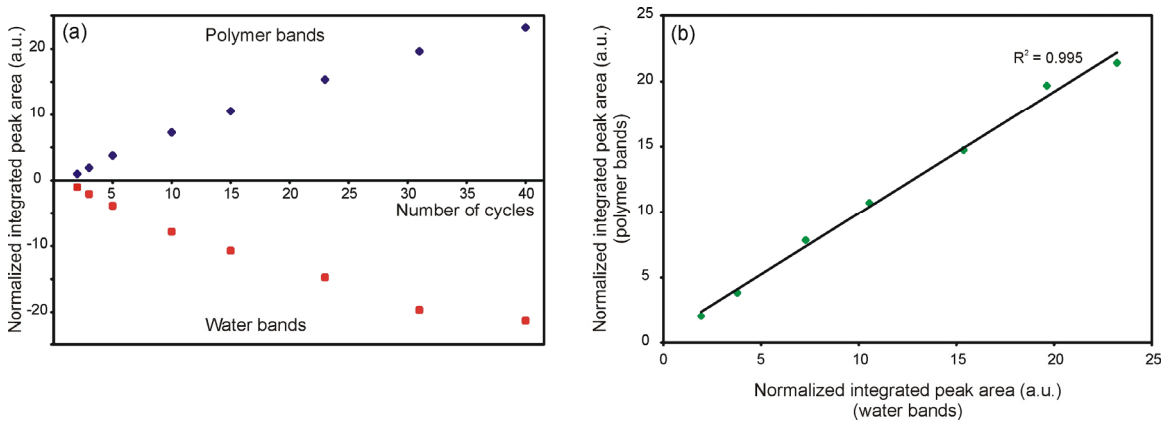

Figure 3.12: (a) Normalized integrated areas for the polymer (1363 – 946 cm^{-1}) and water (3690 – 2924 cm^{-1}) bands shown in Figure 3.11 and (b) absolute value of the ratio of the integrated areas.

The cyclic voltammograms performed at N-DLC deposited onto ZnSe (Figure *3.13(a)*) reveal little information on the electropolymerization process, compared to the same N-DLC layer deposited on silicon (Figure *3.13(b)*). The homogeneous electron transfer for N-DLC deposited onto doped silicon occurs through the vertical axis of the layer. In contrast, for the spectroelectrochemical studies N-DLC was deposited onto insulating ZnSe resulting in homogeneous electronic conduction occurring from the point-of-contact (the pogo-pin) into the electrochemical cell, which corresponds to a distance of ~ 4 mm. Sheet resistances of up to 1000 Ω/□ have been reported for N-DLC layers.[14] Comparably high sheet resistance values for indium-tin oxide thin films have resulted in nearly featureless cyclic voltammograms, whereas layers with sheet resistances of ~ 10 Ω/□ displayed acceptable electrochemical behavior.[87] Hence, lowering the sheet

resistance of N-DLC, favorable electrochemical properties can be obtained with coated mid-IR waveguides.

The PANI layer obtained at N-DLC on ZnSe after 40 cycles is characterized by a thickness of 70 ± 6 nm (n = 3) (*Figure 3.14*).

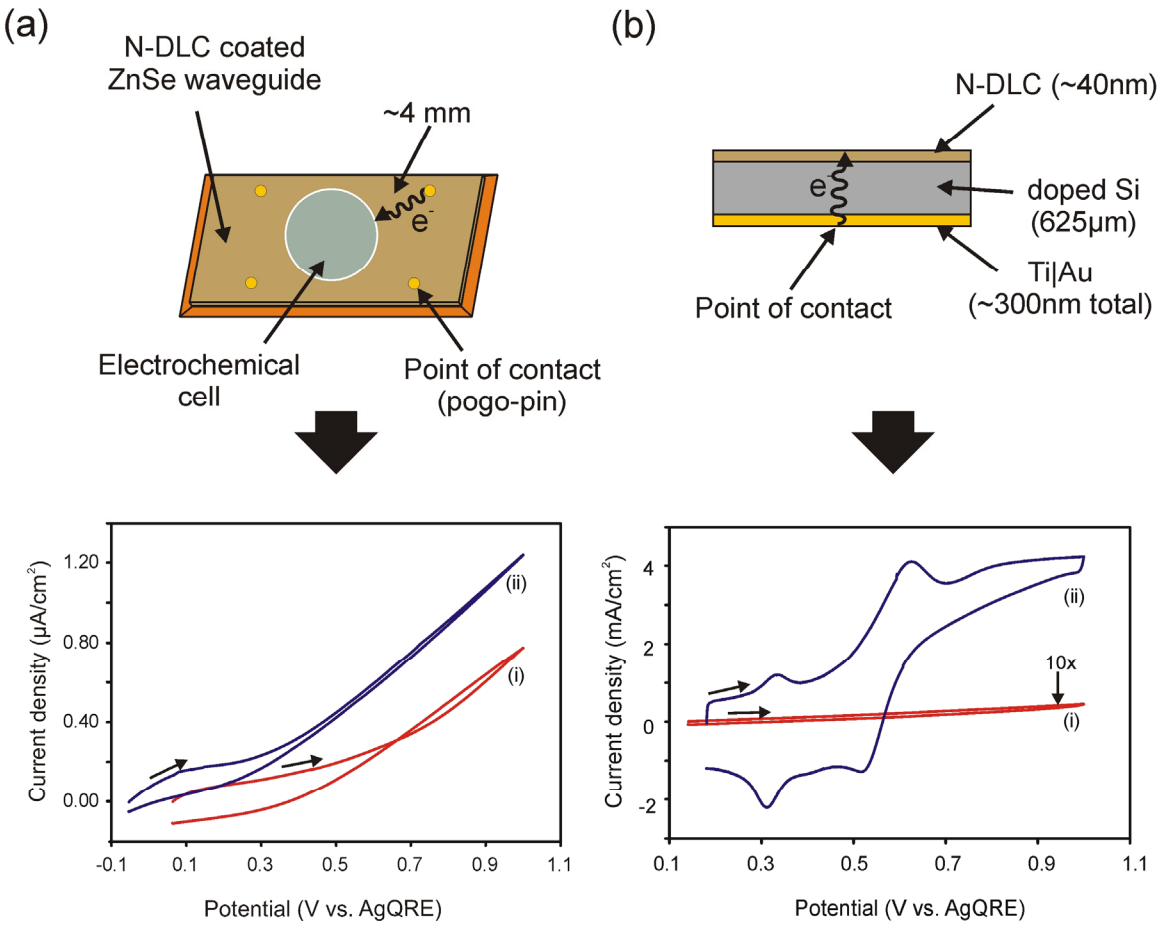

Figure 3.13: Cyclic voltammograms of a solution containing (i) 1 M perchloric acid and (ii) 0.2 M aniline and 1 M perchloric acid from the open circuit potential to +1.0 V (vs. AgQRE) at 0.005 V/s. The working electrode was (a) N-DLC on ZnSe, and (b) N-DLC on doped Si (5th cycle shown).

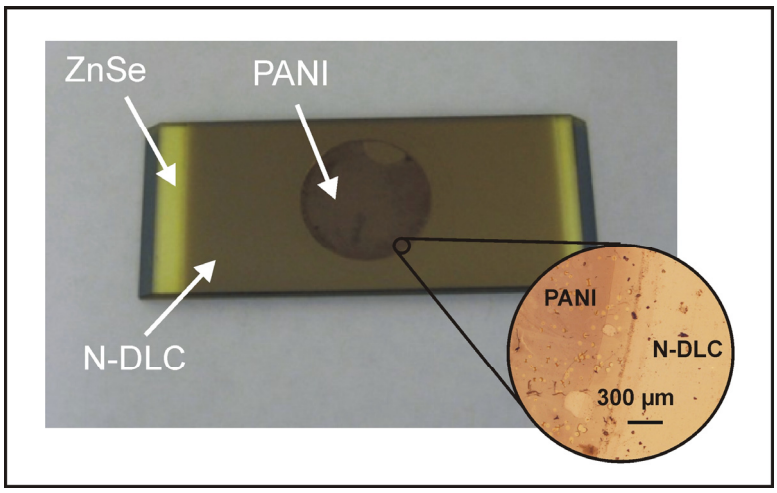

Figure 3.14: Optical image of electropolymerized PANI on N-DLC coated ZnSe waveguide. The inset shows the PANI layer at a higher magnification at the edge of the electrochemical cell.

3.4 Final remarks

The physical and electrochemical properties of nitrogen-doped diamondlike carbon layers developed in this study have been described. Due to the high fraction of sp^2-hybridized carbon, the non-doped layer exhibited equal electrochemical properties to doped layers. Pre-treatment of N-DLC layers with cathodic potential sweeping in sulfuric acid resulted in an improved electron transfer rate towards the $Fe(CN)_6^{3-/4-}$ redox couple. Deposition of DLC onto ZnSe confirmed that mid-IR transparency is maintained at multi-reflection waveguides.

The first application of N-DLC coated waveguides to multi-reflection ATR spectroelectrochemistry was demonstrated via the electropolymerization of polyaniline. Several infrared spectroscopic changes related to polymer growth were monitored at N-DLC modified ZnSe waveguides.

Future work will focus on decreasing the sheet resistance of N-DLC layers in order to obtain improved electrochemical behavior of N-DLC/ZnSe waveguides in addition to the

spectroscopic information. Finally, based on the obtained results future depositions of N-DLC layers will be immediately treated with a hydrogen plasma after deposition, in order to delay the adsorption of atmospheric impurities aiming at preserving high electrochemical activity for extended periods.[62, 63]

3.5 References

1. Stotter, J.; Show, Y.; Wang, S.; Swain, G., *Comparison of the Electrical, Optical, and Electrochemical Properties of Diamond and Indium Tin Oxide Thin-Film Electrodes*, Chem. Mater., **17 (19)**, 4880-4888, (2005).

2. Christensen, P. A., *In situ infrared spectroelectrochemistry*, Encyclopedia of Electrochemistry, **3**, 530-571, (2003).

3. Christensen, P. A.; Hamnett, A., *In-situ infrared studies of the electrode-electrolyte interface*, Compr. Chem. Kinet., **29**, 1-77, (1989).

4. Flowers, P. A.; Callender, S.-A., *Variable Path Length Transmittance Cell for Ultraviolet, Visible, and Infrared Spectroscopy and Spectroelectrochemistry*, Anal. Chem., **68 (1)**, 199-202, (1996).

5. Korzeniewski, C., *Infrared spectroscopy in electrochemistry: new methods and connections to UhV surface science*, Crit. Rev. Anal. Chem., **27 (2)**, 81-102, (1997).

6. Janotta, M.; Rudolph, D.; Kueng, A.; Kranz, C.; Voraberger, H.-S.; Waldhauser, W.; Mizaikoff, B., *Analysis of Corrosion Processes at the Surface of Diamond-Like Carbon Protected Zinc Selenide Waveguides*, Langmuir, **20 (20)**, 8634-8640, (2004).

7. Janotta, M.; Vogt, F.; Voraberger, H.-S.; Waldhauser, W.; Lackner Jurgen, M.; Stotter, C.; Beutl, M.; Mizaikoff, B., *Direct analysis of oxidizing agents in aqueous solution with attenuated total reflectance mid-infrared spectroscopy and diamond-like carbon protected waveguides*, Anal. Chem., **76 (2)**, 384-391, (2004).

8. Schnupp, R.; Kuhnhold, R.; Temmel, G.; Burte, E.; Ryssel, H., *Thin carbon films as electrodes for bioelectronic applications*, Biosens. Bioelectron., **13 (7-8)**, 889-894, (1998).

9. Bouamrane, F.; Kautek, W.; Sahre, M.; Tadjeddine, A.; Rzepka, E.; Levy-Clement, C., *Electrochemistry at undoped and doped diamond-like carbon films grown by UHV pulsed laser deposition*, Proc. - Electrochem. Soc., **97-32 (Proceedings of the International Symposium on Diamond Materials, 5th, 1997)**, 309-323, (1998).

10. Moon, J.-M.; Park, S.; Lee, Y.-K.; Sook Bang, G.; Hong, Y.-K.; Park, C.; Cheol Jeon, I., *Diamond-like carbon electrodes in electrochemical microgravimetry*, J. Electroanal. Chem., **464 (2)**, 230-237, (1999).

11. Niwa, O.; Jia, J.; Sato, Y.; Kato, D.; Kurita, R.; Maruyama, K.; Suzuki, K.; Hirono, S., *Electrochemical Performance of Angstrom Level Flat Sputtered Carbon Film Consisting of sp2 and sp3 Mixed Bonds*, J. Am. Chem. Soc., **128 (22)**, 7144-7145, (2006).

12. Yoo, K.; Miller, B.; Kalish, R.; Shi, X., *Electrodes of nitrogen-incorporated tetrahedral amorphous carbon. A novel thin-film electrocatalytic material with diamond-like stability*, Electrochem. Solid-State Lett., **2 (5)**, 233-235, (1999).

13. Yee, N. C.; Shi, Q.; Cai, W.-B.; Scherson, D. A.; Miller, B., *Electrochemical characterization of nitrogen-incorporated tetrahedral carbon films grown by a filtered cathodic vacuum arc*, Electrochem. Solid-State Lett., **4 (10)**, E42-E44, (2001).

14. Zeng, A.; Liu, E.; Tan, S. N.; Zhang, S.; Gao, J., *Stripping voltammetric analysis of heavy metals at nitrogen doped diamond-like carbon film electrodes*, Electroanalysis, **14 (18)**, 1294-1298, (2002).

15. Zeng, A.; Liu, E.; Tan, S. N.; Zhang, S.; Gao, J., *Cyclic voltammetry studies of sputtered nitrogen doped diamond-like carbon film electrodes*, Electroanalysis, **14 (15-16)**, 1110-1115, (2002).

16. Lagrini, A.; Deslouis, C.; Cachet, H.; Benlahsen, M.; Charvet, S., *Elaboration and electrochemical characterization of nitrogenated amorphous carbon films*, Electrochem. Commun., **6 (3)**, 245-248, (2004).

17. Lagrini, A.; Charvet, S.; Benlahsen, M.; Debiemme-Chouvy, C.; Deslouis, C.; Cachet, H., *Microstructure and electronic investigations of carbon nitride films deposited by RF magnetron sputtering*, Thin Solid Films, **482 (1-2)**, 41-44, (2005).

18. Pleskov, Y. V.; Krotova, M. D.; Polyakov, V. I.; Khomich, A. V.; Rukovishnikov, A. I.; Druz, B. L.; Zaritskiy, I., *Electrochemical behaviour of a-C:N:H films*, J. Electroanal. Chem., **519 (1-2)**, 60-64, (2002).

19. Pleskov, Y. V.; Krotova, M. D.; Polyakov, V. I.; Khomich, A. V.; Rukovishnikov, A. I.; Druz, B. L.; Zaritskiy, I. In *Electrical and electrochemical properties of a-C:N:H films*, Materials Research Society Symposium Proceedings, 2000; pp 439-444.

20. Adamopoulos, G.; Godet, C.; Deslouis, C.; Cachet, H.; Lagrini, A.; Saidani, B., *The electrochemical reactivity of amorphous hydrogenated carbon nitrides for*

varying nitrogen contents: the role of the substrate, Diamond Relat. Mater., **12 (3-7)**, 613-617, (2003).

21. Cachet, H.; Deslouis, C.; Chouiki, M.; Saidani, B.; Conway, N. M. J.; Godet, C., *Electrochemistry of Nitrogen-Incorporated Hydrogenated Amorphous Carbon Films*, J. Electrochem. Soc., **149 (7)**, E233-E241, (2002).

22. Lackner, J. M., *Industrially-scaled large-area and high-rate tribological coating by Pulsed Laser Deposition*, Surf. Coat. Technol., **200 (5-6)**, 1439-1444, (2005).

23. Robertson, J., *Electronic and atomic structure of diamond-like carbon*, Semicond. Sci. Technol., **18 (3)**, S12-S19, (2003).

24. Rudolph, M., *Digital simulations on unequally spaced grids. Part 2. Using the box method by discretization on a transformed equally spaced grid*, J. Electroanal. Chem., **543 (1)**, 23-39, (2003).

25. Rudolph, M., *Digital simulations on unequally spaced grids. Part 3. Attaining exponential convergence for the discretisation error of the flux as a new strategy in digital simulations of electrochemical experiments*, J. Electroanal. Chem., **571 (2)**, 289-307, (2004).

26. Rudolph, M. http://www.digielch.de (October 15, 2006).

27. Briggs, D.; Seah, M. P.; Editors, *Practical Surface Analysis by Auger and X-ray Photoelectron Spectroscopy*. 1983; p 533 pp.

28. Pleskov, Y. V.; Evstefeeva, Y. E.; Baranov, A. M., *Amorphous diamond-like carbon electrodes: the catalytic effect of platinum admixture*, Russ. J. Electrochem., **37 (6)**, 644-646, (2001).

29. Bennett, J. A.; Wang, J.; Show, Y.; Swain, G. M., *Effect of sp2-Bonded Nondiamond Carbon Impurity on the Response of Boron-Doped Polycrystalline Diamond Thin-Film Electrodes*, J. Electrochem. Soc., **151 (9)**, E306-E313, (2004).

30. Diaz, J.; Paolicelli, G.; Ferrer, S.; Comin, F., *Separation of the sp3 and sp2 components in the C1s photoemission spectra of amorphous carbon films*, Phys. Rev. B: Condens. Matter, **54 (11)**, 8064-8069, (1996).

31. Haerle, R.; Riedo, E.; Pasquarello, A.; Baldereschi, A., *sp2/sp3 Hybridization ratio in amorphous carbon from C 1s core-level shifts: X-ray photoelectron spectroscopy and first-principles calculation*, Phys. Rev. B: Condens. Matter Mater. Phys., **65 (4)**, 045101/045101-045101/045109, (2002).

32. Voevodin, A. A.; Donley, M. S., *Preparation of amorphous diamond-like carbon by pulsed laser deposition: a critical review*, Surf. Coat. Technol., **82 (3)**, 199-213, (1996).

33. Song, H.; Ilegbusi, O. J., *Analysis of X-ray photoelectron spectra of amorphous carbon nitride films*, Thin Solid Films, **388 (1,2)**, 114-119, (2001).

34. Tabbal, M.; Merel, P.; Moisa, S.; Chaker, M.; Ricard, A.; Moisan, M., *X-ray photoelectron spectroscopy of carbon nitride films deposited by graphite laser ablation in a nitrogen postdischarge*, Appl. Phys. Lett., **69 (12)**, 1698-1700, (1996).

35. Zheng, W. T.; Cao, P. J.; Li, J. J.; Wang, X.; Jin, Z. S., *Chemical bonding of CNx films synthesized by nitrogen ion implantation into diamond and graphite*, Surf. Coat. Technol., **173 (2-3)**, 213-218, (2003).

36. Wu, Z.; Yu, Y.; Liu, X., *Characteristics of carbon nitride films synthesized by single-source ion beam enhanced deposition system*, Appl. Phys. Lett., **68 (9)**, 1291-1293, (1996).

37. Zhang, W.; Xia, Y.; Ju, J.; Wang, L.; Fang, Z.; Zhang, M., *Electrical conductivity of carbon nitride films with different nitrogen content*, Solid State Commun., **126**, 163-166, (2003).

38. Jiang, L.; Fitzgerald, A. G.; Rose, M. J.; Cheung, R.; Rong, B.; van der Drift, E., *X-ray photoelectron spectroscopy studies of the effects of plasma etching on amorphous carbon nitride films*, Appl. Surf. Sci., **193 (1-4)**, 144-148, (2002).

39. Rusop, M.; Soga, T.; Jimbo, T., *X-ray photoelectron spectroscopy studies on the bonding properties of amorphous carbon nitride films synthesized by pulsed laser deposition with different substrate temperatures*, Surf. Rev. Lett., **12 (2)**, 185-195, (2005).

40. Zheng, W. T.; Sjoestroem, H.; Ivanov, I.; Xing, K. Z.; Broitman, E.; Salaneck, W. R.; Greene, J. E.; Sundgren, J. E., *Reactive magnetron sputter deposited CNx: effects of N2 pressure and growth temperature on film composition, bonding, and microstructure*, J. Vac. Sci. Technol., A, **14 (5)**, 2696-2701, (1996).

41. Ripalda, J. M.; Montero, I.; Galan, L., *An XPS study of carbon nitride synthesized by ion beam nitridation of C60 fullerene*, Diamond Relat. Mater., **7 (2-5)**, 402-406, (1998).

42. Andujar, J. L.; Pino, F. J.; Polo, M. C.; Bertran, E., *Carbon nitride thin films deposited from coupled r.f. magnetron sputtering and ion beam-assisted processes*, Diamond Relat. Mater., **10 (3-7)**, 1175-1178, (2001).

43. Xu, W.; Fujimoto, T.; Wang, L.; Ohchi, T.; Kojima, I., *What happens in the annealing of carbon nitride thin films?*, J. Vac. Sci. Technol., B: Microelectron. Nanometer Struct.--Process., Meas., Phenom., **22 (1)**, 6-11, (2004).

44. Voevodin, A. A.; Jones, J. G.; Zabinski, J. S.; Czigany, Z.; Hultman, L., *Growth and structure of fullerene-like CNx thin films produced by pulsed laser ablation of graphite in nitrogen*, J. Appl. Phys., **92 (9)**, 4980-4988, (2002).

45. Ferrari, A. C., *Determination of bonding in diamond-like carbon by Raman spectroscopy*, Diamond Relat. Mater., **11 (3-6)**, 1053-1061, (2002).

46. Ferrari, A. C.; Robertson, J., *Raman spectroscopy of amorphous, nanostructured, diamond-like carbon, and nanodiamond*, Philos. Trans. R. Soc. London, A, **362 (1824)**, 2477-2512, (2004).

47. Robertson, J., *Amorphous carbon*, Adv. Phys., **35 (4)**, 317-374, (1986).

48. Tuinstra, F.; Koenig, J. L., *Raman spectrum of graphite*, J. Chem. Phys., **53 (3)**, 1126-1130, (1970).

49. Ferrari, A. C.; Rodil, S. E.; Robertson, J., *Interpretation of infrared and Raman spectra of amorphous carbon nitrides*, Phys. Rev. B: Condens. Matter Mater. Phys., **67 (15)**, 155306/155301-155306/155320, (2003).

50. Victoria, N. M.; Hammer, P.; dos Santos, M. C.; Alvarez, F., *Vibrational analysis of amorphous carbon-nitrogen alloys by 15N and D isotopic substitution*, Phys. Rev. B: Condens. Matter Mater. Phys., **61 (2)**, 1083-1087, (2000).

51. Lazar, G.; Zellama, K.; Vascan, I.; Stamate, M.; Lazar, I.; Rusu, I., *Infrared absorption properties of amorphous carbon films*, Journal of Optoelectronics and Advanced Materials, **7 (2)**, 647-652, (2005).

52. Veerasamy, V. S.; Yuan, J.; Amaratunga, G. A. J.; Milne, W. I.; Gilkes, K. W. R.; Weiler, M.; Brown, L. M., *Nitrogen doping of highly tetrahedral amorphous carbon*, Phys. Rev. B: Condens. Matter Mater. Phys., **48 (24)**, 17954-17959, (1993).

53. Tabbal, M.; Christidis, T.; Isber, S.; El Khakani, M. A.; Merel, P.; Chaker, M., *Graphitic nanoclustering in pulsed laser deposited diamond-like-carbon and carbon nitride thin films*, Thin Solid Films, **453-454**, 234-238, (2004).

54. Shin, I. H.; Lee, T. D., *Effect of nitrogen doping on field emission characteristics of patterned diamond-like carbon films prepared by pulsed laser deposition*, Journal of Vacuum Science & Technology, B: Microelectronics and Nanometer Structures, **18 (2)**, 1027-1030, (2000).

55. Bard, A. J.; Faulkner, L. R., *Electrochemical Methods: Fundamentals and Application*. 2nd ed.; John Wiley & Sons, Inc.: New York, 2001.

56. Marken, F.; Eklund, J. C.; Compton, R. G., *Voltammetry in the presence of ultrasound: can ultrasound modify heterogeneous electron transfer kinetics?*, J. Electroanal. Chem., **395 (1-2)**, 335-338, (1995).

57. Benlahsen, M.; Cachet, H.; Charvet, S.; Debiemme-Chouvy, C.; Deslouis, C.; Lagrini, A.; Vivier, V., *Improvement and characterization of the electrochemical reactivity of amorphous carbon nitride electrodes*, Electrochem. Commun., **7 (5)**, 496-499, (2005).

58. Cachet, H.; Debiemme-Chouvy, C.; Deslouis, C.; Lagrini, A.; Vivier, V., *Correlation between electrochemical reactivity and surface chemistry of amorphous carbon nitride films*, Surf. Interface Anal., **38 (4)**, 719-722, (2006).

59. Bard, A. J.; Editor, *Electroanalytical Chemistry*. 1991; Vol. 17, p 393.

60. Chen, P.; McCreery, R. L., *Control of electron transfer kinetics at glassy carbon electrodes by specific surface modification*, Anal. Chem., **68 (22)**, 3958-3965, (1996).

61. Zhou, J.; Wipf, D. O., *UV/ozone pretreatment of glassy carbon electrodes*, J. Electroanal. Chem., **499 (1)**, 121-128, (2001).

62. Kuo, T.-C.; McCreery, R. L., *Surface Chemistry and Electron-Transfer Kinetics of Hydrogen-Modified Glassy Carbon Electrodes*, Anal. Chem., **71 (8)**, 1553-1560, (1999).

63. Chen, Q.; Swain, G. M., *Structural Characterization, Electrochemical Reactivity, and Response Stability of Hydrogenated Glassy Carbon Electrodes*, Langmuir, **14 (24)**, 7017-7026, (1998).

64. Fagan, D. T.; Hu, I. F.; Kuwana, T., *Vacuum heat-treatment for activation of glassy carbon electrodes*, Anal. Chem., **57 (14)**, 2759-2763, (1985).

65. Salazar-Banda, G. R.; Andrade, L. S.; Nascente, P. A. P.; Pizani, P. S.; Rocha-Filho, R. C.; Avaca, L. A., *On the changing electrochemical behaviour of boron-doped diamond surfaces with time after cathodic pre-treatments*, Electrochim. Acta, **51 (22)**, 4612-4619, (2006).

66. Kahn, M.; Menegazzo, N.; Mizaikoff, B.; Berghauser, R.; Lackner, J. M.; Hufnagel, D.; Waldhauser, W. In *Properties of DLC and Nitrogen-doped DLC Films Deposited by DC Magnetron Sputtering*, Tenth International Conference on Plasma Surface Engineering, Garmisch (Germany), September 10-15, 2006.

67. Simon, N.; Girard, H.; Ballutaud, D.; Ghodbane, S.; Deneuville, A.; Herlem, M.; Etcheberry, A., *Effect of H and O termination on the charge transfer of moderately boron doped diamond electrodes*, Diamond Relat. Mater., **14 (3-7)**, 1179-1182, (2005).

68. Ilangovan, G.; Pillai, K. C., *Mechanism of activation of glassy carbon electrodes by cathodic pretreatment*, J. Solid State Electrochem., **3 (6)**, 357-360, (1999).

69. Sundberg, K. M.; Smyrl, W. H.; Atanasoska, L.; Atanasoski, R., *Surface modification and oxygen reduction on glassy carbon in chloride media*, J. Electrochem. Soc., **136 (2)**, 434-439, (1989).

70. Poon, M.; McCreery, R. L., *In situ laser activation of glassy carbon electrodes*, Anal. Chem., **58 (13)**, 2745-2750, (1986).

71. Stutts, K. J.; Kovach, P. M.; Kuhr, W. G.; Wightman, R. M., *Enhanced electrochemical reversibility at heat-treated glassy carbon electrodes*, Anal. Chem., **55 (9)**, 1632-1634, (1983).

72. Ilangovan, G.; Pillai, K. C., *Electrochemical and XPS Characterization of Glassy Carbon Electrode Surface Effects on the Preparation of a Monomeric Molybdate(VI)-Modified Electrode*, Langmuir, **13 (3)**, 566-575, (1997).

73. Martin, H. B.; Morrison, P. W., Jr., *Application of a diamond thin film as a transparent electrode for in situ infrared spectroelectrochemistry*, Electrochem. Solid-State Lett., **4 (4)**, E17-E20, (2001).

74. Dekanski, A.; Stevanovic, J.; Stevanovic, R.; Nikolic, B. Z.; Jovanovic, V. M., *Glassy carbon electrodes. I. Characterization and electrochemical activation*, Carbon, **39 (8)**, 1195-1205, (2001).

75. Engstrom, R. C.; Strasser, V. A., *Characterization of electrochemically pretreated glassy carbon electrodes*, Anal. Chem., **56 (2)**, 136-141, (1984).

76. Hupert, M.; Muck, A.; Wang, J.; Stotter, J.; Cvackova, Z.; Haymond, S.; Show, Y.; Swain, G. M., *Conductive diamond thin-films in electrochemistry*, Diamond Relat. Mater., **12 (10-11)**, 1940-1949, (2003).

77. Chen, Q.; Gruen, D. M.; Krauss, A. R.; Corrigan, T. D.; Witek, M.; Swain, G. M., *The structure and electrochemical behavior of nitrogen-containing nanocrystalline diamond films deposited from CH4/N2/Ar mixtures*, J. Electrochem. Soc., **148 (1)**, E44-E51, (2001).

78. Chen, P.; Fryling, M. A.; McCreery, R. L., *Electron Transfer Kinetics at Modified Carbon Electrode Surfaces: The Role of Specific Surface Sites*, Anal. Chem., **67 (18)**, 3115-3122, (1995).

79. Nicholson, R. S., *Theory and application of cyclic voltammetry for measurement of electrode reaction kinetics*, Anal. Chem., **37 (11)**, 1351-1355, (1965).

80. Yang, H.-H.; McCreery, R. L., *Elucidation of the mechanism of dioxygen reduction on metal-free carbon electrodes*, J. Electrochem. Soc., **147 (9)**, 3420-3428, (2000).

81. Martin, H. B.; Argoitia, A.; Landau, U.; Anderson, A. B.; Angus, J. C., *Hydrogen and oxygen evolution on boron-doped diamond electrodes*, J. Electrochem. Soc., **143 (6)**, L133-L136, (1996).

82. Beck, F.; Krohn, H.; Kaiser, W.; Fryda, M.; Klages, C. P.; Schafer, L., *Boron doped diamond/titanium composite electrodes for electrochemical gas generation from aqueous electrolytes*, Electrochim. Acta, **44 (2-3)**, 525-532, (1998).

83. Nagaoka, T.; Yoshino, T., *Surface properties of electrochemically pretreated glassy carbon*, Anal. Chem., **58 (6)**, 1037-1042, (1986).

84. Swain, G. M., *Electrically Conducting Diamond Thin Films: Advanced Electrode Materials for Electrochemical Technologies*. Marcel Dekker, Inc.: New York, 2004; Vol. 22, p 181-277.

85. Harrick, N. J., *Internal Reflection Spectroscopy*. 1967; p 327 pp.

86. Klinger, L.; Glickman, E.; Katsman, A.; Levin, L., *Time dependence of stress and hillock distributions during electromigration in thin metal film interconnections*, Materials Science & Engineering, B: Solid-State Materials for Advanced Technology, **B23 (1)**, 15-18, (1994).

87. Popovich, N. D.; Wong, S.-S.; Yen, B. K. H.; Yeom, H.-Y.; Paine, D. C., *Influence of Microstructure on the Electrochemical Performance of Tin-Doped Indium Oxide Film Electrodes*, Anal. Chem., **74 (13)**, 3127-3133, (2002).

4 CHARACTERIZATION OF NOBLE METAL-DIAMONDLIKE CARBON NANOCOMPOSITE MATERIALS

The physical, spectroscopic, and electrochemical properties of gold- and platinum-diamondlike carbon (DLC) nanocomposite materials will be presented in this chapter, along with initial efforts towards coating of mid-IR waveguides with these nanocomposite materials for spectroelectrochemical analysis.

4.1 Motivation

Besides doping with nitrogen, the electrical conductivity of diamondlike carbon can also be improved by the introduction of metal nanoclusters.[1] In contrast to N-DLC, metal-DLC layers do not give rise to additional absorption bands in the IR spectrum. Therefore, extending upon the work presented in *Chapter 3*, metal-DLC layers containing gold and platinum nanoclusters have been investigated for their suitability towards mid-IR ATR spectroelectrochemical platforms.

4.1.1 Metal-diamondlike carbon (DLC) nanocomposites

The conductivity of non-doped DLC is governed by the fraction of sp^2-hybridized carbon present in the layer (*Section 2.2.2*). Therefore, DLC layers with a high fraction of sp^3-hybridized carbon atoms are inherently insulating, and hence, not suitable for electrochemical analysis. Electronic conduction in DLC layers can be increased by adding dopants such as nitrogen[2] or phosphorous.[3] A detailed review on doped DLC electrodes is presented in *Chapter 3*.

Alternatively, the inclusion of metal nanoclusters during DLC deposition has also shown to increase the conductivity of DLC thin films.[1] These films are commonly referred to as "metal-doped" DLC films [4-8] even though the presence of the metal does not increase the free carrier concentration of the DLC matrix as would be expected from "true" dopants. Therefore, the terminology "nanocomposite" is more appropriate and will be used throughout this thesis to provide a clear distinction between the metal-DLC nanocomposite electrodes presented in this chapter, and the nitrogen-doped DLC layers discussed in *Chapter 3*.

The incorporation of metals into DLC layers was originally pursued due to the improved tribological properties of nanocomposite layers vs. metal-free DLC.[9-11] However, the electrochemical properties of metal-DLC nanocomposites have only rarely been addressed in literature, due to their less favorable characteristics compared to BDD. Results published by Sunkara et al.[12] on chromium- and hafnium-DLC nanocomposite electrodes have shown slow electrode kinetics (~ 10^{-5} cm/s) for both $Fe(CN)_6^{3-/4-}$ and $Ru(NH_3)_6^{3+/2+}$ redox couples. Unfortunately, no compositional information on these layers was provided by the authors. Hence, unambiguous conclusions regarding the electrochemical activity cannot be derived from these studies.

Pleskov et al. described the electrochemical properties of platinum-DLC nanocomposite films via cyclic voltammetry using nanocomposite electrodes with up to 12 % platinum content. The authors report a peak separation between anodic and cathodic peak of at least 360 mV for the $Fe(CN)_6^{3-/4-}$ couple,[13] however, the scan rate was not reported. Hence, the prediction of the heterogeneous electron transfer rate is not possible from these reports. Although the authors did not discuss the influence of the DLC matrix on

the electrochemical properties, it is likely that the mediocre electronic conduction observed resulted from the inclusion of hydrogen in the DLC layer (see also *Section 2.2.3*).

Since metal-DLC layers were originally developed for mechanically demanding environments, extensive evaluation of the infrared spectroscopic properties of these nanocomposite materials has not yet been performed.[14] However, since neither of the metals used in this study covalently bond to the DLC matrix, these metal-DLC layers are anticipated to exhibit infrared spectra similar to those of metal-free DLC, which may provide suitable nanocomposite electrode materials for mid-infrared ATR spectroelectrochemistry.

4.2 Experimental

4.2.1 Pulsed laser deposition system

Metal-DLC nanocomposite materials were jointly developed with the research group headed by Dr. Narayan at the University of North Carolina (UNC) at Chapel Hill. Depositions were performed by the collaborators in a stainless steel high vacuum chamber, which was maintained at a pressure of $\sim 5 \times 10^{-6}$ Torr during film deposition (*Figure 2.4(a)*). A Compex 205 KrF excimer laser (Coherent Inc., Fort Lauderdale, FL) operating at $\lambda = 248$ nm was used for target ablation. The laser was operated with a pulse duration of 25 ns and a frequency of 10 Hz. The output of ~ 200 mJ and a spot size of ~ 0.05 cm^2 provided an energy density of $\sim 4 - 5$ J/cm^2. The target-to-substrate distance was maintained at 4.5 cm. The total time for each deposition was 10 min resulting in the film thicknesses depicted in *Table 4.1*.

Table 4.1: Thickness of the metal-DLC nanocomposite layers determined by stylus profilometry.

Sample	Thickness (nm)
Pure DLC	50
Au #1	105
Au #2	67
Au #3	63
Pt #1	58
Pt #2	38
Pt #3	50

A high purity 4 cm diameter graphite pellet (99.999 %, Alfa Aesar, Ward Hill, MA) was used as the target for pulsed laser deposition of DLC thin films on silicon. The metal-DLC films were prepared by partially covering the graphite pellet surface with a segment of gold or platinum (*Figure 2.4(b)*). The target was rotated at a speed of 5 rpm, and the focused laser beam sequentially ablated graphite and metal portions of the multicomponent target.

4.2.2 Physical characterization

In addition to the characterization techniques presented in *Section 3.2.2*, the metal-DLC layers were analyzed using Rutherford backscattering spectroscopy (RBS), transmission electron microscopy (TEM) and atomic force microscopy (AFM) to evaluate the influence of metal on the DLC matrix.

Rutherford backscattering spectroscopy (RBS) data were collected with a 1.7 MV Tandetron particle accelerator (General Ionex, Newburyport, MA) using a 2.25 MeV

He^{2+} ion beam. The detector was mounted for a backscatter angle of 165 º. The sample was inclined 5 º towards the detector, and was randomly rotated 1 º in both the x- and y-planes avoiding ion channeling. The diameter of the beam spot size was 1.5 mm. Spectral simulations were performed with the RUMP software package (Genplot, Cortland, OH).

Cross-sectional Z-contrast images of the diamondlike carbon-metal composite films were obtained using a 2010 F scanning transmission electron microscope (JEOL, Tokyo, Japan) equipped with Gatan Image Filter attachment. In this TEM/STEM system, a 1.6 Å probe is scanned across the sample. A high angle annular detector collects electrons that are scattered at large angles (75-150 mrad). Contrast is proportional to the atomic number (Z) squared.

A PicoPlus **atomic force microscope** (Molecular Imaging, Phoenix, AZ) equipped with a 10 × 10 μm range multipurpose scanner was used to record the surface topography of metal-free and metal-DLC films in air. The atomic force microscopy studies were performed in contact mode with silicon probes (MikroMasch, Wilsonville, OR) providing a nominal tip curvature of < 10 nm. The obtained AFM images were processed using the Scanning Probe Image Processor (SPIP) software package (Image Metrology, Lyngby, Denmark).

Scanning electron microscopy (SEM) pictures were obtained with an FEI Nova Nanolab 200 systems equipped with a field emission detector.

The **X-ray photoelectron spectroscopy** (XPS) data were acquired with parameters equal to those presented in *Section 3.2.2*. High resolution spectra were recorded for the carbon 1s singlet, gold 4f, and platinum 4f doublet peaks for quantification of each constituent. In-situ etching for XPS depth profiling was achieved using an argon ion gun

(Nonsequitur Technologies, Inc., Bend, OR). Argon ions accelerated at 5 kV resulted in a current density of 12.8 mA/cm^2 and an etching rate of approximately 0.9 nm/s.

For the **spectroelectrochemical studies**, platinum- and gold-diamondlike carbon nanocomposite films were deposited onto 5.0 cm x 2.0 cm x 2.0 mm trapezoidal ATR germanium waveguides (MacroOptica, Moscow, Russia). The modified germanium waveguides were masked to expose a 4 cm^2 area at the center of the crystal. Deposition parameters for the platinum-DLC and gold-DLC films studied in these experiments are listed in *Table 4.2* under Pt #1 and Au #2, respectively. The cell shown in *Figure 3.1* was used for the experiments described in this chapter.

Raman spectra were acquired with a Renishaw 2000 spectrometer using the 514.5 nm line of an argon ion laser.

4.2.3 Electrochemical characterization

The electrochemical characterization was performed using the same setup described in *Section 3.2.3*. In addition, 3 mm glassy carbon, 1 mm platinum, and 1 mm gold disk electrodes were used for comparison of the working potential window for metal-DLC in 0.5 M H_2SO_4.

4.3 Results

The error bars presented within this chapter reflect the variance ($\pm 1\sigma$) observed in a single representative sample for each metal type and content. An exception lies in the data collected by Rutherford backscattering spectroscopy: Since $n = 1$, the error bars correspond to 10 % instrumental error estimated by the operator at the facilities where the measurements were performed (AMPAC/UCF in Orlando, FL)

4.3.1 Rutherford backscattering spectroscopy

Elemental information obtained by Rutherford backscattering spectroscopy (RBS) is especially useful for samples whose composition along the vertical axis may not be ideally uniform. As described in *Section 3.2.1*, the nanocomposite layers presented in this study are deposited by the sequential ablation of the metal-modified graphite target. Depending upon the deposition conditions (e.g. target rotation speed, pulse frequency, and amount of metal masking the underlying graphite), a layered structure consisting of alternating DLC and metal nanoclusters may be obtained.[15] Additionally, the ablation of the metal modifier increases the roughness of the target leading to a decreased deposition rate.[16, 17] The roughness increases with the number of pulses, resulting in a gradient metal concentration within the deposited film. RBS is insensitive to the chemical properties of the sample, matrix effects, and sample morphology rendering it ideal for quantification of the bulk metal.[18] *Table 4.2* summarizes the differences in elemental composition of the DLC nanocomposite layers with target composition.

Table 4.2: Metal content in the DLC nanocomposite layers determined by RBS

Sample	Target composition (percent metal)	Metal concentration in layer
Au #1	50 %	36.0 %
Au #2	25 %	11.0 %
Au #3	10 %	3.0 %
Pt #1	50 %	11.5 %
Pt #2	30 %	5.7 %
Pt #3	25 %	4.0 %

In order to examine if any discrepancies in metal content between the surface and bulk of the layer exist, X-ray photoelectron spectroscopy (XPS) was applied in addition to RBS for compositional analysis. A comparison of the data derived is shown in *Figure 4.1*:

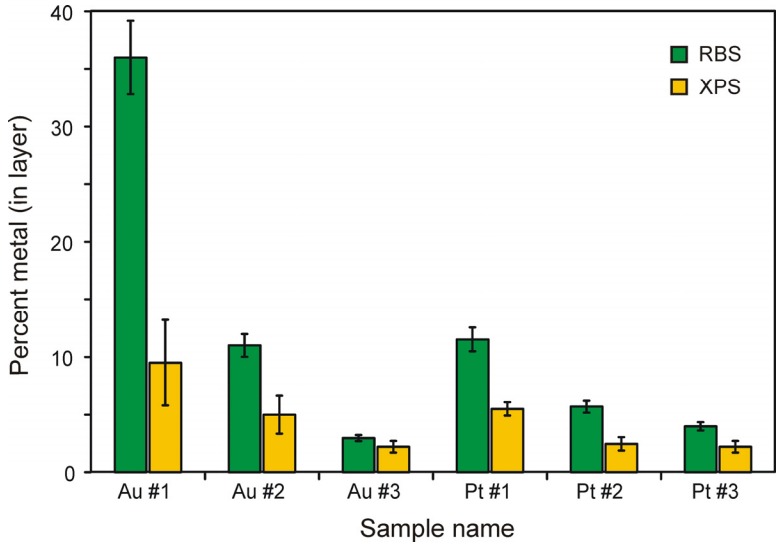

Figure 4.1: Comparison of the metal content in the nanocomposite layers obtained from RBS and XPS (n = 4)compositional analysis.

As shown in *Figure 4.1*, the results obtained with the two different spectroscopic techniques vary significantly, especially for the layers containing the highest amount of metal. As previously mentioned, the repeated ablation of the metal target results in a decreased deposition rate. Therefore, the lower metal content measured at the surface (via XPS) compared to the bulk (via RBS) is consistent with the lower deposition rate of the progressively rougher target. The discrepancy between the two techniques at layers with lower metal content is significantly smaller, indicating that the metal deposition rate is consistent throughout the deposition.

4.3.2 X-ray photoelectron spectroscopy studies

Superficial composition in metal-DLC is derived from the ratio of the integrated peak areas adjusted with the proper sensitivity factors for each element detected (*Figure 4.2(a)*). General survey spectra of the DLC layers show that only carbon, adventitious oxygen and the metal modifier (for metal-DLC nanocomposites) are present in measurable quantities. High resolution spectra of the 4f peaks for the corresponding modifier (*Figure 4.2(b)* and *(c)*) shows that the metal is included in its metallic (zero-valent) form.

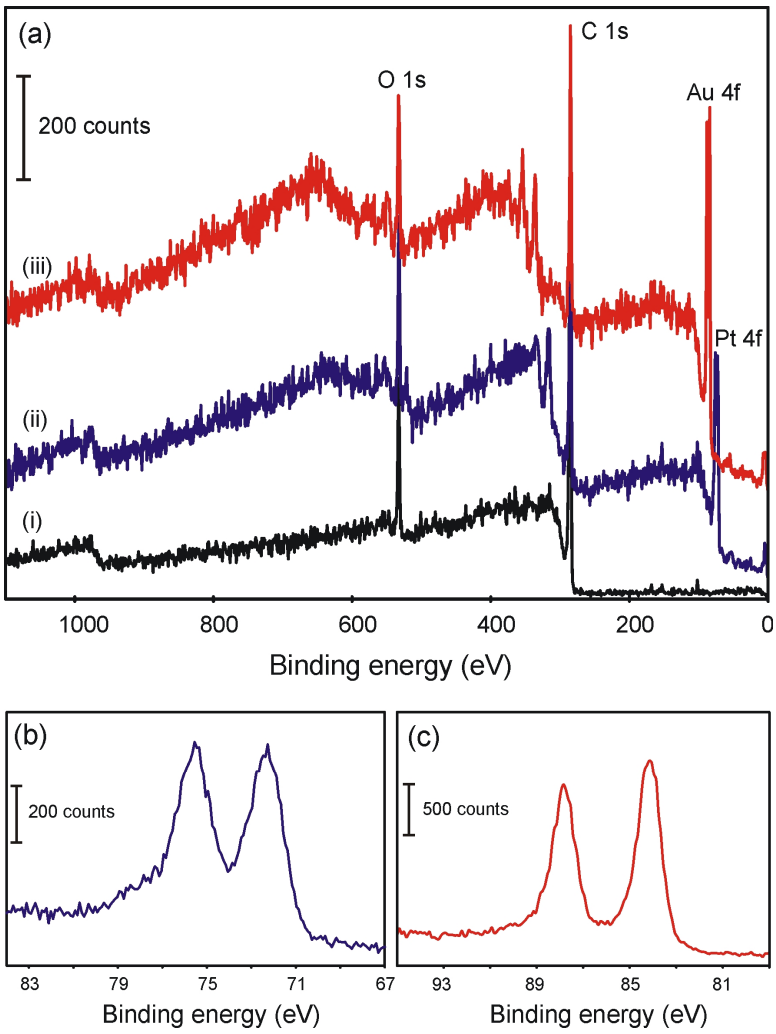

Figure 4.2: (a) General survey spectra of (i) DLC, (ii) Pt-DLC (Pt #1) and (iii) Au-DLC (Au #1) and high resolution spectra of (b) Pt 4f in Pt-DLC, and (c) Au 4f in Au-DLC obtained by XPS.

Furthermore, as was discussed in *Section 3.3.1*, the hybridization state of carbon is determined from the mathematical deconvolution of the 1s photoemission peak into the presumed constituents. Exemplary deconvolution of the carbon 1s peak into sp^2- and sp^3-hybridized carbon in metal-free DLC is shown in *Figure 4.3*.

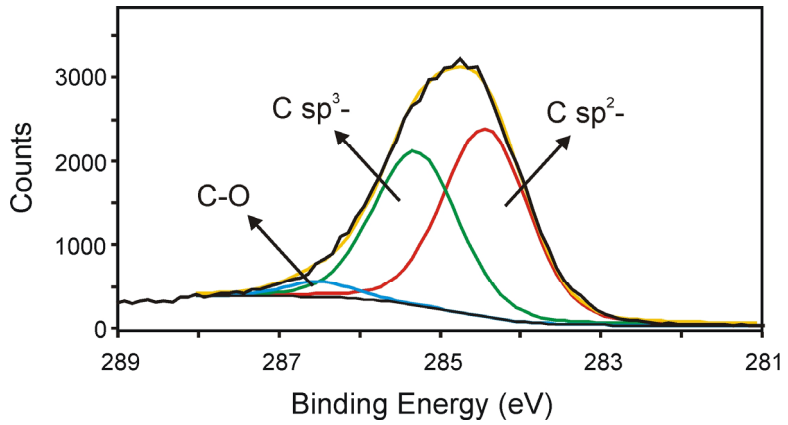

Figure 4.3: XPS spectrum of the C 1s peak of the metal-free DLC film and the deconvolution of the measured cumulative peak into sp^2-, sp^3-, and CO contributions.

The presence of sp^2-hybridized carbon will affect the conductivity of DLC layers (see also *Section 2.2.3*), therefore, quantification of surface sp^2-carbon is necessary in order to assess the contribution to the observed electrochemical properties.[19, 20] The deconvoluted carbon 1s spectra for metal-free DLC films reveal a surface composition of approx. 46 % sp^3-hybridized carbon atoms. The presence of metal in the nanocomposite films does not seem to substantially affect the surface sp^3-hybridized carbon content (see *Table 3.2*).

Table 4.3: Compositional analysis of the metal-DLC nanocomposite layers presented in this study.

Sample	Metal concentration	Percentage of sp^3-hybridized atoms (n = 4)	Oxygen/carbon ratio (n = 4)
DLC	0 %	46 ± 2 %	0.11 ± 0.01
Au #1	36.0 %	41 ± 11 %	0.18 ± 0.03
Au #2	11.0 %	38 ± 2 %	0.16 ± 0.03
Au #3	3.0 %	42 ± 6 %	0.15 ± 0.03
Pt #1	11.5 %	38 ± 4 %	0.18 ± 0.01
Pt #2	5.7 %	39 ± 12 %	0.16 ± 0.04
Pt #3	4.0 %	40 ± 8 %	0.17 ± 0.01

Generally, the incorporation of metal induces a decreased sp^3-fraction due to stress reduction via the formation of thin graphitic (sp^2-) "shells" around the metal clusters in the layers.[21] Hence, an increase in metal concentration should correspond to a decrease in sp^3-hybridized carbon atoms. However, the data obtained by XPS did not provide evidence of this correlation, thereby contrasting previously published data on ruthenium-[6] and chromium-DLC[4] films, showing the expected trend. This apparent discrepancy is related to the analytical method quantifying the fraction of sp^3-hybridized carbon atoms. Ruthenium- and chromium-DLC films were investigated with electron energy loss spectroscopy (EELS), which determines the average fraction of sp^3-hybridized carbon atoms over the entire thickness of an electron transparent region of the film. The surface of the DLC layers is additionally affected by collisions with incident species resulting in an increased apparent sp^2-content.[22, 23] Since XPS is highly selective to the surface composition, it is anticipated that the determined sp^2-carbon content will be affected by collisional damage as well as the metal content.

In addition, compositional analysis along the vertical axis was obtained by sputtering the surface with noble gas ions. However, information about the oxidation state of the elements is typically lost due to damage from the bombardment with the highly energetic noble gas ions.[24] Depth profiling of a platinum-DLC layer deposited onto a germanium ATR crystal is presented in *Section 3.3.5*.

4.3.3 Raman spectroscopic studies

The visible Raman spectrum of metal-free DLC layer shown in *Figure 4.4* is consistent with a layer containing a high fraction of sp^3-hybridized carbon. Upon incorporation of metal, the Raman spectra exhibits increased D-band intensities, suggesting that the metal-DLC nanocomposite films contain larger sp^2-hybridized carbon clusters than the metal-free diamondlike carbon film. Also, the position of the G-band in the metal-DLC films with higher metal concentrations indicates an increased clustering of sp^2-hybridized atoms.[25] Finally, the FWHM of the G-bands are reduced in films with higher metal concentrations as a result of lowered stresses within these films.[26] In contrast to XPS, Raman spectroscopy probes the hybridization states of carbon throughout the entire layer.[27] The changes spectral observed indicate that the bulk fraction of sp^2-hybridized carbon increases with the metal content, which is in agreement with reports on ruthenium- and chromium-DLC nanocomposites (see *Section 3.3.1*).[4, 6]

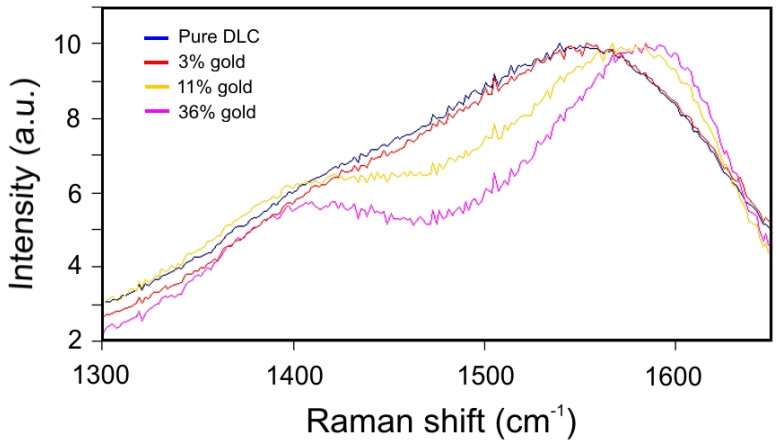

Figure 4.4: Raman spectra of gold-DLC nanocomposite layers with increasing metal content (data recorded in collaboration with Dr. Roger J. Narayan, UNC Chapel Hill).

4.3.4 Transmission electron, scanning electron and atomic force microscopy

Metals that do not bond covalently to a matrix frequently form self-assemblies of nearly spherical clusters within the matrix.[28, 29] The driving force for this clustering effect is the reduction in surface energy.[30] Low resolution cross-sectional transmission electron microscopic images of platinum-DLC show that the metal nanoclusters range in size from 3 to 7 nm (*Figure 4.5(a)*) These dimensions are in agreement with values reported in the literature.[15, 31, 32]

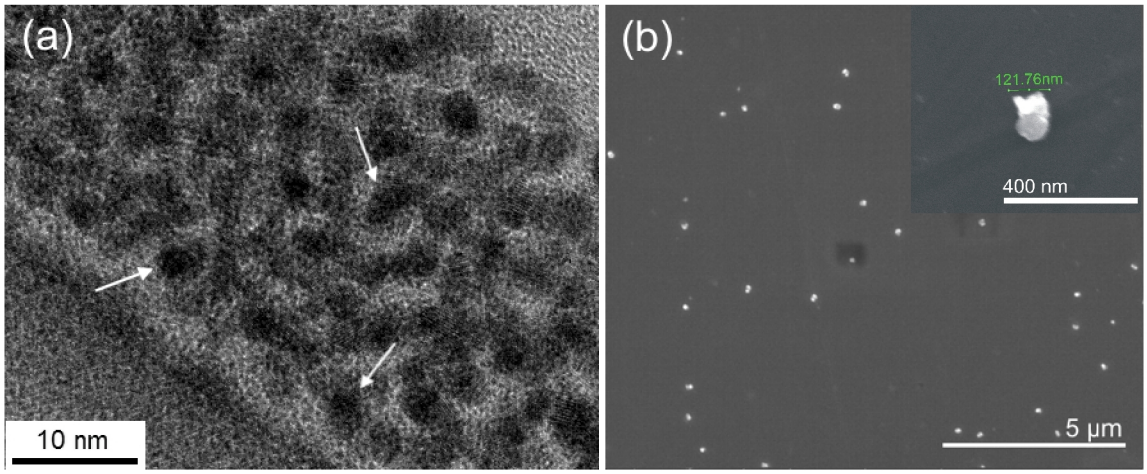

Figure 4.5: (a) Cross-sectional transmission electron microscopic image of a platinum-DLC layer. The white arrows mark platinum nanoclusters (data recorded in collaboration with Dr. Roger J. Narayan, UNC Chapel Hill). (b) Scanning electron microscopic image of the surface of a Pt-DLC layer. Inset in (b) shows a close-up image of surface particulates.

In contrast to the TEM results, the surface of metal-DLC layers are characterized by the presence of several large particulates with diameters of 200 – 300 nm (*Figure 4.5(b)*). Metal films deposited by PLD commonly show the presence of superficial features similar to those observed in the present study.[17] Surface particulates are attributed to a "splashing" mechanism occurring during pulsed laser deposition. Splashing occurs in materials via subsurface boiling, or shock wave ejection of particulates. As a result, the highly energetic plume originating from the ablated target may contain droplets of molten metal, which results in comparatively large features. The size of the formed droplets may be minimized by carefully repolishing the metal component of the target and by performing the deposition at higher laser fluences.[16, 33, 34]

Atomic force microscopy (AFM) images further confirms the presence of surface particulates, in addition to providing information about the height. A representative AFM image shows the particles are approximately disk shaped with heights of up to 30 nm

(*Figure 4.6(a)*). For comparison, the topographic image obtained at a metal-free DLC film (*Figure 4.6(b)*) is featureless indicating that DLC layers prepared by PLD display a very homogeneous surface.

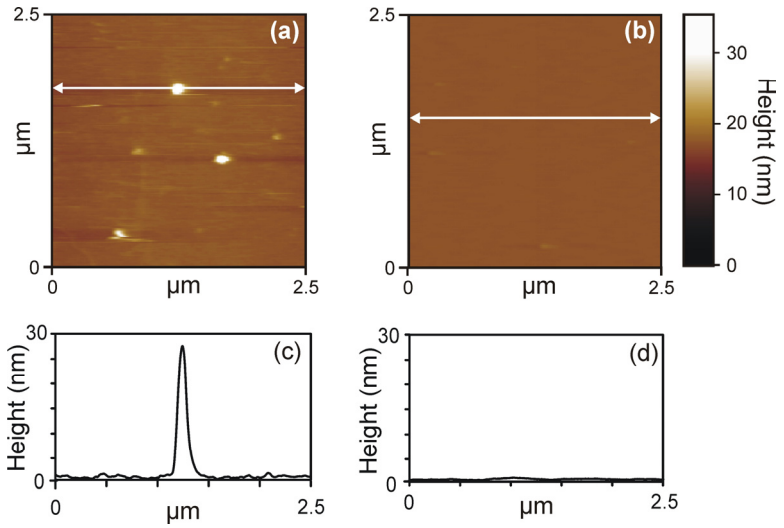

Figure 4.6: Atomic force microscopic images of (a) a gold-DLC layer (Au #1), and (b) a metal-free layer. Figures (c) and (d) show the corresponding height profiles along the white arrows in (a) and (b).

4.3.5 Mid-infrared spectroscopic studies

DLC thin films reveal transparency over a considerable mid-infrared spectral window.[35-37] Additionally, *Figure 4.7* indicates that all spectral features appear at the same magnitude for the metal-DLC coated mono-crystalline germanium attenuated total reflection (ATR) waveguides, as for a pristine Ge substrate. Gold-DLC coated ATR crystals transmit approximately 50 % of radiation of a pristine Ge waveguide, and despite the observed attenuation, sufficient radiation is transmitted through the crystal coated with platinum-DLC to enable spectroscopic analysis. Hence, metal-DLC nanocomposite

thin films have the potential to serve as transparent electrodes for spectroelectrochemical ATR analysis in the mid-infrared regime.

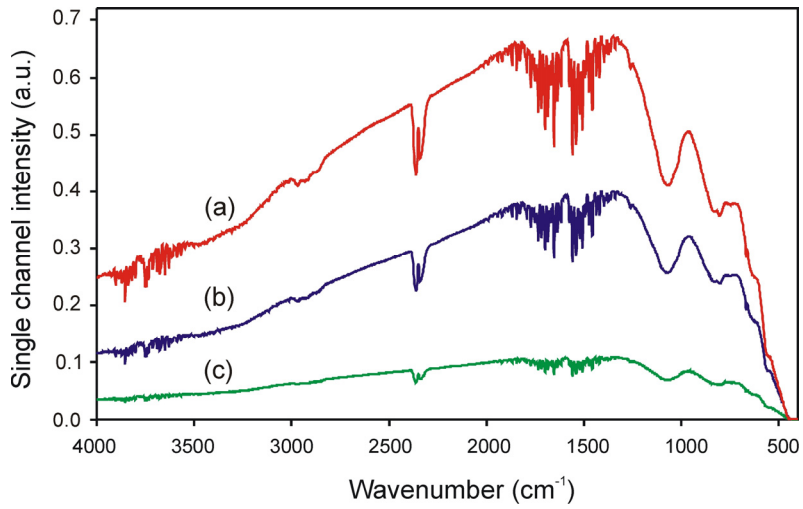

Figure 4.7: Single beam spectra of (a) a bare, (b) a gold-DLC coated, and (c) a platinum-DLC coated germanium crystal.

4.3.6 Electrochemical studies

Electronic conduction in DLC films containing metal clusters is not only dependent upon the type of metal, but also on its ability to react with the DLC matrix via the formation of carbide bonds.[1] In general, with increasing metal content the conductivity of the layers will accordingly increase approaching the behavior of the pure metal at very high concentrations (typically > 60 at. %).[1] The electron transfer mechanism in these nanocomposite films has yet to be fully elucidated, although Pleskov et al. hypothesized that electrons are shuttled via two distinct pathways: (1) homogeneously via a hopping mechanism through sp^2-hybridized carbon clusters, and (2) heterogeneously via the metal clusters, which serve as catalytic centers facilitating the electron transfer at the electrode|electrolyte interface.[8, 13]

The primary objective of the electrochemical study was to evaluate the performance of platinum- and gold-DLC thin films as electrode materials. Thus, initial experiments included determining the working potential window. The platinum-DLC films displayed a working potential window of 2.0 V while the gold-DLC films extends to 2.4 V (at ± 1mA/cm^2). In addition to sp^2-hybridized carbon, surfaces of metal-DLC nanocomposites display metal nanoclusters catalyzing H_2 evolution,[38] resulting in a lower potential window compared to N-DLC layers described in the literature[2, 39, 4] as well as those discussed in *Chapter 3*. Although the described effect may be disadvantageous from an electroanalytical viewpoint, the enhanced electrocatalytic activity measured at platinum-DLC surfaces is considered desirable for certain electrochemical systems, such as proton exchange membrane fuel cells.[41-43] For comparison *Figure 4.8* illustrates the working potential windows of metal-DLC electrodes, glassy carbon electrodes (entirely sp^2-hybridized), and the respective pristine metals. The metal-DLC electrodes provide a wider electrochemical window compared to the respective pristine metals, while offering the mechanical and chemical stability of an inert ceramic.

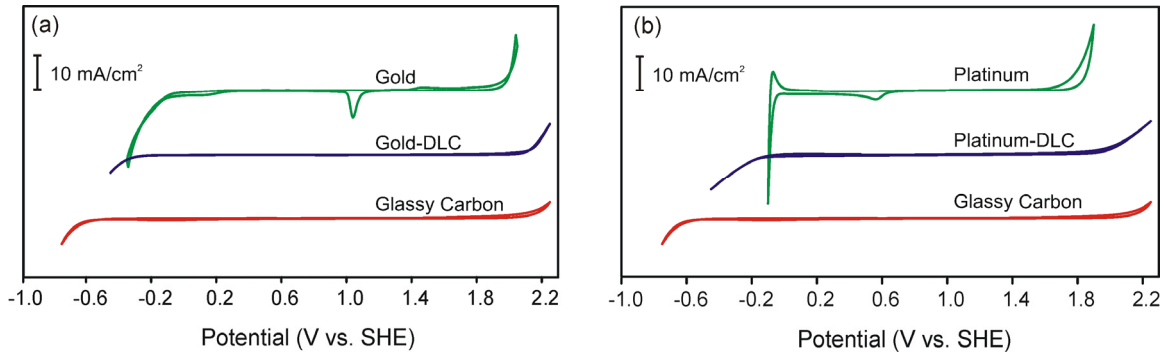

Figure 4.8: Working potential windows of (a) glassy carbon, gold, and gold-diamondlike carbon films, and (b) glassy carbon, platinum, and platinum-diamondlike carbon films in 0.5 M H_2SO_4 sparged with argon.

The following redox mediator couples, $Ru(NH_3)_6^{3+/2+}$ and $Fe(CN)_6^{3-/4-}$, were employed to determine the electrochemical behavior of metal-DLC electrodes. The peak separations (ΔE_p) measured at the different metal-DLC electrodes range from approximately 100 mV to 250 mV depending on the metal content (see *Table 3.3*).

Table 4.4: Peak separation of $Ru(NH_3)_6^{3+/2+}$ and $Fe(CN)_6^{3-/4-}$ redox species with respect to the metal concentration at 0.1 V/s (n = 3).

Sample	ΔE ($Ru(NH_3)_6^{3+/2+}$) (mV)	ΔE ($Fe(CN)_6^{3-/4-}$) (mV)
Au #1	104 ± 11	122 ± 5
Au #2	140 ± 14	159 ± 20
Au #3	164 ± 29	244 ± 25
Pt #1	124 ± 8	147 ± 6
Pt #2	172 ± 7	201 ± 14
Pt #3	179 ± 7	204 ± 40

Heterogeneous electron transfer rate constants (k_s) were extracted by a curve fitting process of the experimental CVs (*Section 3.2.3*) and are summarized in *Table 3.4*.

Table 4.5: Kinetic parameters for the metal-DLC layers derived from simulations (n = 3).

Sample	k_s ($\times 10^{-3}$ cm/s) $Ru(NH_3)_6^{3+/2+}$	k_s ($\times 10^{-3}$ cm/s) $Fe(CN)_6^{4-/3-}$	α $Ru(NH_3)_6^{3+}$	$1-\alpha$ $Fe(CN)_6^{4-}$
Au #1	6.1 ± 1.6	3.5 ± 0.7	0.50 ± 0.03	0.50 ± 0.01
Au #2	3.5 ± 0.9	2.3 ± 0.8	0.51 ± 0.01	0.46 ± 0.02
Au #3	2.4 ± 0.9	1.0 ± 0.1	0.51 ± 0.01	0.48 ± 0.03
Pt #1	4.3 ± 0.6	2.8 ± 0.5	0.52 ± 0.01	0.49 ± 0.02
Pt #2	2.3 ± 0.2	1.3 ± 0.1	0.52 ± 0.01	0.48 ± 0.01
Pt #3	2.3 ± 0.8	1.3 ± 0.3	0.52 ± 0.02	0.48 ± 0.02

The k_s values calculated for both redox mediators are one to two orders of magnitude smaller compared to those determined for the same redox systems at glassy carbon,[44-46] and doped diamond.[47, 48] A comparison to N-DLC electrodes reveals that the heterogeneous electron transfer at metal-DLC occurs two to three times slower, however the k_s values reported herein are approximately two orders of magnitude higher than those previously published.[12]

The oxygen-to-carbon (O/C) ratio in the metal-DLC layers studied here does not vary with metal content (see *Table 3.2*), hence, any influence on the electrochemical behavior of these nanocomposite electrodes may be neglected in the context of this study.

4.3.7 Scanning electrochemical microscopy studies

According to literature,[8] the presence of metal particulates at the surface of metal-DLC generates regions with increased electrochemical activity. The local electrochemical activity at a surface can typically be probed by scanning electrochemical microscopy (SECM). According to Bard et al.,[49] conducting features as small as one-tenth of the ultramicroelectrode (UME) size should be detectable, provided that the normalized tip-to-

substrate distance (L) is at most 0.1. The conducting features observed on the metal-DLC layers display radii of up to 150 nm, meaning that an UME with a radius of 1.5 µm positioned at 150 nm away from surface would be required in order to determine the presence of conducting features.

However, the density of particulates at the metal-DLC surfaces is too high, therefore, the obtained response would reflect the average value obtained with several particulates. Furthermore, at the small tip-to-substrate distances required by this sample, precise height control is critical, and sample tilt and uneven morphology will result in "tip crashing", damaging the substrate and UME.[50]

4.3.8 Spectroelectrochemical studies

As depicted in *Table 2.1*, the penetration depth is higher at ZnSe ATR than at other common waveguide materials. Therefore, preliminary studies with metal-DLC coated waveguides were conducted on zinc selenide (ZnSe) ATR crystals, however the layer delaminated from the waveguide when a potential step of +600 mV (vs. AgQRE) in 0.1 KCl was applied (*Figure 4.9*). Due to limitations of the deposition system, the substrates coated with metal-DLC were not ion etched prior to the deposition, unlike the ZnSe substrates presented in *Section 3.3.5*. Hence, the increased stress originating from the exposure to the electric field was sufficient to induce delamination of the poorly adhering film from the substrate.[51]

In the absence of ion etching, the presence of an interfacial layer can also improve the adhesion of DLC to the substrate. Thick (~ 1 µm) DLC layers have shown excellent adhesive properties to silicon[52] and germanium[53, 54] due to the formation of a carbide phase. In contrast, only relatively thin DLC films (< 300 nm) can be grown on zinc

sulfide (ZnS)[37, 55] and ZnSe[37] due to the lack of intermixing between DLC and substrate phases.

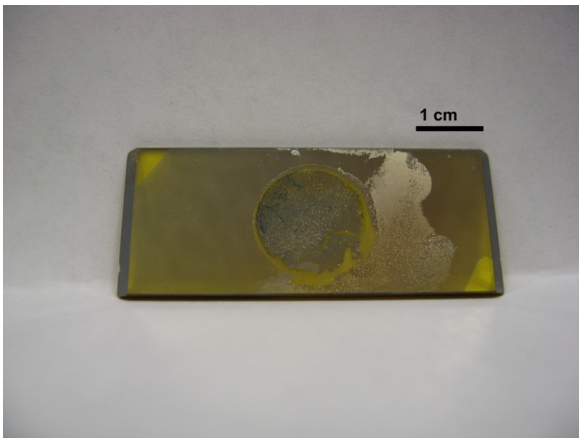

Figure 4.9: Optical image of delaminated platinum-DLC layer, which was deposited onto ZnSe after the application of a potential step of +600 mV (vs. AgQRE) in 0.1 M KCl.

XPS depth profiling of a platinum-DLC layer deposited onto a germanium substrate (*Figure 4.10(a)*) confirms that the DLC and germanium phases are intimately mixed. Additionally, evidence of the formation of germanium-carbon bonds is derived from the shift in binding energy of the C 1s photoemission peak to values below 284 eV (*Figure 4.10(b)*).[53, 54]

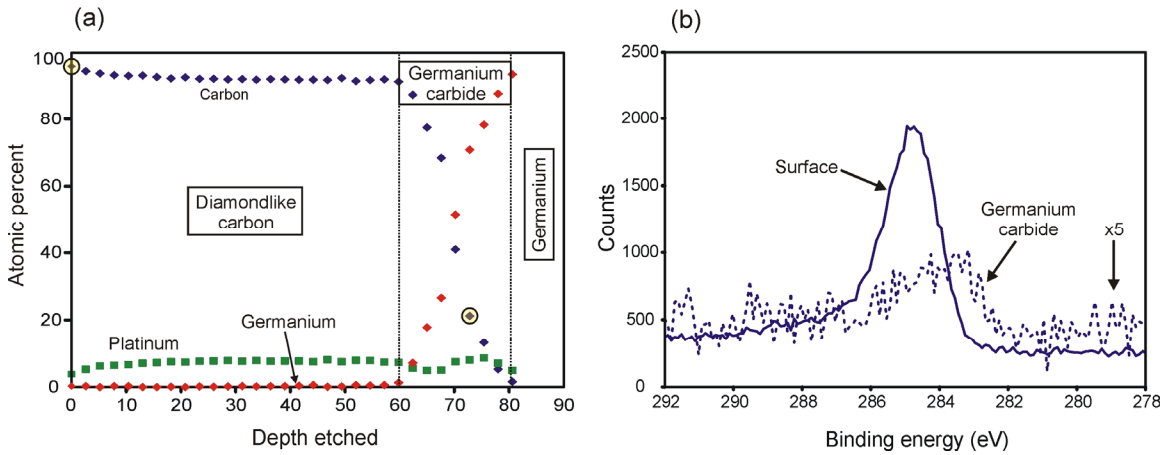

Figure 4.10: (a) XPS depth profile of platinum-DLC on germanium. The two highlighted carbon data points correspond to surface carbon and germanium carbide. The C 1s spectra for the corresponding two data points are shown in (b).

However, exposure of the metal-DLC coated germanium waveguide to anodic potentials (+600 mV vs. AgQRE in 0.1 M KCl) resulted in blistering of the coating and pitting of the waveguide (*Figure 4.11*). Corrosion of germanium occurs at anodic potentials as low as 300 mV (vs. SHE).[56, 57] Hence, dissolution of the waveguide is likely to occur with imperfections in the DLC coating.[56, 58-60] Pinholes in the DLC layer provide pathways for the electrolyte to reach the underlying substrate and initiate the dissolution process. Germanium is suitable for electrochemical analysis restricted to cathodic potentials,[61] however in general, the presence of pinholes will persistently limit the use of metal-DLC nanocomposite electrodes for spectroelectrochemistry. The uniformity of metal-DLC layers has to be improved to become viable optically transparent electrodes. Therefore, future efforts will be directed towards the formation of homogeneous, pinhole-free layers.

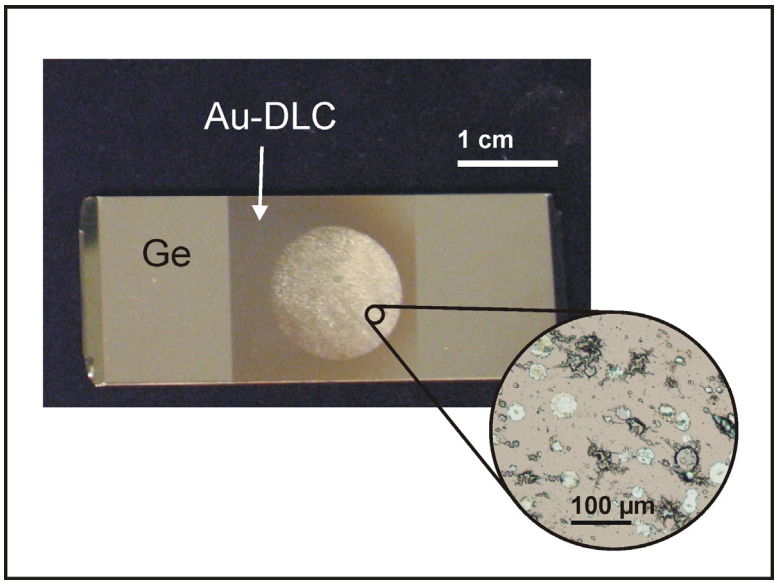

Figure 4.11: Optical image of delaminated gold-DLC layer deposited on a germanium waveguide after applying +600 mV (vs. AgQRE) in 0.1 M KCl.

4.4 Final remarks

A detailed characterization of the physical and electrochemical properties of metal-DLC layers was achieved in this study. The inclusion of noble metal nanoclusters into the layers resulted in an improved electronic conduction, rendering them suitable for electrochemical applications. In addition, germanium waveguides coated with 4 cm^2 sections of metal-DLC layers displayed sufficient mid-IR transparency for spectroscopic applications. Despite, further necessary improvements in the film quality and the adhesive properties to waveguiding materials, the nanocomposite layers described in this study are suitable optically transparent electrodes for mid-IR spectroelectrochemistry.

Additionally, continuing efforts should be directed towards elucidating the conducting mechanism in metal-DLC nanocomposites. Both the fraction of sp^2-hybridized carbon and the metal content increase concomitantly (see *Sections 4.3.1* and *4.3.3*), and as a result, an unambiguous description of the conduction mechanism is not possible.

As the homogenous and heterogeneous conduction occurs via different pathways,[8, 13] by depositing additional nanocomposite layers as shown in *Figure 4.12*, it is envisioned that the two pathways can be separated. This should allow to distinguish between the. catalytic heterogeneous conduction from the homogeneous conduction (hopping through sp^2-clusters), providing more detailed information about the influence of each on the electrical properties of metal-DLC nanocomposite thin films.

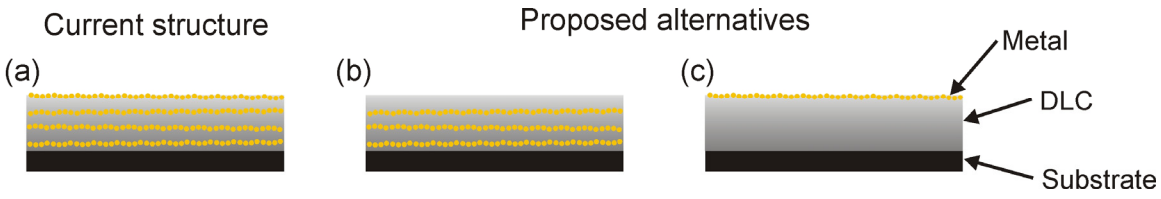

Figure 4.12: Schematic representation of the metal-DLC nanocomposite thin films as they are (a) currently deposited, along with (b-c) the structures proposed for investigation of the conducting properties.

Furthermore, the electron transfer rate of $Fe(CN)_6^{4-/3-}$ at carbon surfaces can be suppressed by modification of C=O bonds with dinitrophenylhydrazine.[45] This would permit further distinction between the heterogeneous electron transfer occurring at the metal versus the sp^2-sites.

4.5 References

1. Benndorf, C.; Boettger, E.; Fryda, M.; Haubold, H. G.; Klages, C. P.; Koeberle, H., *Electrical conductivity and microstructure of metal containing hydrogenated amorphous carbon films*, Synth. Met., **43 (3)**, 4055-4058, (1991).

2. Yoo, K.; Miller, B.; Kalish, R.; Shi, X., *Electrodes of nitrogen-incorporated tetrahedral amorphous carbon. A novel thin-film electrocatalytic material with diamond-like stability*, Electrochem. Solid-State Lett., **2 (5)**, 233-235, (1999).

3. Mominuzzaman, S. M.; Ebisu, H.; Soga, T.; Jimbo, T.; Umeno, M., *Phosphorus doping and defect studies of diamond-like carbon films by pulsed laser deposition using camphoric carbon target*, Diamond Relat. Mater., **10 (3-7)**, 984-988, (2001).

4. Fan, X.; Dickey, E. C.; Pennycook, S. J.; Sunkara, M. K., *Z-contrast imaging and electron energy-loss spectroscopy analysis of chromium-doped diamond-like carbon films*, Appl. Phys. Lett., **75 (18)**, 2740-2742, (1999).

5. Koduri, P.; Sunkara, M. K.; Dickey, E. C.; Frazier, C.; Babu, S. V., *Structural and electrochemical characterization of metal doped diamondlike carbon films*, Surf. Eng., **15 (5)**, 373-376, (1999).

6. Lian, G. D.; Dickey, E. C.; Ueno, M.; Sunkara, M. K., *Ru-doped nanostructured carbon films*, Diamond Relat. Mater., **11 (12)**, 1890-1896, (2002).

7. Rusli; Yoon, S. F.; Yang, H.; Ahn, J.; Huang, Q. F.; Zhang, Q.; Guo, Y. P.; Yang, C. Y.; Teo, E. J.; Wee, A. T. S.; Huan, A. C. H., *Investigation of tungsten incorporated amorphous carbon film*, Thin Solid Films, **355-356**, 174-178, (1999).

8. Pleskov, Y. V.; Evstefeeva, Y. E.; Baranov, A. M., *Threshold effect of admixtures of platinum on the electrochemical activity of amorphous diamond-like carbon thin films*, Diamond Relat. Mater., **11 (8)**, 1518-1522, (2002).

9. Corbella, C.; Oncins, G.; Gomez, M. A.; Polo, M. C.; Pascual, E.; Garcia-Cespedes, J.; Andujar, J. L.; Bertran, E., *Structure of diamond-like carbon films containing transition metals deposited by reactive magnetron sputtering*, Diamond Relat. Mater., **14 (3-7)**, 1103-1107, (2005).

10. Grill, A.; Patel, V., *Tribological properties of diamond-like carbon and related materials*, Diamond Relat. Mater., **2 (5-7)**, 597-605, (1993).

11. Inkin, V. N.; Kirpilenko, G. G.; Dementjev, A. A.; Maslakov, K. I., *A superhard diamond-like carbon film*, Diamond Relat. Mater., **9 (3-6)**, 715-721, (2000).

12. Sunkara, M. K.; Chandrasekaran, H.; Koduri, P., *Electrochemical studies of metal-doped diamondlike carbon films*, New Diamond Front. Carbon Technol., **9 (6)**, 407-415, (1999).

13. Pleskov, Y. V.; Evstefeeva, Y. E.; Baranov, A. M., *Amorphous diamond-like carbon electrodes: the catalytic effect of platinum admixture*, Russ. J. Electrochem., **37 (6)**, 644-646, (2001).

14. Rong, Z. Y.; Abraizov, M.; Dorfman, B.; Strongin, M.; Yang, X.-Q.; Yan, D.; Pollak, F. H., *Scanning tunneling microscopy of diamond-like nanocomposite films*, Appl. Phys. Lett., **65 (11)**, 1379-1381, (1994).

15. Narayan, R. J., *Pulsed laser deposition of functionally gradient diamondlike carbon-metal nanocomposites*, Diamond Relat. Mater., **14 (8)**, 1319-1330, (2005).

16. van de Riet, E.; Nillesen, C. J. C. M.; Dieleman, J., *Reduction of droplet emission and target roughening in laser ablation and deposition of metals*, J. Appl. Phys., **74 (3)**, 2008-2012, (1993).

17. Faehler, S.; Stoermer, M.; Krebs, H. U., *Origin and avoidance of droplets during laser ablation of metals*, Appl. Surf. Sci., **109/110 (Laser Processing of Surfaces and Thin Films)**, 433-436, (1997).

18. Czanderna, A. W., *Overview of ion spectroscopies for surface compositional analysis*, Methods of Surface Characterization, **2 (Ion Spectrosc. Surf. Anal.)**, 1-44, (1991).

19. Niwa, O.; Jia, J.; Sato, Y.; Kato, D.; Kurita, R.; Maruyama, K.; Suzuki, K.; Hirono, S., *Electrochemical Performance of Angstrom Level Flat Sputtered Carbon Film Consisting of sp2 and sp3 Mixed Bonds*, J. Am. Chem. Soc., **128 (22)**, 7144-7145, (2006).

20. Yee, N. C.; Shi, Q.; Cai, W.-B.; Scherson, D. A.; Miller, B., *Electrochemical characterization of nitrogen-incorporated tetrahedral carbon films grown by a filtered cathodic vacuum arc*, Electrochem. Solid-State Lett., **4 (10)**, E42-E44, (2001).

21. Bewilogua, K.; Wittorf, R.; Thomsen, H.; Weber, M., *DLC based coatings prepared by reactive d.c. magnetron sputtering*, Thin Solid Films, **447-448**, 142-147, (2004).

22. Arena, C.; Kleinsorge, B.; Robertson, J.; Milne, W. I.; Welland, M. E., *Electronic and topographic structure of ta-C, ta-C:N and ta-C:B investigated by scanning tunnelling microscopy*, Diamond Relat. Mater., **8 (2-5)**, 435-439, (1999).

23. Steffen, H. J.; Roux, C. D.; Marton, D.; Rabalais, J. W., *Auger-electron-spectroscopy analysis of chemical states in ion-beam-deposited carbon layers on graphite*, Phys. Rev. B: Condens. Matter Mater. Phys., **44 (8)**, 3981-3990, (1991).

24. Kelly, R., *On the problem of whether mass or chemical bonding is more important to bombardment-induced compositional changes in alloys and oxides*, Surf. Sci., **100 (1)**, 85-107, (1980).

25. Bozhko, A.; Takagi, T.; Takeno, T.; Shupegin, M., *Electron transport in W-containing amorphous carbon-silicon diamond-like nanocomposites*, J. Phys.: Condens. Matter, **16 (46)**, 8447-8458, (2004).

26. Wu, W.-y.; Ting, J.-m., *Growth and characteristics of carbon films with nano-sized metal particles*, Thin Solid Films, **420-421**, 166-171, (2002).

27. Wagner, J.; Ramsteiner, M.; Wild, C.; Koidl, P., *Resonant Raman scattering of amorphous carbon and polycrystalline diamond films*, Phys. Rev. B: Condens. Matter Mater. Phys., **40 (3)**, 1817-1824, (1989).

28. Afonso, C. N.; Serna, R.; Ballesteros, J. M.; Petford-Long, A. K.; Doole, R. C., *Synthesis by pulsed laser deposition of metallic nanoclusters embedded in an amorphous host*, Appl. Surf. Sci., **127-129**, 339-343, (1998).

29. Narayan, R. J., *Laser processing of diamond-like carbon-metal composites*, Appl. Surf. Sci., **245 (1-4)**, 420-430, (2005).

30. Shim, J.-H.; Lee, B.-J.; Cho, Y. W., *Thermal stability of unsupported gold nanoparticle: a molecular dynamics study*, Surf. Sci., **512 (3)**, 262-268, (2002).

31. Morrison, M. L.; Buchanan, R. A.; Liaw, P. K.; Berry, C. J.; Brigmon, R. L.; Riester, L.; Abernathy, H.; Jin, C.; Narayan, R. J., *Electrochemical and antimicrobial properties of diamondlike carbon-metal composite films*, Diamond Relat. Mater., **15 (1)**, 138-146, (2006).

32. Narayan, R. J.; Abernathy, H.; Riester, L.; Berry, C. J.; Brigmon, R., *Antimicrobial properties of diamond-like carbon-silver-platinum nanocomposite thin films*, J. Mater. Eng. Perform., **14 (4)**, 435-440, (2005).

33. Yoshitake, T.; Nagayama, K., *The velocity distribution of droplets ejected from Fe and Si targets by pulsed laser ablation in a vacuum and their elimination using a vane-type velocity filter*, Vacuum, **74 (3-4)**, 515-520, (2004).

34. Nakata, Y.; Gunji, S.; Okada, T.; Maeda, M., *Fabrication of LiNbO3 thin films by pulsed laser deposition and investigation of nonlinear properties*, Appl. Phys. A: Mater. Sci. Process., **A79 (4-6)**, 1279-1282, (2004).

35. Janotta, M.; Rudolph, D.; Kueng, A.; Kranz, C.; Voraberger, H.-S.; Waldhauser, W.; Mizaikoff, B., *Analysis of Corrosion Processes at the Surface of Diamond-Like Carbon Protected Zinc Selenide Waveguides*, Langmuir, **20 (20)**, 8634-8640, (2004).

36. Janotta, M.; Vogt, F.; Voraberger, H.-S.; Waldhauser, W.; Lackner Jurgen, M.; Stotter, C.; Beutl, M.; Mizaikoff, B., *Direct analysis of oxidizing agents in aqueous solution with attenuated total reflectance mid-infrared spectroscopy and diamond-like carbon protected waveguides*, Anal. Chem., **76 (2)**, 384-391, (2004).

37. Keeley, J. T.; Wu, R. L. C., *Diamond-like carbon films as a protective coating for zinc sulfide and zinc selenide optics*, Proc. - Electrochem. Soc., **89-12 (Proc. Int. Symp. Diamond Diamond-Like Films, 1st, 1989)**, 250-260, (1989).

38. Norskov, J. K.; Bligaard, T.; Logadottir, A.; Kitchin, J. R.; Chen, J. G.; Pandelov, S.; Stimming, U., *Trends in the exchange current for hydrogen evolution*, J. Electrochem. Soc., **152 (3)**, J23-J26, (2005).

39. Adamopoulos, G.; Godet, C.; Deslouis, C.; Cachet, H.; Lagrini, A.; Saidani, B., *The electrochemical reactivity of amorphous hydrogenated carbon nitrides for varying nitrogen contents: the role of the substrate*, Diamond Relat. Mater., **12 (3-7)**, 613-617, (2003).

40. Zeng, A.; Liu, E.; Tan, S. N.; Zhang, S.; Gao, J., *Cyclic voltammetry studies of sputtered nitrogen doped diamond-like carbon film electrodes*, Electroanalysis, **14 (15-16)**, 1110-1115, (2002).

41. You, T.; Niwa, O.; Horiuchi, T.; Tomita, M.; Iwasaki, Y.; Ueno, Y.; Hirono, S., *Co-Sputtered Thin Film Consisting of Platinum Nanoparticles Embedded in Graphite-Like Carbon and Its High Electrocatalytic Properties for Electroanalysis*, Chem. Mater., **14 (11)**, 4796-4799, (2002).

42. Rajalakshmi, N.; Ryu, H.; Dhathathreyan, K. S., *Platinum catalysed membranes for proton exchange membrane fuel cells - higher performance*, Chem. Eng. J. (Amsterdam, Neth.), **102 (3)**, 241-247, (2004).

43. Gomez de la Fuente, J. L.; Rojas, S.; Martinez-Huerta, M. V.; Terreros, P.; Pena, M. A.; Fierro, J. L. G., *Functionalization of carbon support and its influence on the electrocatalytic behaviour of Pt/C in H2 and CO electrooxidation*, Carbon, **44 (10)**, 1919-1929, (2006).

44. Chen, P.; Fryling, M. A.; McCreery, R. L., *Electron Transfer Kinetics at Modified Carbon Electrode Surfaces: The Role of Specific Surface Sites*, Anal. Chem., **67 (18)**, 3115-3122, (1995).

45. Chen, P.; McCreery, R. L., *Control of electron transfer kinetics at glassy carbon electrodes by specific surface modification*, Anal. Chem., **68 (22)**, 3958-3965, (1996).

46. Chen, Q.; Swain, G. M., *Structural Characterization, Electrochemical Reactivity, and Response Stability of Hydrogenated Glassy Carbon Electrodes*, Langmuir, **14 (24)**, 7017-7026, (1998).

47. Hupert, M.; Muck, A.; Wang, J.; Stotter, J.; Cvackova, Z.; Haymond, S.; Show, Y.; Swain, G. M., *Conductive diamond thin-films in electrochemistry*, Diamond Relat. Mater., **12 (10-11)**, 1940-1949, (2003).

48. Chen, Q.; Gruen, D. M.; Krauss, A. R.; Corrigan, T. D.; Witek, M.; Swain, G. M., *The structure and electrochemical behavior of nitrogen-containing nanocrystalline diamond films deposited from CH4/N2/Ar mixtures*, J. Electrochem. Soc., **148 (1)**, E44-E51, (2001).

49. Bard, A. J.; Mirkin, M. V.; Unwin, P. R.; Wipf, D. O., *Scanning electrochemical microscopy. 12. Theory and experiment of the feedback mode with finite heterogeneous electron-transfer kinetics and arbitrary substrate size*, J. Phys. Chem., **96 (4)**, 1861-1868, (1992).

50. Kranz, C.; Friedbacher, G.; Mizaikoff, B.; Lugstein, A.; Smoliner, J.; Bertagnolli, E., *Integrating an Ultramicroelectrode in an AFM Cantilever: Combined Technology for Enhanced Information*, Anal. Chem., **73 (11)**, 2491-2500, (2001).

51. Klinger, L.; Glickman, E.; Katsman, A.; Levin, L., *Time dependence of stress and hillock distributions during electromigration in thin metal film interconnections*, Materials Science & Engineering, B: Solid-State Materials for Advanced Technology, **B23 (1)**, 15-18, (1994).

52. Wittmer, M.; Ugolini, D.; Eitle, J.; Oelhafen, P., *Amorphous hydrogenated carbon films on semiconductors. II. Microstructural properties of the interface*, Appl. Phys. A, **A48 (6)**, 559-566, (1989).

53. Wittmer, M.; Ugolini, D.; Oelhafen, P., *Interface properties of hydrogenated amorphous carbon films on germanium (100) surfaces*, J. Electrochem. Soc., **137 (4)**, 1256-1261, (1990).

54. Bruce, T.; Bello, I.; Huang, L. J.; Lau, W. M.; High, M.; Strnad, V.; Panchhi, P., *Interfacial characterization of ion-beam-deposited a-C films on Ge*, J. Appl. Phys., **76 (1)**, 552-557, (1994).

55. Bruce, T.; Huang, L. J.; Bello, I.; Lau, W. M.; Panchhi, P.; Strnad, V.; High, M., *Interfacial reactions of ion beam deposited a-C films on ZnS*, J. Vac. Sci. Technol., A, **12 (4, Pt. 1)**, 1487-1490, (1994).

56. Higashiyama, T.; Takenaka, T., *Infrared attenuated total reflection spectra of adsorbed layers at the interface between a germanium electrode and an aqueous solution of sodium laurate*, J. Phys. Chem., **78 (9)**, 941-947, (1974).

57. Bard, A. J.; Editor, *Encyclopedia of Electrochemistry of the Elements, Vol. 6*. 1976; p 341 pp.

58. Reed, A. H.; Yeager, E., *Infrared internal reflection studies of the germanium/electrolyte interface*, Electrochim. Acta, **15 (8)**, 1345-1354, (1970).

59. Efimov, E. A.; Erusalimchik, I. G., *Electrochemistry of Germanium and Silicon. Translated from the Russian*. 1963; p 199 pp.

60. Mark, H. B., Jr.; Pons, B. S., *In situ spectrophotometric method for observing the infrared spectra of species at the electrode surface during electrolysis*, Anal. Chem., **38 (1)**, 119-121, (1966).

61. Mattson, J. S.; Smith, C. A., *Optically transparent carbon film electrodes for infrared spectroelectrochemistry*, Anal. Chem., **47 (7)**, 1122-1125, (1975).

5 SPECTROSCOPIC AND ELECTROCHEMICAL STUDIES ON THE DEPOSITION CONDITIONS FOR CATHODICALLY ELECTROPOLYMERIZED POLY(4-VINYLPYRIDINE) IN ACETONITRILE

A detailed spectroscopic analysis of the pre-polymerization solution containing the 4-vinylpyridine monomer and varying amounts of perchloric acid, as well as optimized polymerization conditions are presented in this chapter. Furthermore, the behavior of electropolymerized poly(4-vinylpyridine) semipermeable membranes towards hexacyanoferrate species is discussed.

5.1 Motivation

The selectivity of spectroelectrochemical platforms is based on the electrochemical activity of the analyte and the optical absorbance at the wavelength range selected. Employing a partitioning membrane can further improve the selectivity by preventing the interaction of interferants with the transduction mechanism. The sensitivity of the spectroelectrochemical platform can also benefit if the analyte is pre-concentrated in the partitioning membrane.

Anion-exchange membranes spin-coated onto UV-Vis ATR spectroelectrochemical sensing platforms resulted in increased selectivity and sensitivity towards $Fe(CN)_6^{4-}$.[1, 2] However, degradation of the polymer in harsh chemical environments diminishes the temporal stability of the platform. Membranes deposited via the electropolymerization technique display increased mechanical robustness over solvent-casted membranes due to

a higher degree of crosslinking.[3, 4] Similar to solvent-casted poly(4-vinylpyridine)[5], membranes obtained from the electropolymerization of the 4-VP monomer have shown anion-exchange properties.[6]

Therefore, the mid-IR ATR spectroelectrochemical platform previously discussed (*Chapters 3* and *4*) can be further improved through the incorporation of the electropolymerized poly(4-VP) membrane described in this chapter.

Thick, vinylpyridine-based membranes cathodically electropolymerized from aqueous solutions require the presence of protonated monomers and operation at potential ranges yielding intense hydrogen evolution. In order to prevent delamination of DLC from the substrates due to the hydrogen evolution, our approach establishes the electropolymerization of 4-VP in organic solvents, specifically acetonitrile. Additionally, since the activity of the hydrogen ion is not directly measurable with a glass electrode,[7] IR, NMR, and UV spectroscopic titrations were devised to study the effects of acid addition to pre-polymerization solutions in acetonitrile. In addition, the spectroscopic data also serves to provide further insight regarding the structural isomer in solution responsible for initiating the electropolymerization process.

Finally, Ling et al.[8] reported that electropolymerized poly(2-VP) deposited in the presence of perchlorate anions displayed improved adherence to the substrate as well as uniformity and rigidity relative to films deposited in the presence of sulfate, nitrate or chloride anions. A similar effect have been described for solvent-casted poly(vinylpyridine) films.[9] The improved robustness in perchlorate containing films has been attributed to the anions interaction with the pyridine moieties, resulting in extensive electrostatic crosslinking.[9] Hence, studies on the electropolymerization conditions of

poly(4-VP) discussed in this chapter will be restricted to pre-polymerization solutions containing perchlorate anions.

5.1.1 Poly(4-vinylpyridine) as an anion selective membrane

The ion-exchange properties of electropolymerized poly(4-VP) films can vary significantly depending upon the applied potential range, as well as the composition of the pre-polymerization solution. For example, Finklea and co-workers[10] reported that thin, selectively insulating films can be generated at anodic potentials (> +1 V vs. SSCE), which block the transport of ions to the electrode, but allow the permeation of neutral species such as hydroquinone. Lebrun[11, 12] showed that 4-VP can also be electropolymerized at cathodic potentials (-2.8 V vs. Ag/Ag^{+}) resulting in films slightly thicker than anodically deposited membranes (60 nm vs. 10 nm). While the diffusion of either ionic or neutral species was not evaluated in this study, Viel and co-workers[13] have reported evidence that cathodically electrodeposited poly(4-VP) incorporates Cu^{2+} ions, thereby demonstrating that polymer films grown under those conditions behave differently from anodically deposited poly(4-VP). Furthermore, by protonating or quaternizing the nitrogen atom at the pyridine ring, an anion-exchange polymer is obtained. Bartak and co-workers[3] have explored this property to saturate electrochemically grown poly(4-VP) films with $PtCl_4^{2-}$ and subsequently reducing the anions to metallic platinum clusters embedded into the polymer matrix. Thus, films with enhanced electrocatalytic properties were obtained. Li et al.[6] used a similar approach to introduce $PdCl_4^{2-}$ ions into the film yielding a membrane loaded with palladium clusters that is responsive to concentration changes of hydrazine in solution.

Sekine and co-workers[14] studied the corrosion inhibition properties of polymer-coated steel substrates in concentrated sodium chloride solutions. The authors concluded that cathodically electropolymerized films based on vinylpyridine monomers (both 2- and 4-substituted) are well suited as protective membranes due to the film uniformity and high durability at the tested conditions, especially if the polymer is cured at 130 ºC for 30 min. Similar corrosion studies at zinc substrates using cathodically electropolymerized 2-VP were performed shortly thereafter by De Bruyne[15] corroborating these findings.

Ling and co-workers devised an electropolymerization procedure for 2-VP involving the partial protonation of the monomer, yielding polymer films of several micrometers in thickness.[16] Detailed optimization studies on the electropolymerization conditions concluded that poly(2-VP) film quality varies with monomer concentration, solvent composition, and addition of an acid to the solution.[8, 16] Their observations indicate that the highest quality films result from a pre-polymerization solution acidified with perchloric acid to a pH comparable to the pKa of the monomer.[17] However, the solvent composition (85:15 H_2O:CH_3OH) selected by the authors limits the formation of uniform thin films due to intense hydrogen gas evolution resulting from the applied potential range (-2.5 V vs. SCE).[16]

5.2 Experimental

5.2.1 Spectroscopic characterization

HPLC grade acetonitrile (Honeywell Jackson & Burdick, Muskegon, MI) was used for all experiments except for NMR studies, where acetonitrile-d_3 containing 1 % v/v tetramethylsilane (Sigma Aldrich, St. Louis, MA) was utilized. Infrared spectra were recorded in transmission mode using a PIKE Technologies (Madison, WI) liquid cell

fitted with NaCl windows and a PTFE spacer with a nominal thickness of 50 μm on a Bruker Optics Equinox 55 FT-IR spectrometer (Billerica, MA) equipped with a broad-band liquid nitrogen-cooled mercury-cadmium-telluride (MCT) detector from Infrared Associates (Stuart, FL). A total of 100 spectra were averaged per measurement in a spectral range of 4000-400 cm^{-1} at 4 cm^{-1} resolution.

A 300 MHz Varian, Inc. Vx 300 (Palo Alto, CA) NMR spectrometer equipped with a 5 mm probe head was used for all ^{1}H NMR experiments.

The UV spectra were recorded with a 1 mm pathlength silica cuvette at 2 nm spectral resolution using a Shimadzu Scientific Instruments, Inc. UV-3101PC (Columbia, MD) scanning spectrometer.

5.2.2 Polymer formation and electrochemical characterization

The 4-vinylpyridine monomer was distilled under reduced pressure to remove the hydroquinone inhibitor (Sigma Aldrich, St. Louis, MA). The distillate was stored in sealed glass vials at -14 ºC. Tetraethylammonium perchlorate (TEAP; RSA Corporation, Danbury, CT) was used as the supporting electrolyte for all electropolymerization reactions, and was further purified by double recrystallization from HPLC grade methanol (Honeywell Jackson & Burdick, Muskegon, MI), subsequently dried, and stored at 110 ºC. Platinum disc electrodes (ø = 1 mm) were polished to a mirror finish using 6, 3, and 1 μm diamond, and 0.05 μm γ-alumina paste (Leco, St. Joseph, MI) utilizing polishing microcloths (Buehler Ltd., Lake Bluff, IL). The electrodes were subsequently sonicated and electrochemically cleaned in 0.5 M sulfuric acid (Fisher Scientific, Fair Lawn, NJ). The polymer films were formed by cyclic voltammetry in solutions containing 15.8 mM 4-vinylpyridine, 0.1 M TEAP and varying amounts of

perchloric acid (Fisher Scientific, Fair Lawn, NJ) for a total of 50 cycles at a scan rate of 0.1 V/s from the open circuit potential to -2.73 V (vs. Fc/Fc^{+}).

The electrochemical characterization was performed by exposing the freshly deposited polymer films to 5 mM hexaammineruthenium(III) trichloride ($Ru(NH_3)_6^{3+}$) and 5 mM potassium hexacyanoferrate(II) trihydrate ($Fe(CN)_6^{4-}$) in a supporting electrolyte solution containing 0.1 M or 0.5 M potassium chloride (Sigma Aldrich, St. Louis, MA). Cyclic voltammograms of the modified electrodes in redox mediator solutions were recorded every 10 min for 60 min at 0.01 V/s. In order to verify the pH dependence of the anion uptake into poly(4-VP) films, some $Fe(CN)_6^{4-}$ solutions were acidified with concentrated hydrochloric acid (Fisher Scientific, Fair Lawn, NJ). All solutions for electrochemical analysis were sparged with argon from Airgas (Marietta, GA) for at least 15 min prior to use; additionally, the argon stream used to sparge the pre-polymerization solutions was saturated with acetonitrile in order to minimize solvent evaporation. Two potentiostats (CH Instruments models 440A and 660A, Austin, TX) were used to electropolymerize and characterize the polymer films.

5.3 Results

5.3.1 Infrared spectroscopic studies

Transmission-absorption experiments at optical pathlengths on the order of magnitude of the utilized wavelength range typically result in interference fringes, arising from multiple reflections at the interface between the sample and the sodium chloride windows.[18] By measuring the periodicity of these interference fringes, the effective optical pathlength is determined using the following equation:

$$d = \frac{1}{2n_s\Delta}, \tag{5.1}$$

where d is the pathlength, n_s is the refractive index of the sample in the liquid cell (acetonitrile, $n = 1.34$) and Δ is the periodicity. The calculated pathlength was 46 ± 3 µm (n = 4). The corrected optical pathlengths were used to normalize the quantitative results shown in *Figure 5.2*.

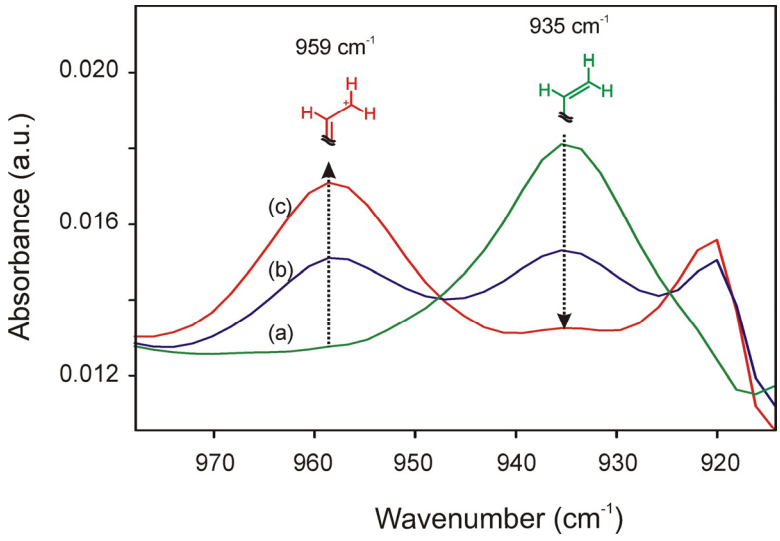

Figure 5.1: Infrared spectra of polymerization solutions containing 15.8 mM 4-VP and (a) no acid, (b) 7.9 mM perchloric acid, and (c) 22.5 mM perchloric acid.

The infrared spectral features of 4-VP have already been studied in detail in literature.[19-23] The feature of interest to this study is the out-of-plane bending mode from the vinyl group at 935 cm^{-1}. This band is especially sensitive to substitution patterns at the α-carbon (i.e. the carbon closest to the pyridine ring), shifting to higher wavenumbers if the vinyl group is attached to an electron withdrawing group, and vice-versa.[24] At the conditions studied here, protonation of the pyridine ring leads to a blue shift of this band of approx. 25 cm^{-1} (*Figure 5.1*). By comparing the area of these two bands, a quantitative

relationship between the neutral and the protonated monomer has been established, as shown in *Figure 5.2*.

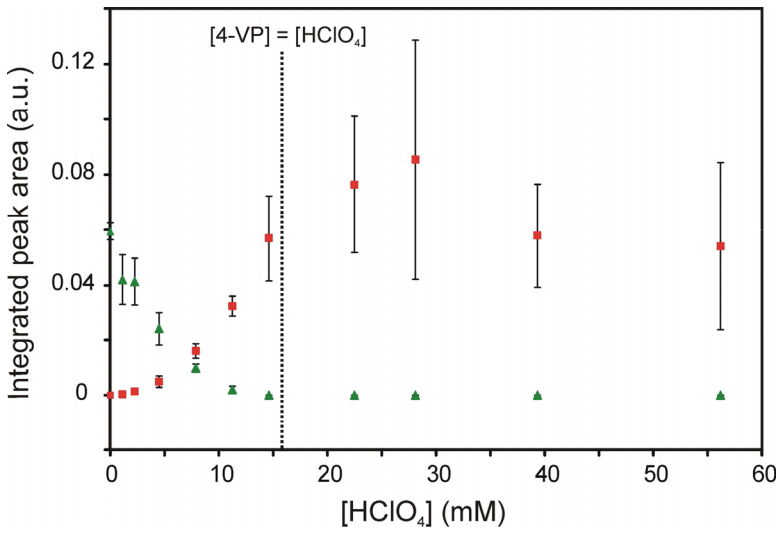

Figure 5.2: Integrated peak area for the vinyl out-of-plane bending for the unprotonated (▲) and protonated (■) monomer as a function of the added amount of acid (n = 4).

Examination of *Figure 5.2* suggests that an equimolar ratio of protonated to unprotonated 4-VP occurs at an acid concentration of approx. 7.9 mM. The presence of large error bars at acid concentrations above 15 mM $HClO_4$ is attributed to dissolution of the NaCl cell windows occurring upon increasingly higher water content accompanying the higher acid content in the analyzed solutions (up to 148 mM water).

5.3.2 Ultraviolet spectroscopic studies

IR spectroscopic studies provide detailed information about changes in the bonding arrangement of 4-VP upon addition of $HClO_4$. Complementarily, UV spectroscopy is sensitive to electronic transitions and can detect subtle changes occurring in the π-electron cloud, as the 4-VP monomer is titrated. Due to the monomer fully absorbing the

incident radiation, a ten-fold dilution of the analytes was required to ensure useful signal levels.

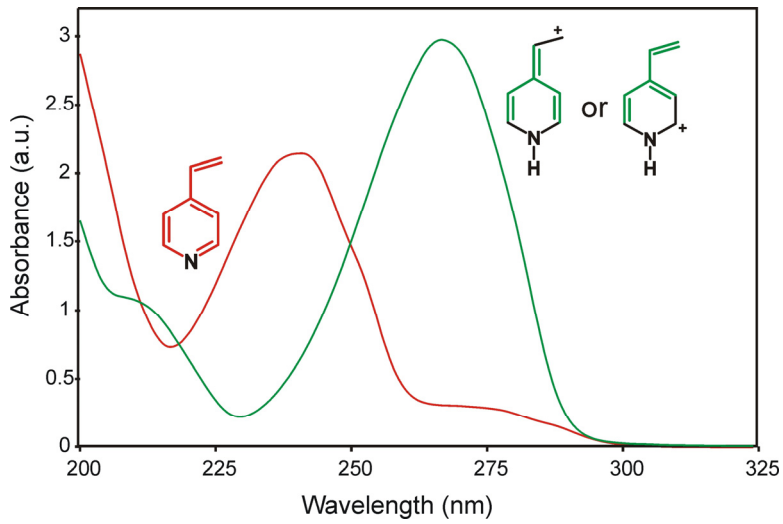

Figure 5.3: Ultraviolet spectra of solutions containing 15.8 mM 4-VP in the (a) unprotonated or (b) protonated form dissolved in acetonitrile.

Curve (a) in *Figure 5.3* shows the UV absorption spectrum of neutral 4-VP in acetonitrile. The spectrum contains an absorption maximum at approximately 240 nm, corresponding to the π-π* transition of the aromatic ring, and a second absorption feature at approximately 272 nm corresponding to the forbidden n-π* transition of the lone electron pair at the nitrogen atom.[25] The observed spectral features correspond well with findings previously reported in literature for this compound.[19, 26-28] *Figure 5.3*(b) represents the spectrum obtained in the case of a solution containing fully protonated 4-VP monomers. The peak corresponding to the π-π* transition in neutral 4-VP entirely disappears indicating a loss in aromaticity. In addition, the n-π* peak also disappears, as predicted[25]. In contrast, an absorbance band with a maximum at 266 nm increases in intensity with the addition of the acid, and reaches a maximum intensity at a 1:1 ratio of

[4-VP]:[$HClO_4$] indicating that all monomer in solution has been protonated. The band at 266 nm corresponds to the absorbance region expected for a conjugated triene system,[29-31] confirming the presence of resonance structures (a) and (c) in *Figure 5.7* in solution.

5.3.3 ^1H Nuclear magnetic resonance spectroscopic studies

The ^1H NMR spectrum of unprotonated 4-VP is composed of five sets of peaks, indicating five types of protons. Peak assignment has already been pursued in the literature[21, 32-34] and is depicted graphically in *Figure 5.4*. NMR titration studies were performed at the same conditions as the aforementioned IR experiments utilizing the same monomer and acid concentrations.

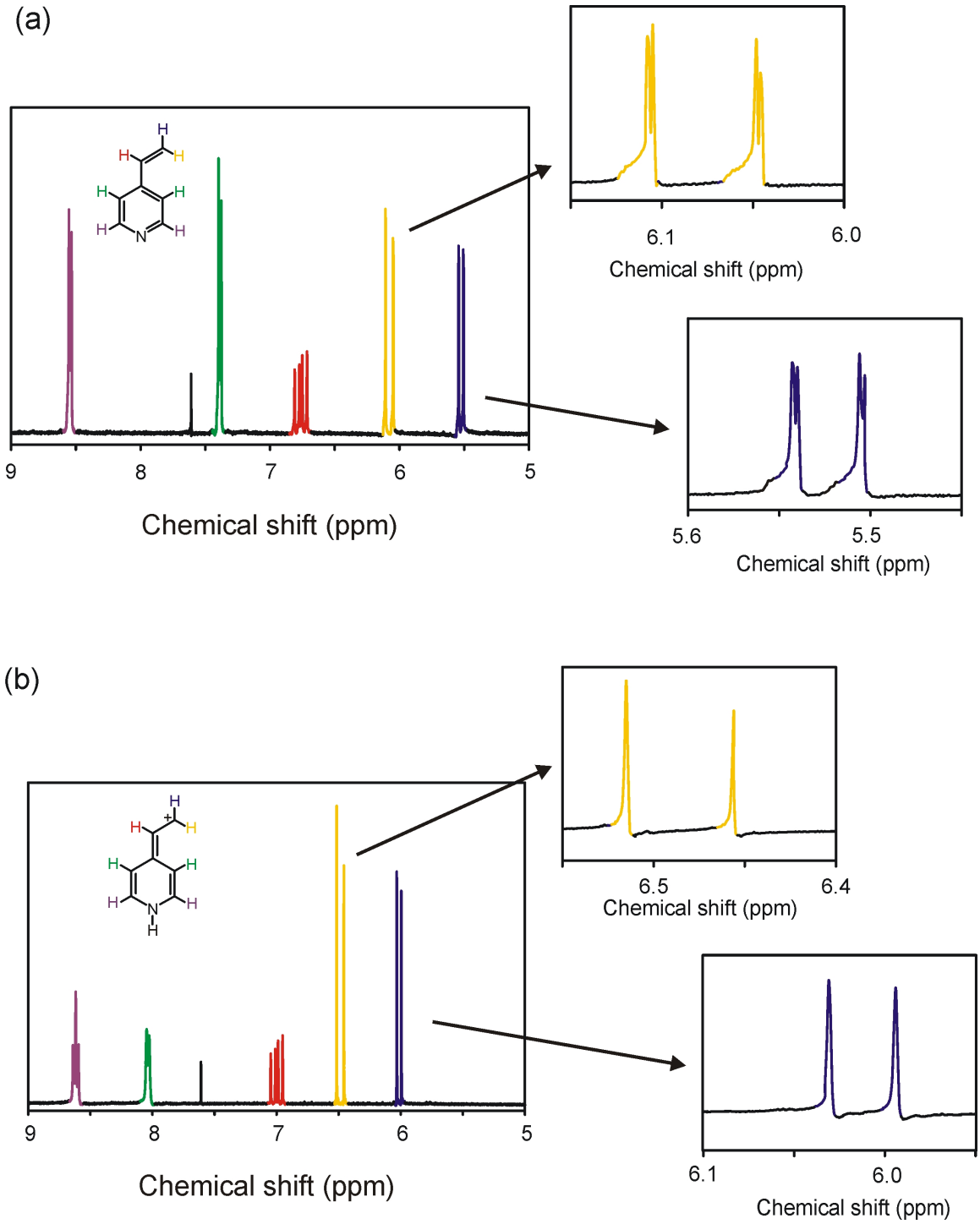

Figure 5.4: ^{1}H NMR spectra of (a) unprotonated and (b) fully protonated 4-VP. Expanded regions correspond to the terminal methylene protons, demonstrating the observed change in ^{2}J upon protonation.

Upon protonation/quaternization of the nitrogen atom in pyridine molecules induces an overall displacement of the ring protons to the low field, affecting the protons at the *para*- position most, and those at the *ortho*- position least.[33, 35, 36] 4-VP lacks protons at the *para*- position, however, protons at the *ortho*- and *meta*- positions exhibit a similar shift to the low field as demonstrated for pyridine. The trend observed is related to changes in π-electron density and paramagnetic contributions from the electrons at the nitrogen atom, induced by the protonation.[37] *Figure 5.5* summarizes the change in chemical shifts for each proton group upon incremental addition of perchloric acid.

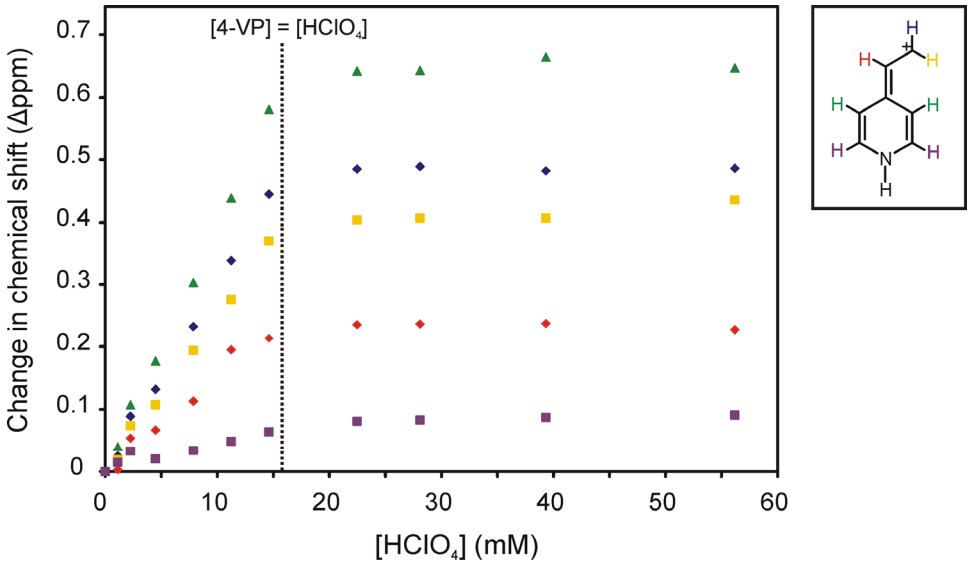

Figure 5.5: ^{1}H NMR chemical shifts upon addition of perchloric acid. The vertical dashed line indicates equimolarity of 4-VP and $HClO_4$.

Additional evidence that the structure of the monomer is influenced by the addition of acid is presented by changes in splitting pattern of protons in the *ortho*- position (at ~ 8.6 ppm). In unprotonated 4-VP, *ortho*- protons yield a doublet indicating that spin-spin splitting is caused by only one type of protons (the *meta*- protons). In contrast, a triplet is

obtained in the solutions containing excess acid, demonstrating that an additional proton is incorporated into the monomer neighboring the protons in the *ortho*- position. Finally, analysis of vicinal (^3J) and geminal (^2J) coupling constants at the vinylic protons results in predictable coupling constants for the unprotonated monomer (*Figure 5.6*).[21, 24] It has been observed, however, that ^2J is influenced by resonance effects, whereas ^3J remains unaffected by protonation of the nitrogen group. *Para*- substituted styrenes exhibit a behavior similar to that of protonated 4-VP, as reported by Reynolds and co-workers.[38-40]

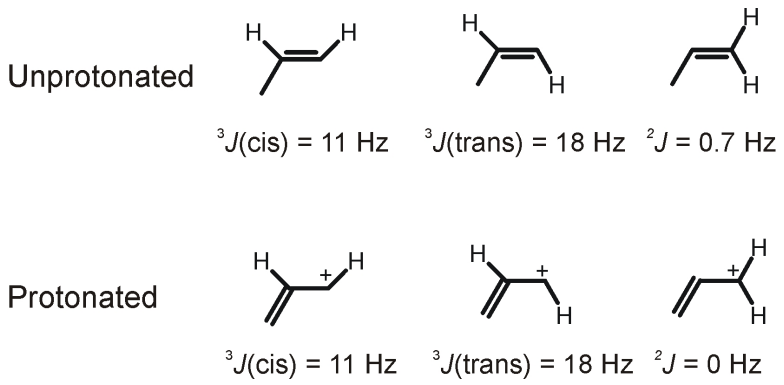

Figure 5.6: Coupling constants for the different vinyl protons in unprotonated and protonated 4-VP.

The authors concluded that substituents with different electronegativities change the geminal coupling constants in correlation with the extent of polarization of the styrene molecule. The vinyl group acts as a π-donor in order to stabilize the styrene, which induces a partial positive charge at the β-carbon. This effect decreases ^2J to values below 1 Hz. Protonation of the nitrogen atom in 4-VP results in the disappearance of ^2J (i.e. $^2J = 0$ Hz), indicating that a positive charge resides on the vinyl group and that the structure labeled (a) in *Figure 5.7* is preferentially adopted by the monomer in solution.

Therefore, upon electrochemical reduction, isomer (a) will generate the radical species responsible for initiating the polymerization reaction.

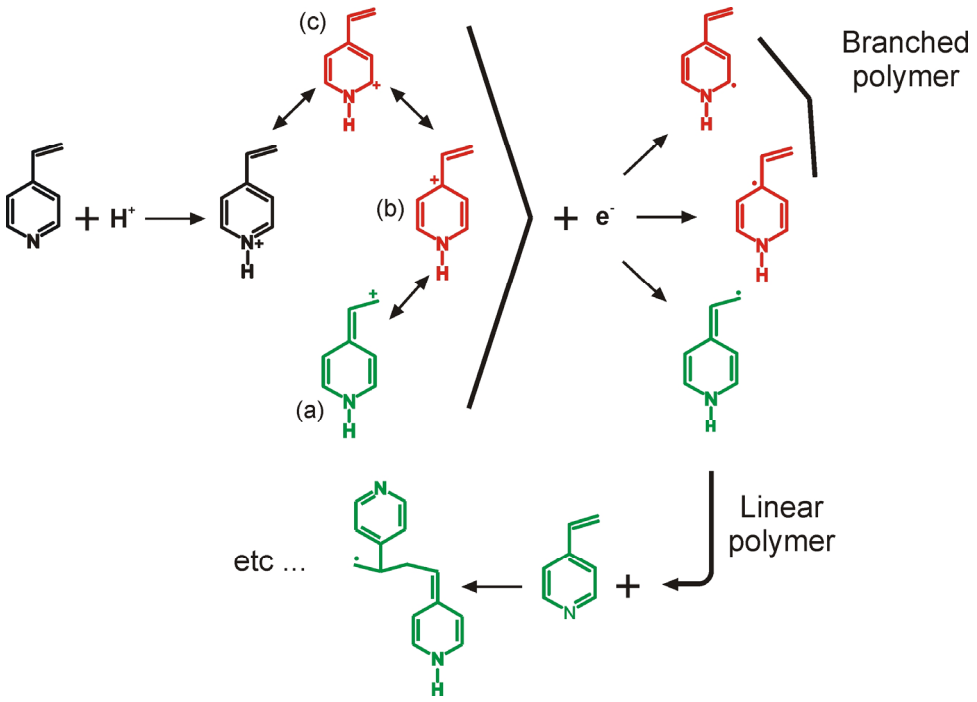

Figure 5.7: Possible resonance structures for [4-VP-H$^+$] (a-c), and proposed cathodic electropolymerization mechanism for a solution containing both [4-VP] and [4-VP-H$^+$] adapted from Ling et al.[4]

5.3.4 Electrochemical characterization

The cyclic voltammograms of the polymer films deposited at increasing amounts of perchloric acid displayed a variety of features. In solutions containing only the monomer and the supporting electrolyte a single reduction peak is observed at approx. -2.6 V (vs. Fc/Fc$^+$), which can be attributed to the reduction of the unprotonated monomer at the electrode.[12] Upon addition of perchloric acid, a second reduction peak evolves at approx. -1.0 V (vs. Fc/Fc$^+$) corresponding to the reduction of the protonated monomer.

Representative CVs containing ferrocene (as the internal standard[41]) are shown in *Figure 5.8*.

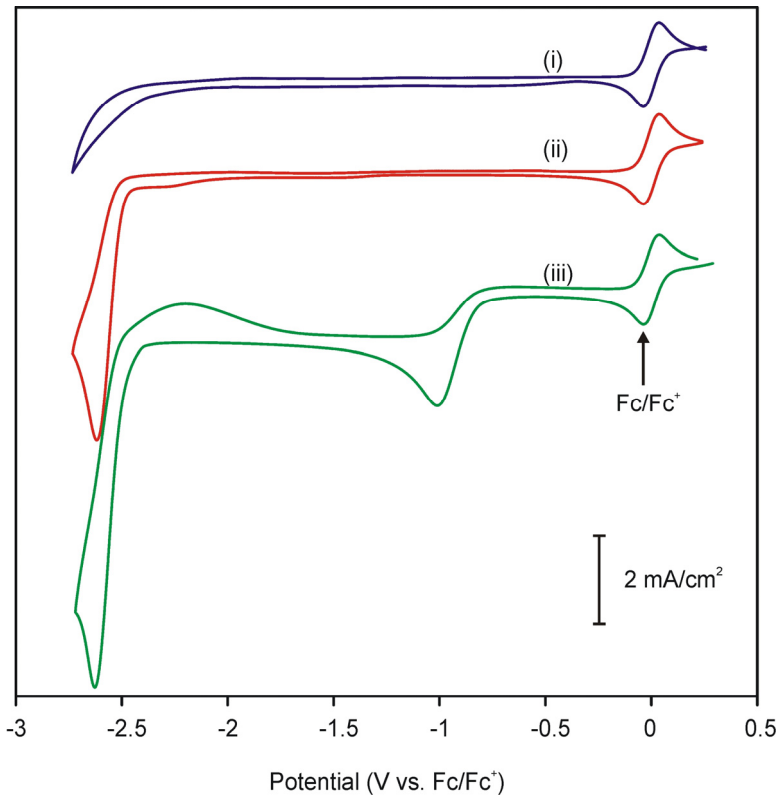

Figure 5.8: Cyclic voltammograms recorded in acetonitrile solutions containing (i) 0.1 M TEAP, (ii) 15.8 mM 4-VP and 0.1 M TEAP, and (iii) 15.8 mM 4-VP, 7.9 mM $HClO_4$ and 0.1 M TEAP.

The uniformity of an electrode coating (e.g. self-assembled monolayers[42], sputtered silicon nitride[43]) can be evaluated by monitoring the diffusion of a redox mediator through an insulating layer. The presence of a blocking layer delays the diffusion of a redox mediator towards the electrode surface, resulting in currents smaller than those recorded at bare electrodes. With cyclic voltammetry, this is observed as the absence of the current waves associated with the oxidation/reduction of the redox mediator. Hence, the uniformity of the deposited polymer films was investigated by determining the permeability of 5 mM $Ru(NH_3)_6^{3+}$ at P(4-VP) modified electrodes. *Figure 5.9*

summarizes the current response obtained from the $Ru(NH_3)_6^{3+/2+}$ couple with poly(4-VP) coated electrodes deposited grown with different amounts of perchloric acid.

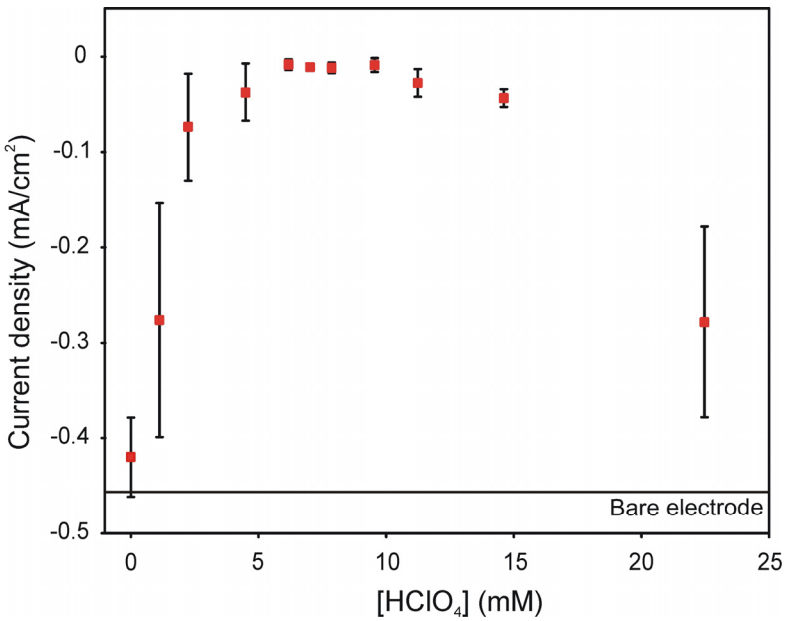

Figure 5.9: Current response obtained by cyclic voltammetry from a 5 mM $Ru(NH_3)_6^{3+}$ solution (0.1 M KCl) at an electrode coated with different 4-VP-to-$HClO_4$ ratios contrasted by the response from a bare platinum electrode (solid line) ($n \geq 3$).

Under the conditions examined in this study, uniform films can be reproducibly deposited with acid concentrations ranging from 4.5 mM to 11.2 mM. By comparison with results obtained via IR spectroscopy, the same acid concentration range corresponds to a protonated-to-unprotonated monomer ratio of 0.28 to 0.71, respectively. The trend seen in *Figure 5.9* demonstrate that in order to obtain uniformly coated electrodes, the cathodic electropolymerization of 4-VP requires that at least one-third of the 4-VP monomers be protonated. These results confirm the reaction mechanism proposed by Ling et al.[4] whereby the initiation of electropolymerization reaction occurs through the reduction of protonated 4-VP. Furthermore, the dependency on both forms of the

monomer (protonated and unprotonated) for polymer formation is emphasized by the increasing currents measured at higher acid concentrations.

Based upon the aforementioned experiments, the uptake of $Fe(CN)_6^{4-}$ in electropolymerized 4-VP films was evaluated. Polymer films deposited in the presence of 7.9 mM $HClO_4$, corresponding to approx. half of the monomers being protonated, were then exposed to a 5 mM $Fe(CN)_6^{4-}$ solution, and the anion uptake was verified by cyclic voltammetry at 10 min intervals for 60 min. Since only a fraction of the pyridine rings in the polymer are protonated, $Fe(CN)_6^{4-}$ solutions were additionally acidified with concentrated HCl to protonate neutral pyridine groups incorporated into the membrane.

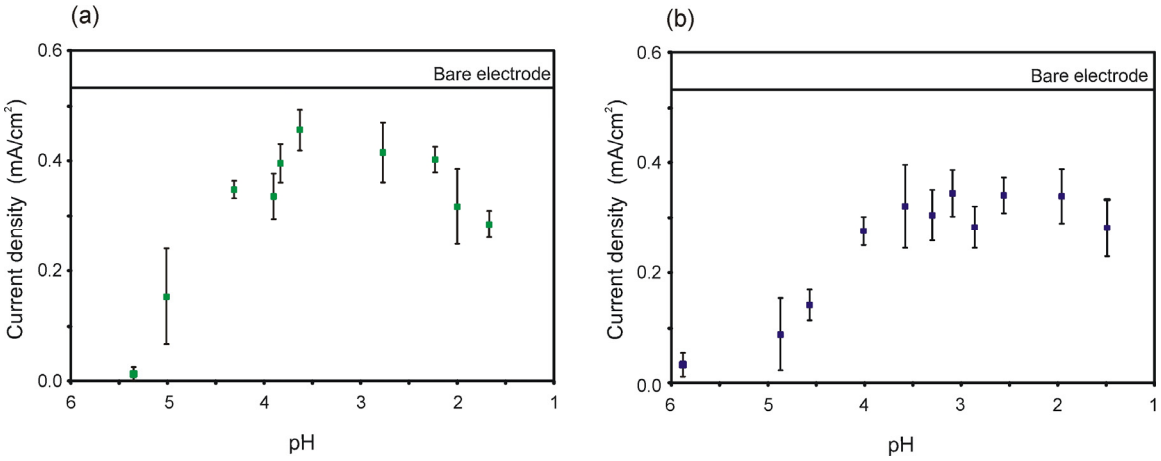

Figure 5.10: Current density measured by cyclic voltammetry at a P(4-VP) modified electrode immersed in a 5 mM $Fe(CN)_6^{4-}$ solution at various pH values (n = 3) with (a) 0.1 M KCl and (b) 0.5 M KCl. For comparison, the current response for the bare electrode is depicted as a solid line.

The response of the polymer membrane to $Fe(CN)_6^{4-}$ at different pH values and in solutions with different amounts of supporting electrolyte (i.e. different ionic strength) is presented in *Figure 5.10*. Concomitantly with a higher density of positive charges in the polymer, the measured current corresponding to the diffusion $Fe(CN)_6^{4-}$ through the

polymer rapidly increases, reaching a maximum at a pH of approximately 3.5. However, the current measured at the modified electrode remains smaller than that at a bare electrode. The uptake of ionic species into a redox polymer is dependent upon the availability of active redox sites. For a redox polymer such as poly(4-VP) sufficient positively charged redox active sites must be available within the polymer to incorporate $Fe(CN)_6^{4-}$ anions. A very thin polymer film evidently contains a limited amount of redox sites and therefore $Fe(CN)_6^{4-}$ cannot be enriched, with respect to the surrounding solution. Hence, the poly(4-VP) membranes deposited with the approach described behave as semipermeable membranes, restricting access of $Ru(NH_3)_6^{3+}$ to the electrode, while permitting diffusion of anions.

High chloride ion concentrations (0.5 M) have been reported to induce a shift in the chemical equilibrium of $Fe(CN)_6^{3-}$ in poly(2-VP), resulting in the substitution of the redox site ($Fe(CN)_6^{3-}$) with the chloride ions.[44] Additionally, swelling of the membrane promoted by the chloride ions results in a increased effusion of $Fe(CN)_6^{3-}$ from the polymer (i.e. decreased enrichment).[44] In contrast, the poly(4-VP) do not exhibit a significantly different response at higher chloride ion concentration.

Furthermore, $Fe(CN)_6^{4-}$ is a weak tetravalent Brønsted base, therefore an equilibrium of different species will be established in solution at a given pH value. The fractions of each species calculated according to the acid dissociation constants provided by Jordan et al.[45] are displayed graphically in *Figure 5.11*. Although the distribution of species in solution at different electrolyte concentrations varies (especially between pH values of 2 and 3), the current measured at the modified electrodes is independent of the exact hexacyanoferrate species. The response obtained at low pH values also serves to

demonstrate that poly(4-VP) films do not degrade under acidic conditions, since deteriorated film will display a response to $Fe(CN)_4^{6-}$ approaching that of the bare electrode, corresponding to the loss of coverage by the film.

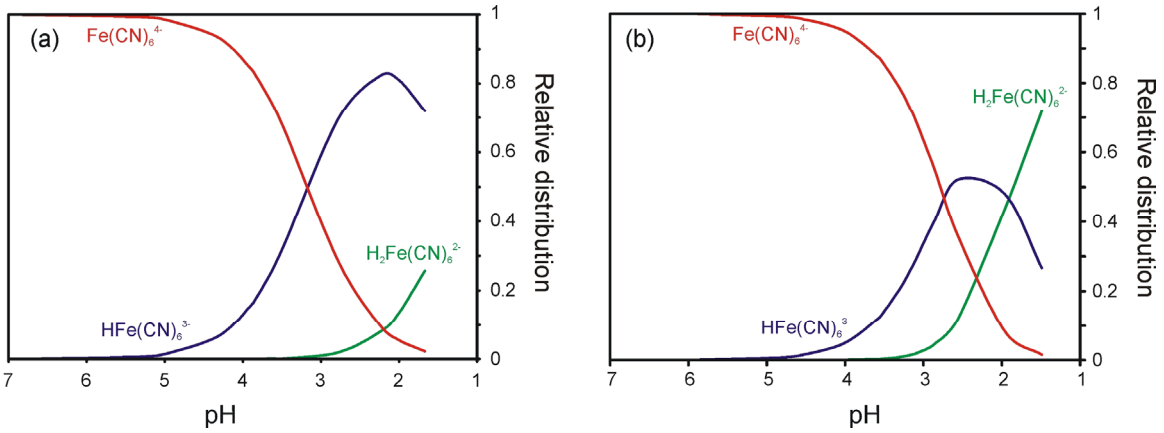

Figure 5.11: Distribution of hexacyanoferrate species in solution at different pH values with (a) 0.1 M KCl and (b) 0.5 M KCl.

In order to confirm that the increased measured currents does not arise from degradation of the layer at low pH values, polymer modified electrodes were immersed in solutions containing 5mM $Ru(NH_3)_6^{3+}$ (with 0.1 M KCl) acidified with concentrated HCl to a pH of 3.4 (*Figure 5.12*). The current response measured at the acidified solution is nearly identical to that obtained $Ru(NH_3)_6^{3+}$ solutions with no added acid. However, at low pH values, the protonation of the pyridine groups should further hinder the diffusion of cationic species to the electrode surface, yielding lower currents. Since the current measured is not affected at the lower pH (in contrast to that measured for $Fe(CN)_6^{4-}$), diffusion of $Ru(NH_3)_6^{3+}$ to the electrode must occur at defects (e.g. pinholes) present in the polymer.

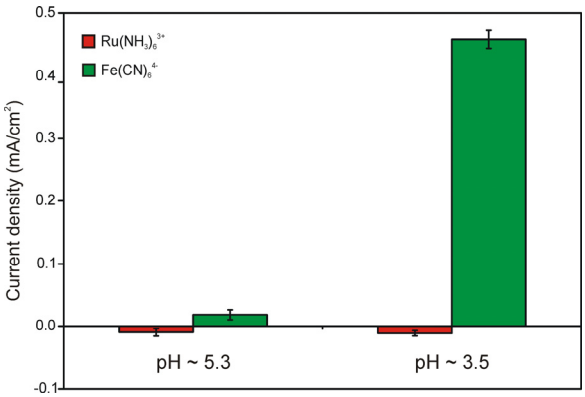

Figure 5.12: Current response obtained via cyclic voltammetry of P(4-VP) modified electrodes exposed to solutions containing 5mM $Ru(NH_3)_6^{3+}$ or 5mM $Fe(CN)_6^{4-}$ (with 0.1 M KCl). All solutions, with the exception of $Ru(NH_3)_6^{3+}$ at pH = 5.3, were acidified with HCl to the desired pH (n = 3).

Finally, in order to confirm $Fe(CN)_6^{4-}$ uptake into the membrane, the poly(4-VP) coated electrodes loaded with $Fe(CN)_6^{4-}$ were exposed to a solution containing only the electrolyte acidified to a pH of 3.8. *Figure 5.13* overlays a cyclic voltammogram obtained at the polymer modified electrode in a solution containing $Fe(CN)_6^{4-}$ with a CV obtained at the electrolyte-only solution. The peak current immediately decreases to approx. 1 % of the original value, thereby providing confirmation that the poly(4-VP) films do not function as enrichment membranes, rather as semipermeable thin films restricting the diffusion of cationic species.

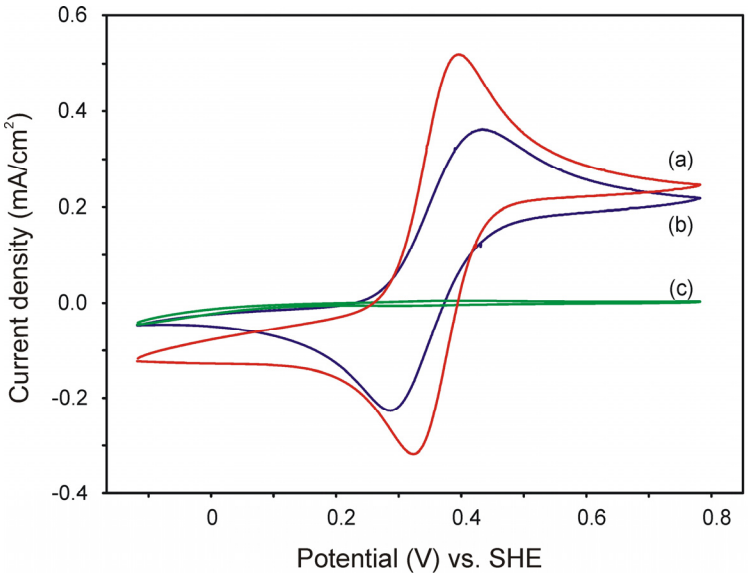

Figure 5.13: Cyclic voltammograms of a 5 mM $Fe(CN)_6^{4-}$ solution (0.1 M KCl, pH = 3.83) using (a) a bare Pt disc electrode and (b) a poly(4-VP) coated Pt disc electrode. The same electrode (c) was then switched to an electrolyte-only solution (pH = 3.73).

The peak current measured at the electrolyte-only solution decreases by only 10 % over a period of 60 min indicating minimal leaching of the incorporated anionic species.

Thicker polymer films may be grown by either (1) increasing the number of electropolymerization cycles, or (2) increasing the monomer concentration. The response of the modified electrode to $Fe(CN)_6^{4-}$ is not significantly affected by extending number of growth cycles from 15 to 150, which in agreement with a self-limiting growth process (*Figure 5.14*).[8]

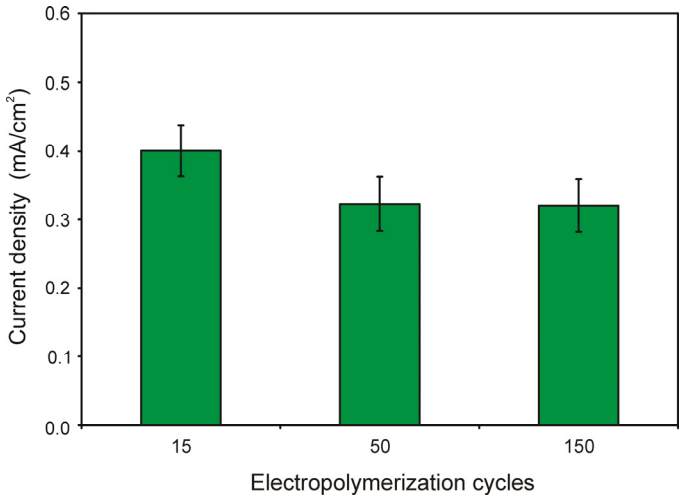

Figure 5.14: Changes in the current response obtained by cyclic voltammetry of polymer modified electrodes to 5 mM $Fe(CN)_6^{4-}$ with increasing electropolymerization cycles (pH = 3.5, 0.5 M KCl, n = 3).

Alternatively, the concentration of the monomer can be increased and, concomitantly, the probability that a radical monomer will initiate chain propagation close to the electrode surface is also increased.[46] At the comparatively low 4-VP concentration used in this study, the electrochemically formed radical species diffuse into the bulk forming oligomers in solution rather than at the electrode surface. Doubling the 4-VP and $HClO_4$ concentrations induces the formation of several white particulates within minutes of mixing. 4-VP spontaneously polymerizes in presence of alkyl halides and certain mineral acids, including $HClO_4$.[32, 47-49] Therefore, the monomer concentration must be kept low to hinder the spontaneous polymerization process.

Therefore, the P(4-VP) films obtained by the procedure described herein do not possess the thickness necessary to exhibit an enrichment behavior towards $Fe(CN)_6^{4-}$. The determining factor for the low thickness is the monomer concentration required in order to prevent spontaneous polymerization. Nevertheless, the polymer films described show semipermeable properties by blocking the diffusion of $Ru(NH_3)_6^{3+}$ to the electrode.

Additionally, the response obtained for $Fe(CN)_6^{4-}$ was shown to be independent of the chloride concentration or the distribution of hexacyanoferrate species in solution, demonstrating that the response at poly(4-VP) films does not degrade even at low pH values.

5.4 Final remarks

Extensive spectroscopic studies were devised for correlating the formation of high quality electropolymerized poly(4-vinylpyridine) films with a range of acid concentrations essential to sustaining the polymerization process. Furthermore, these studies provide additional information about the electropolymerization mechanism by establishing the predominant structural isomer present in solution. responsible for the initiation of the electropolymerization process. Correlation of data obtained via IR spectroscopy and electrochemistry, it was determined that approx. 30 to 70 % of the 4-VP monomers in solution need to be protonated in order to generate uniform polymer films that cover the entire electrode surface. Additional electrochemical studies have demonstrated that films grown at these conditions behave as semipermeable thin-film membranes selectively blocking cationic species, such as $Ru(NH_3)_6^{3+}$. Due to limitations of the maximum monomer concentration that can be employed, continuing efforts should be directed towards development of alternative electroanalytical procedures specifically for production of thicker poly(4-VP) films.[46]

5.5 References

1. Stegemiller Michael, L.; Heineman William, R.; Seliskar Carl, J.; Ridgway Thomas, H.; Bryan Samuel, A.; Hubler, T.; Sell Richard, L., *Spectroelectrochemical sensing based on multimode selectivity simultaneously achievable in a single device. 11. Design and evaluation of a small portable sensor for the determination of ferrocyanide in Hanford waste samples*, Environmental science & technology, **37 (1)**, 123-130, (2003).

2. Heineman, W. R.; Seliskar, C. J.; Richardson, J. N., *Spectroelectrochemical sensing based on multimode selectivity simultaneously achievable in a single device: An overview*, Aust. J. Chem., **56 (2-3)**, 93-102, (2003).

3. Bartak, D. E.; Kazee, B.; Shimazu, K.; Kuwana, T., *Electrodeposition and characterization of platinum microparticles in poly(4-vinylpyridine) film electrodes*, Anal. Chem., **58 (13)**, 2756-2761, (1986).

4. Ling, X.; Pritzker, M. D.; Burns, C. M.; Byerley, J. J., *A Mechanism for Electropolymerization of 2-Vinylpyridine Coatings on Metal Surfaces*, Macromolecules, **31 (26)**, 9134-9140, (1998).

5. Oyama, N.; Anson, F. C., *Electrostatic binding of metal complexes to electrode surfaces coated with highly charged polymeric films*, J. Electrochem. Soc., **127 (1)**, 249-250, (1980).

6. Li, T.; Wang, E. K., *Electrocatalytic oxidation and flow amperometric detection of hydrazine at an electropolymerized 4-vinylpyridine/palladium film electrode*, Electroanalysis, **9 (15)**, 1205-1208, (1997).

7. Kolthoff, I. M.; Chantooni, M. K., Jr., *Calibration of the glass electrode in acetonitrile. Shape of potentiometric titration curves. Dissociation constant of picric acid*, J. Am. Chem. Soc., **87 (20)**, 4428-4436, (1965).

8. Ling, X.; Pritzker, M. D.; Burns, C. M.; Byerley, J. J., *Effects of reaction conditions on the formation of poly(2-vinylpyridine) coatings by electropolymerization*, J. Coat. Tech., **72 (908)**, 71-80, (2000).

9. Oh, S. M.; Faulkner, L. R., *Electron transport dynamics in partially quaternized poly(4-vinylpyridine) thin films containing ferri/ferrocyanide*, J. Electroanal. Chem. Interfac., **269 (1)**, 77-97, (1989).

10. Finklea, H. O.; Vithanage, R. S., *Non-electroactive electrode coatings formed by electrochemical polymerization*, J. Electroanal. Chem. Interfac., **161 (2)**, 283-294, (1984).

11. Lebrun, C.; Deniau, G.; Viel, P.; Tanguy, J.; Lecayon, G. In *Study of the ability of 4-vinylpyridine to form electropolymerized coatings on nickel cathodes*, AIP Conf. Proc., 1996; pp 67-74.

12. Lebrun, C.; Deniau, G.; Viel, P.; Lecayon, G., *Electrosynthesis of poly(4-vinylpyridine) films on metallic surfaces under anodic and cathodic polarizations: structure and properties of the organic coatings*, Surf. Coat. Technol., **100-101 (1-3)**, 474-479, (1998).

13. Viel, P.; Palacin, S.; Descours, F.; Bureau, C.; Le Derf, F.; Lyskawa, J.; Salle, M., *Electropolymerized poly-4-vinylpyridine for removal of copper from wastewater*, Appl. Surf. Sci., **212-213**, 792-796, (2003).

14. Sekine, I.; Kohara, K.; Sugiyama, T.; Yuasa, M., *Syntheses of polymerized films on mild steels by electrooxidation and electroreduction and their corrosion resistance*, J. Electrochem. Soc., **139 (11)**, 3090-3097, (1992).

15. De Bruyne, A.; Delplancke, J. L.; Winand, R., *Electropolymerization of poly(2-vinylpyridine) films on zinc*, J. Appl. Electrochem., **25 (3)**, 284-290, (1995).

16. Ling, X.; Byerley, J. J.; Pritzker, M. D.; Burns, C. M., *Critical effect of pH on the formation of organic coatings on mild steel by the aqueous electropolymerization of 2-vinylpyridine*, J. Appl. Electrochem., **27 (12)**, 1343-1348, (1997).

17. Ling, X. Formation of polymer coatings by electropolymerization. University of Waterloo, Waterloo, 1998.

18. Skoog, D. A.; Holler, J. F.; Nieman, T. A., *Principles of Instrumental Analysis*. 5th ed.; Saunders College Publishing: 1998; p 879 pp.

19. Pietra, S.; Lodi, L., *The infrared and ultraviolet spectra of some vinylpyridines*, Proc. Intern. Meeting Mol. Spectry., 4th, Bologna, 1959, **2**, 921-923, (1962).

20. Vorontsov, E. D.; Panov, V. P., *Vibrational spectra of protonated poly(4-vinylpyridine)*, Vysokomol. Soedin., Ser. A, **18 (11)**, 2412-2417, (1976).

21. Mielke, I.; Ringsdorf, H., *Vinylpyridinium compounds. I. Infrared and NMR spectroscopic investigation*, J. Polym. Sci., Polym. Symp., **No. 31**, 107-120, (1970).

22. Bayari, S.; Yurdakul, S., *Fourier transform infrared and Raman spectra of 4-vinylpyridine and its transition metal(II) tetracyanonickelate complexes*, Spectrosc. Lett., **33 (4)**, 475-483, (2000).

23. Green, J. H. S.; Harrison, D. J., *Vibrational assignments for styrene-d0 and -d8; 2-vinyl- and 4-vinyl pyridine*, Spectrochim. Acta, Part A, **33A (2)**, 249-250, (1977).

24. Pavia, D.; Lampman, G.; Kriz, G., *Introduction to Spectroscopy*. 2nd ed.; Saunders College Publishing: 1996; p 512.

25. Armarego, W. L. F., *Ultraviolet spectra of heterocycles*, Phys. Methods Heterocycl. Chem., **3**, 67-222, (1971).

26. Frank, R. L.; Meikle, R. W., *Pyridines. VII. Conversion of 2-cyclohexenones to pyridines*, J. Am. Chem. Soc., **72**, 4184-4185, (1950).

27. Tazuke, S.; Okamura, S., *The p-p* transition spectra and polymerizability of vinyl compounds complexed with zinc salts*, J. Polym. Sci., Polym. Lett. Ed., **5 (1)**, 95-99, (1967).

28. Favini, G., *Electronic structure of pyridine derivatives. I. Ultraviolet spectra, dipole moments, and basicity of vinyl and styryl pyridine*, Gazz. Chim. Ital., **93 (6)**, 635-648, (1963).

29. Datta, P.; Goldfarb, T. D.; Boikess, R. S., *Photolysis of matrix isolated 1,3-cyclohexadiene, cis-1,3,5-hexatriene, and trans-1,3,5-hexatriene*, J. Am. Chem. Soc., **93 (20)**, 5189-5193, (1971).

30. Furukawa, Y.; Takeuchi, H.; Harada, I.; Tasumi, M., *Matrix-isolation infrared and ultraviolet spectroscopic studies of less stable conformers of 1,3,5-hexatriene*, J. Mol. Struct., **100**, 341-350, (1983).

31. Yeranos, W. A.; Spangler, C. W., *Hueckel molecular orbital study of the electronic spectra of some substituted hexatrienes*, J. Mol. Spectrosc., **24 (2)**, 244-247, (1967).

32. Mielke, I.; Ringsdorf, H., *Untersuchung von Vinylpyridiniumverbindungen. III. Über den Mechanismus der "spontanen Polymerisation" von 4-vinylpyridiniumsalzen in Wasser*, Makromol. Chem., **142**, 319-324, (1971).

33. Smith, I. C.; Schneider, W. G., *The proton magnetic resonance spectrum and the charge distribution of the pyridinium ion*, Can. J. Chem., **39**, 1158-1161, (1961).

34. Jazwinski, J.; Duddeck, H., *Pyridine and aminide derivatives as ligands in 1:1 Rh2[tfa]4 adducts: 1H, 13C and 15N NMR study*, Magn. Reson. Chem., **41 (11)**, 921-926, (2003).

35. Katritzky, A. R.; Dega-Szafran, Z., *Proton and carbon-13 NMR studies of 1-substituted pyridinium salts*, Magn. Reson. Chem., **27 (11)**, 1090-1093, (1989).

36. Katritzky, A. R.; Rees, C. W., *Comprehensive Heterocyclic Chemistry*. 1st ed.; Pergamin Press, Inc.: Elmsford, NY, 1984; Vol. 2, p 690.

37. Gil, V. M. S.; Murrell, J. N., *Interpretation of the proton and nitrogen chemical shifts of pyridine and pyridinium cation*, Transactions of the Faraday Society, **60 (494)**, 248-255, (1964).

38. Hamer, G. K.; Peat, I. R.; Reynolds, W. F., *Investigations of substituent effects by nuclear magnetic resonance spectroscopy and all-valence electron molecular orbital calculations. I. 4-Substituted styrenes*, Can. J. Chem., **51 (6)**, 897-914, (1973).

39. Reynolds, W. F.; Modro, T. A.; Mezey, P. G.; Skorupowa, E.; Maron, A., *Experimental and theoretical investigation of the unusual substituent effect of the vinyl group*, Can. J. Chem., **58 (4)**, 412-417, (1980).

40. Reynolds, W. F.; Peat, I. R.; Hamer, G. K., *Substituent effects on coupling constants to vinyl protons in styrene derivatives*, Can. J. Chem., **52 (19)**, 3415-3423, (1974).

41. Gagne, R. R.; Koval, C. A.; Lisensky, G. C., *Ferrocene as an internal standard for electrochemical measurements*, Inorg. Chem., **19 (9)**, 2854-2855, (1980).

42. Ganesh, V.; Pal, S. K.; Kumar, S.; Lakshminarayanan, V., *Self-assembled monolayers (SAMs) of alkoxycyanobiphenyl thiols on gold - A study of electron transfer reaction using cyclic voltammetry and electrochemical impedance spectroscopy*, J. Colloid Interface Sci., **296 (1)**, 195-203, (2006).

43. Kranz, C.; Friedbacher, G.; Mizaikoff, B.; Lugstein, A.; Smoliner, J.; Bertagnolli, E., *Integrating an Ultramicroelectrode in an AFM Cantilever: Combined Technology for Enhanced Information*, Anal. Chem., **73 (11)**, 2491-2500, (2001).

44. Tantavichet, N.; Pritzker, M. D.; Burns, C. M., *Electropolymerized poly(2-vinylpyridine) coatings as ion-exchange polymer modified electrodes*, J. Appl. Electrochem., **31 (3)**, 281-291, (2001).

45. Jordan, J.; Ewing, G. J., *Protonation of hexacyanoferrates*, Inorg. Chem., **1**, 587-591, (1962).

46. Schuhmann, W.; Kranz, C.; Wohlschlager, H.; Strohmeier, J., *Pulse technique for the electrochemical deposition of polymer films on electrode surfaces*, Biosens. Bioelectron., **12 (12)**, 1157-1167, (1997).

47. Kabanov, V. A.; Aliev, K. V.; Kargina, O. V.; Patrikeeva, T. I.; Kargin, V. A., *Specific polymerization of vinylpyridinium salts. Polymerization on macromolecular matrixes*, J. Polym. Sci., Polym. Symp., **16 (Pt. 2)**, 1079-1094, (1967).

48. Salamone, J. C.; Ellis, E. J.; Bardoliwalla, D. F.; Wilson, C. R., *Formation of high molecular weight polyvinylpyridinium salts by spontaneous polymerization*, Polym. Prepr. (Am. Chem. Soc., Div. Polym. Chem.), **14 (2)**, 773-777, (1973).

49. Salamone, J. C.; Ellis, E. J.; Israel, S. C., *Preparation and polymerization of 2- and 4-vinylpyridine salts*, Nuova Chimica, **49 (1)**, 74-76, (1973).

6 CONCLUSION AND OUTLOOK

The main goal of this thesis was the development of mid-IR transparent electrodes for spectroelectrochemical analysis using multi-reflection ATR waveguides. The first application of conducting DLC thin films in mid-IR-ATR spectroelectrochemistry was successfully demonstrated. In addition, deposition conditions for an electropolymerized ion-exchange membrane at IR-ATR spectroelectrochemical sensing platforms utilizing the developed DLC thin films were established in this thesis.

6.1 Nitrogen-doped DLC

The characterization of N-DLC layers in this work included the determination of their physical composition, the electrochemical activity, and the IR transparency. Electrochemical activity of the N-DLC layers did not display a correlation to the nitrogen content, or to the size of sp^2-hybridized carbon clusters. However, it was demonstrated that by utilizing cathodic pre-treatment, the heterogeneous electron transfer rate of $Fe(CN)_6^{4-/3-}$ at N-DLC could be significantly improved due to the re-activation of the carbon surface after exposure to the atmosphere. The N-DLC layers examined herein displayed an electrochemical activity comparable to that of moderately doped BDD, while providing sufficient mid-IR transparency.

Furthermore, N-DLC layers deposited onto ZnSe exhibited excellent adhesive properties upon application of an electric field, and the first application of doped-DLC in multi-

reflection IR-ATR spectroelectrochemistry was demonstrated for the electropolymerization of polyaniline.

The work presented herein showed that de-activation of the surface can result in decreased electron transfer rates. Continuing efforts should be directed towards the development of new methods aimed at extending the lifetime of the surface. Hydrogenated glassy carbon and BDD electrodes display an increased resistance to fouling due to C-H terminated surfaces. Similar surface properties should be obtainable if N-DLC layers are treated with a hydrogen plasma immediately following the deposition process.

Additionally, in order to obtain an improved electrochemical behavior at the ATR waveguides, the sheet resistance of N-DLC will need to be further diminished. As was discussed in *Section 3.3.4*, the introduction of nitrogen did not influence the electrical conductivity of the layers. Hence, investigations directed towards determination of doping efficiency of other dopants, such as phosphorous and boron, at the deposition parameters utilized in this study (*Section 3.2.1*) should be performed.

6.2 Metal-DLC nanocomposite

Increased electrical conductivity of metal-DLC compared to metal-free layers was demonstrated via the inclusion of metal nanoclusters. Electrochemical activity of the investigated nanocomposite layers display a direct correlation to the metal content. Furthermore, these electrodes provide wider working potential windows compared to those of the respective pristine metals. Transparency in the mid-IR was confirmed for both gold- and platinum-DLC coated waveguides. However, delamination of the layers from ZnSe waveguides occurred upon application of a potential step of +0.6 V (vs.

AgQRE). Improved adhesion characteristics of metal-DLC layers are obtained by deposition at waveguide materials capable of forming carbide bonds, such as germanium. The presence of interfacial carbide phases between the DLC and germanium was confirmed by XPS depth profiling.

Additional efforts should focus on the investigation of contributions to the heterogeneous electron transfer from each constituent (i.e. metal vs. sp^2-hybridized carbon). Surface functionalization of C=O bonds with dinitrophenylhydrazine hinders the heterogeneous electron transfer at sp^2-sites for $Fe(CN)_6^{4-/3-}$. By preventing contributions from the sp^2-hybridized carbon, the electron transfer at the metal can be isolated.

Furthermore, the presence of pinholes in the metal-DLC layers can lead to degradation of the germanium waveguide under anodic conditions. Hence, further optimization of the deposition conditions aimed at obtaining homogeneous coverage of the waveguide should be performed.

6.3 Electropolymerization of poly(4-VP)

Spectroscopic studies of pre-polymerization solutions demonstrated that the positive charge in the protonated form of the 4-VP monomer resides on the β-carbon of the vinyl group. The working electrodes were shown to be uniformly coated with poly(4-VP) provided that 30 – 70 % of the monomer was present in the protonated form during the electropolymerization process. Finally, membranes deposited at the experimental conditions developed and optimized in this thesis were shown to function as semi-permeable membranes permitting the diffusion of $Fe(CN)_6^{4-}$, while restricting $Ru(NH3)_6^{3+}$.

Although the membranes presented herein display preferential diffusion towards anions, enrichment of $Fe(CN)_6^{4-}$ was not possible due to the small thickness. The spontaneous polymerization of 4-VP forbids the utilization of higher monomer concentrations, thereby generating a sufficiently high concentration of radicals to sustain chain propagation. Therefore, continuing work in this field should concentrate on the characterization of alternate electroanalytical techniques in an effort to produce higher amounts of radical monomers. Upon deposition of thicker membranes the application to IR-ATR spectroelectrochemical sensing will be possible.